Modification of b quark hadronization in high-multiplicity pp collisions at $\sqrt{s} = 13\,\text{TeV}$

J. Matthew Durham, Cameron Dean, Eliane Epple, Krista Smith, Cesar da Silva, Cheuk-Ping Wong

Los Alamos National Laboratory, Los Alamos, NM USA

Abstract

The production rates of B_s^0 mesons relative to B^0 mesons are measured in pp collisions at $\sqrt{s} = 13\,\text{TeV}$ as a function of the number of charged particle tracks. The ratio is found to increase with event multiplicity at relatively low transverse momentum. These measurements may have implications for the b quark hadronization mechanism in hadron collisions.

1 Introduction

Strangeness enhancement was one of the first proposed signatures of quark-gluon plasma formation in heavy ion collisions [1]. Since the QCD critical temperature T_c is approximately equal to twice the strange quark mass, $s\bar{s}$ quark pairs can be produced thermally in the deconfined quark-gluon plasma. As the plasma expands and cools, these thermalized strange quarks can combine with other quarks at chemical freezeout to form color singlet hadrons through coalescence, rather than fragmentation in vacuum. The emergence of these additional production and hadronization mechanisms can alter the observed hadron chemistry and lead to an enhanced number of hadrons that contain strange quarks.

Recently, high-multiplicity pp collisions have shown behavior that is typically associated with the formation of quark-gluon plasma, which was previously thought only to manifest in collisions of large nuclei. Foremost among these newly observed effects is strangeness enhancement, where the yields of strange baryons and mesons are enhanced in collisions where a large number of charged particles are produced [2].

Measurements of the relative fractions of B hadrons produced in pp collisions can provide new information on these possible effects. The mass of a pair of b quarks is much greater than the deconfinement temperature, so thermal production is not possible, and contrary to light quarks they are not produced in the fragmentation process at any significant rate. Therefore, b production is essentially fixed by the hard scattering in the initial stages of a collision and is well described by perturbative QCD. If hadronization via coalescence emerges as a mechanism for forming final state B hadrons in dense hadronic systems, then the production rates of B hadrons with a strange quark could increase relative to production of B hadrons containing one light quark.

In this Note we describe measurements of the ratios of B_s^0/B^0 mesons produced as a function of charged particle multiplicity, which is represented by the number of charged tracks reconstructed in the VELO detector. The analysis proceeds as follows: using the 13 TeV pp collision data from 2016, 2017, and 2018, the ratios of B_s^0/B^0 counts are found by fitting the $J/\psi\pi^+\pi^-$ invariant mass spectra in bins of multiplicity. The measured ratios of counts are corrected for the relative LHCb acceptance, trigger, reconstruction, and particle ID efficiencies, in order to give the physics results of the ratio of cross sections. Systematic uncertainties on each correction are discussed in the relevant sections.

2 Data sets

The data considered here are 2016, 2017, and 2018 pp collisions at $\sqrt{s} = 13$ TeV, using stripping versions 28r2, 29r2, and 34, respectively. This sample corresponds to a total integrated luminosity of 5.57/fb. The decays of interest are $B_s^0, B^0 \to J/\psi\pi^+\pi^-$. Invariant mass spectra are constructed from stripped data with preselected dimuons near the J/ψ mass by combining J/ψ candidates with charged pions from the same event. DaVinci v50r6 is used to select $J/\psi\pi^+\pi^-$ candidates. Once a candidate is identified, the `DecayTreeFitter` TupleTool is used to refit the decay product tracks with the constraints of a common vertex, and kinematic constraints that set the dimuon mass to the J/ψ mass reported in the PDG.

2.1 Stripping and Cuts

The data is preselected using the `FullDSTDiMuonJpsi2MuMuDetached` stripping line, which is designed to select J/ψ mesons that originate from a displaced vertex. This line requires at least one reconstructed primary vertex, and two tracks which each have transverse momentum $p_T > 500$ MeV/c, an absolute decay length significance $|$BPVDL$|>3$, and satisfy the minimal muon ID criteria `MINTREE('mu+'==ABSID,PIDmu) > 0.0`. The two tracks are required to form a pair with an invariant mass between 2996.916 and 3196.916 MeV/c^2 and have a vertex fit χ^2 `VCHI2PDOF< 20.0`.

Candidates considered in this analysis are required to satisfy the L0Muon TOS, HLT1DiMuonHighMassDecision TOS, and HLT2DiMuonDetachedJPsiDecision TOS trigger criteria.

Further selections are applied to the stripped data to enhance the signal/background for our decays of interest. Dimuon pairs are required to have a mass within $\pm 3\sigma$ of the mean of the J/ψ peak, which is found to be 12 MeV/c^2 by fitting the mass spectrum of dimuons from candidates which pass all cuts. See Fig. 1. The cuts are summarized in Tab. 1. The mass spectra that are prepared using these cuts are shown in Fig. 2. The combinatorial background is estimated by measuring the mass spectra with like-sign pions, that is, $J/\psi\pi^+\pi^+$ and $J/\psi\pi^-\pi^-$, which is also shown in Fig. 2 in red.
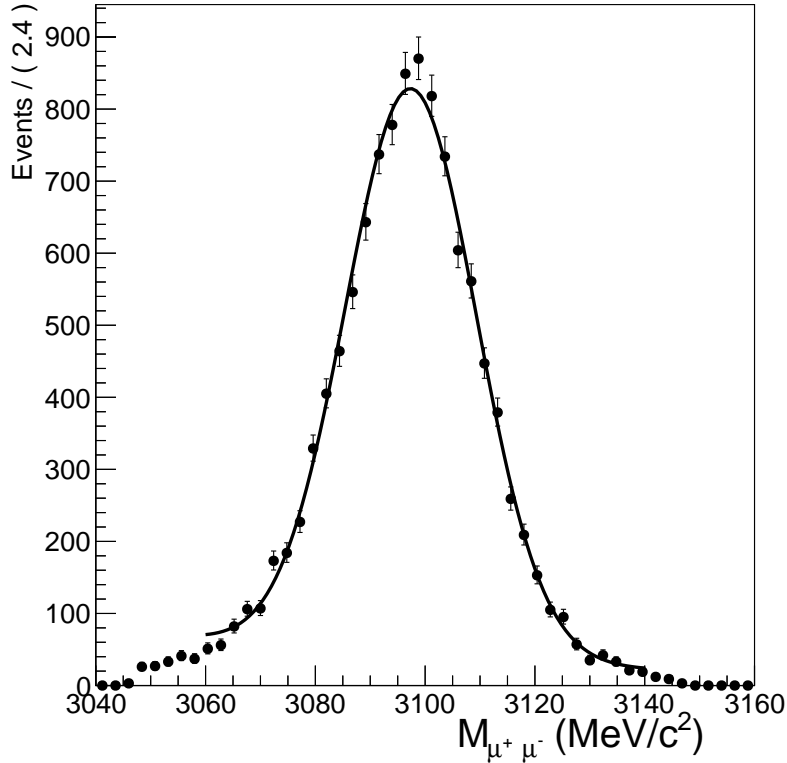

Figure 1: Invariant mass distribution of dimuons prepared using the described selections, fit with a Gaussian. The width extracted from the fit is 11.96±0.15 MeV/c^2.

DecayTree Particle	Variable	Accepted Value
Individual $\mu^{\pm}$		
	p_T	>500 MeV
	TRCHI2DOF	< 3
	TRACK_GhostProb	< 0.3
	IsMuon	TRUE
$\mu^+\mu^-$ pair		
	$|M_{\mu^+\mu^-}|$	$< 3\sigma$ around J/ψ peak where $\sigma = 12$ MeV/c^2
	p_T	> 500 MeV/c
	ACUTDOCA	<0.5 mm
Individual $\pi^{\pm}$		
	p_T	>750 MeV/c
	p	>3 GeV/c
	TRCHI2DOF	< 3
	TRACK_GhostProb	< 0.3
	IsMuon	FALSE
	ProbNNpi	> 0.9
$\pi^+\pi^-$ pair		
	ACUTDOCA	<0.5 mm
$J/\psi\pi^+\pi^-$		
	VCHI2/VDOF	< 10
	DecayTreeFitter χ^2/NDF	<5
	ACUTDOCA between $\mu^+\mu^-$ and $\pi^+\pi^-$	<0.5 mm
	DecayTreeFitter $c\tau$	>0.75 mm
	DIRA OWNPV	>0.99
Global cuts		
	nPV==1	
	-60mm<PVZ<120mm	

Table 1: $J/\psi\pi^+\pi^-$ candidate selection cuts.

2.2 Event Activity Determination

This analysis relies on tracks reconstructed in the VELO to serve as the measure of event activity. It is therefore crucial to select events with a single primary vertex that occur in a z vertex range where the acceptance of the VELO is stable, in order to avoid biases in the track reconstruction that can induce non-physical detector effects. First we examine the distributions of the number of tracks reconstructed in the VELO for the different run periods considered here (2016, 2017, and 2018) see Fig. 3, for events from dimuon DSTs. We see that distributions are identical, so there is no variation in VELO efficiency across these data samples. We see that, for a single vertex, there is a maximum of 250 tracks per event. We compare this with the VELO tracking efficiency from the JINST paper in Fig. 4 [3], which shows that the VELO has a constant efficiency of ~99% in this range of track multiplicity.

Figure 5 shows the distribution of the number of reconstructed tracks selected from events with one primary vertex, for different ranges of the primary vertex z location
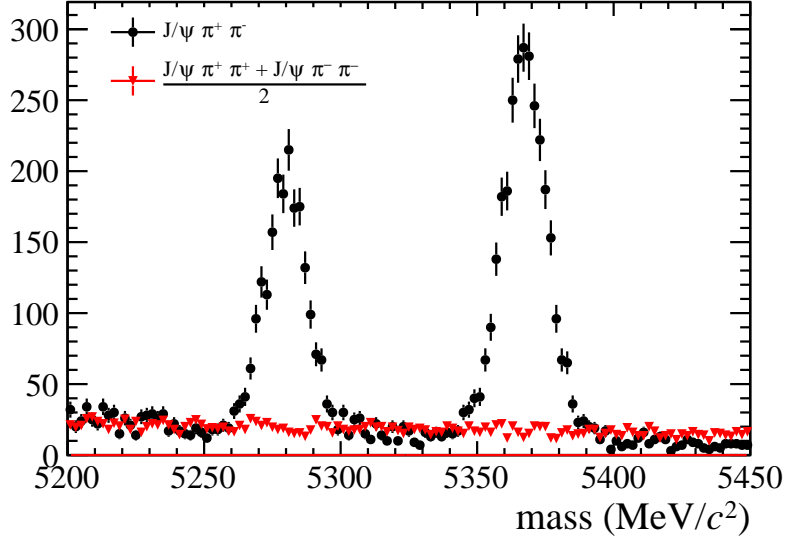
Figure 2: Invariant mass distribution of $J/\psi\pi^+\pi^-$ prepared using the described selections, showing the B^0 and B_s^0 peaks. The mass-spectrum prepared using like-sign dipions, representing the combinatorial background, is shown in red.
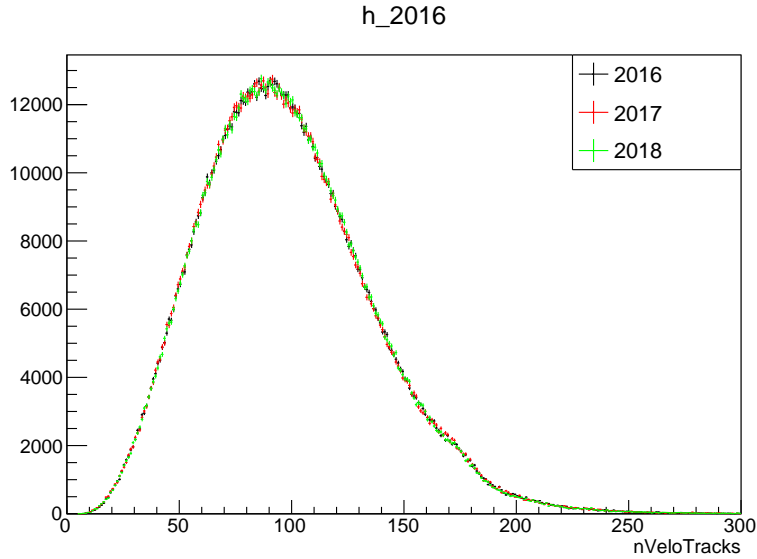

Figure 3: Distribution of the number of tracks reconstructed in the VELO, for the 2016, 2017, and 2018 data considered here.

PVZ, selected from data which contain $J/\psi\pi^+\pi^-$ candidates which pass our selection criteria. We see a common trend for most of the range of PVZ selections, indicating that in this PVZ range, the VELO acceptance is equivalent. However, at the edges of the PVZ range (PVZ<-60 mm, as indicated by the black and red points), there is a clear deviation from the other curves towards lower track multiplicity. This is due to events producing tracks that do not enter the VELO acceptance. Therefore, in this analysis, we restrict our primary vertex z range to -60 mm<PVZ<120 mm.
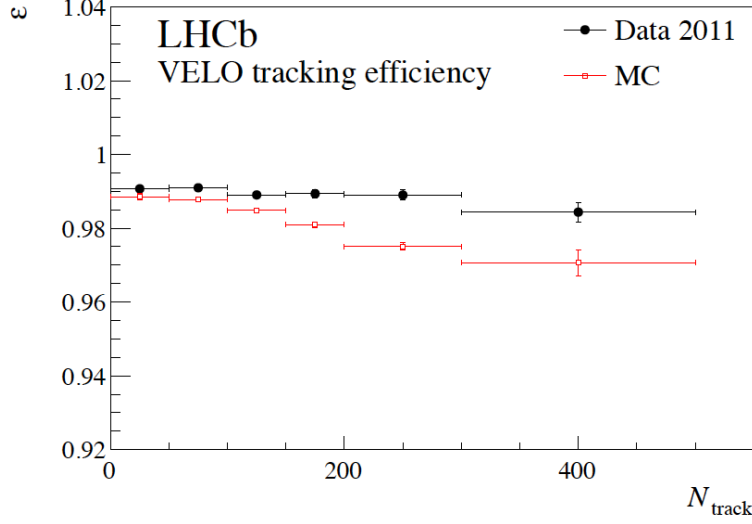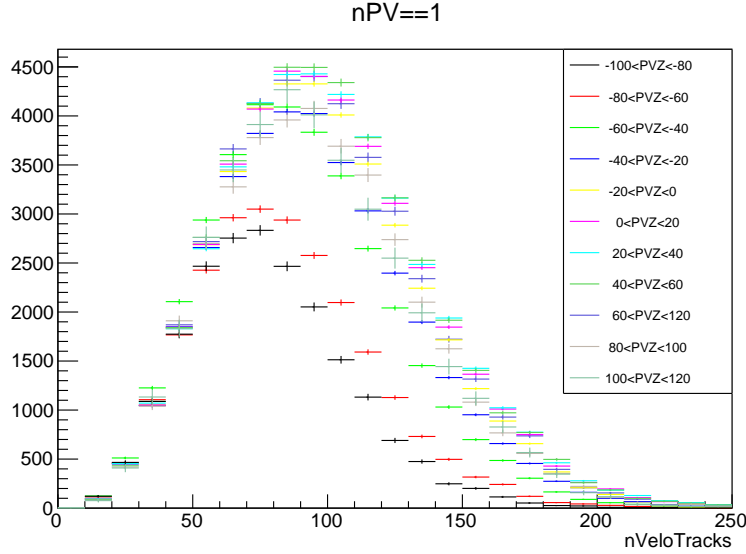
4

Figure 4: VELO tracking efficiency [3].

Figure 5: Distribution of the number of tracks reconstructed in the VELO, for different z ranges of the primary vertex, from data containing a decay candidate. To maintain constant VELO acceptance in this analysis we choose -60 mm$< z <$120 mm.

2.2.1 Comparison with NoBias Events

It is illustrative to compare the multiplicity distributions from our heavily biased data sample with unbiased data. Fig. 6 shows the N_{tracks}^{VELO} and N_{tracks}^{back} distributions for NoBias events in red (which are selected by clock triggers) and $B^0 \to J/\psi\pi^+\pi^-$ signal events in black. The NoBias distributions are selected from the event reconstruction summary (TES location \Event\Rec\Summary). We see significant differences, as expected, since events which produce B mesons are far removed from unbiased data. The NoBias data has an average VELO multiplicity of 37.70 ± 0.02 tracks and average backwards multiplicity of 11.05 ± 0.01 tracks, which will be used as a baseline for comparisons with multiplicity

p_T range	$B^0 < N_{tracks}^{VELO} >$	$B_s^0 < N_{tracks}^{VELO} >$
$0 < p_T < 6$ GeV/c	68.5±1.3	72.7±1.0
$0 < p_T < 6$ GeV/c	73.6±1.1	74.6±0.8
$0 < p_T < 6$ GeV/c	71.5±1.9	75.2±1.7

Table 2: Parameters of the fits to the B_s^0 and B^0 simulated signal shapes. The mean and width parameters m and σ are left free when fitting data, while the other parameters are fixed to these values found from simulation.

binned data in the results section.
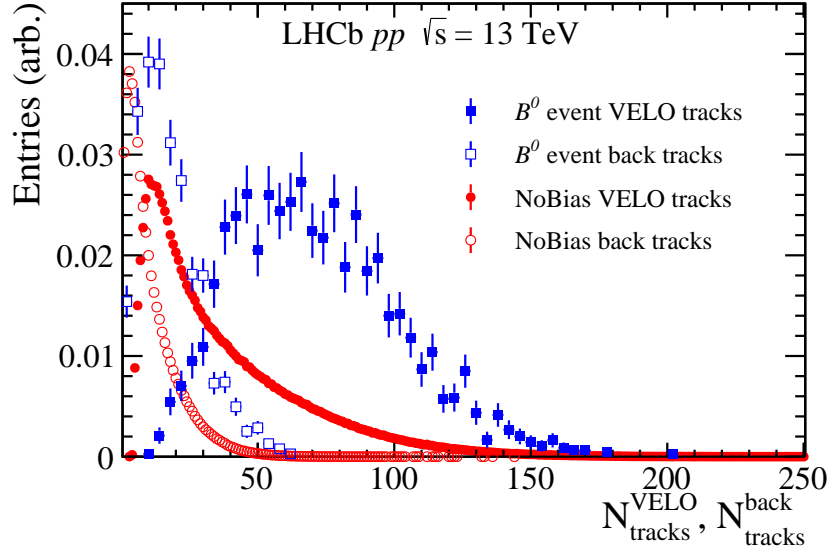
Figure 6: Distribution of the number of VELO tracks and back tracks for NoBias events (red) and B^0 signal events (blue). The vertex location and PV criteria (-60 mm$< z <$120 mm and nPV==1) are applied to all these selections.

2.2.2 Multiplicity distributions vs p_T

The variation of multiplicity distributions with p_T is also of interest. Scatter plots of the p_T vs N_{tracks}^{VELO} for B^0 and B_s^0 signals are shown in Fig. 7. There is not anything immediately apparent, but the B_s^0 multiplicity distribution may be somewhat broader than the B^0 distribution. For a more quantitative look, Fig. 8 shows the N_{tracks}^{VELO} distributions for B^0 and B_s^0 signal events in the three p_T bins considered in this analysis. The variation with p_T can be quantified by the mean number of N_{tracks}^{VELO} in each p_T bin, which is collected in Tab. 2. This data may indicate that B_s^0 production prefers slightly higher multiplicity than B^0 production, although the uncertainties preclude drawing firm conclusions from this metric alone.

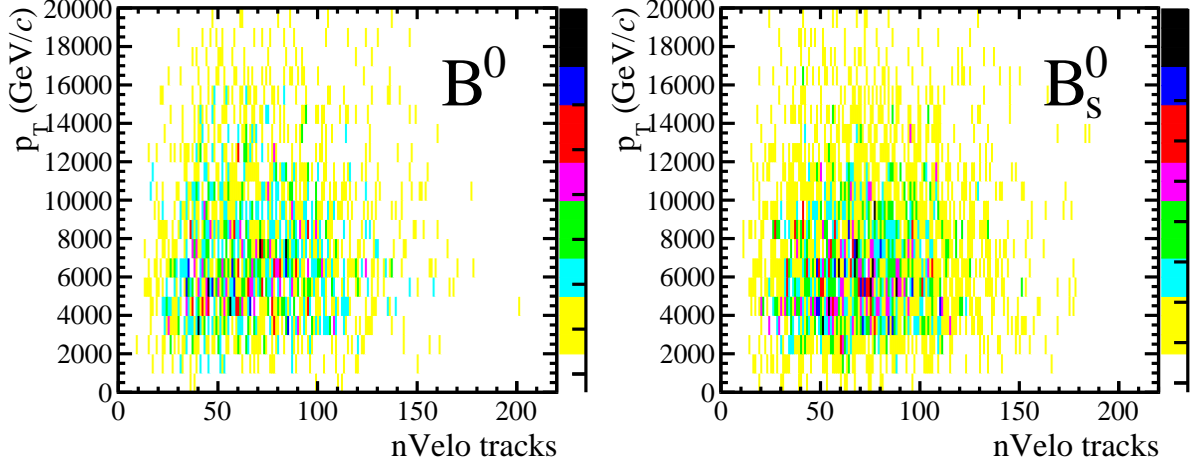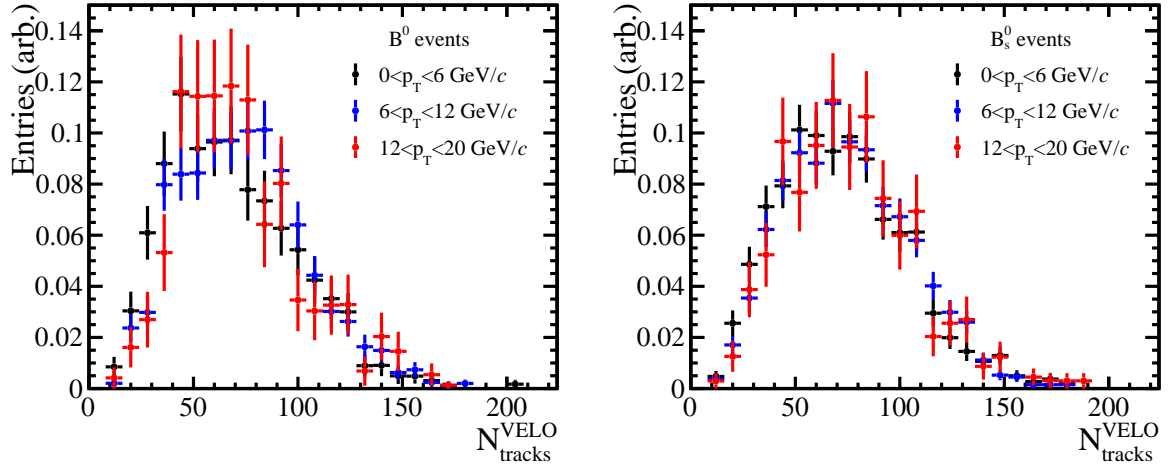Figure 7: Distribution of the number of VELO tracks for B^0 (left) and B_s^0 (right) signal events in bins of p_T. The vertex location and PV criteria (-60 mm< z <120 mm and nPV==1) are applied to all these selections.

Figure 8: Distribution of the number of VELO tracks for B^0 (left) and B_s^0 (right) signal events in bins of p_T. The vertex location and PV criteria (-60 mm< z <120 mm and nPV==1) are applied to all these selections.

3 Signal extraction

Signal yields are extracted by fitting the invariant mass spectra. The fit procedure is discussed herein.

3.1 B_s^0/B^0 extraction

Signal shapes for the B_s^0 and B^0 are determined by fitting simulation. In both cases the peaks are well described by a sum of two Crystal Ball functions, as shown in Figs. 9 and 10. In each fit, the two Crystal Ball functions are constrained to have the same mean and width, while the tail parameters an relative contribution of each Crystal Ball are

7

	μ (MeV/c^2)	σ (MeV/c^2)	n_{high}	α_{high}	n_{low}	α_{low}	fraction
B^0	5280± 0.04	7.97±0.03	1.42±0.02	1.72±0.02	3.10±0.1	-1.71±0.02	0.59±0.01
B_s^0	5367± 0.03	8.18±0.02	1.55±0.02	1.38±0.01	3.02±0.06	-1.91±0.01	0.38±0.004

Table 3: Parameters of the fits to the B_s^0 and B^0 simulated signal shapes. The mean and width parameters m and σ are left free when fitting data, while the other parameters are fixed to these values found from simulation.

allowed to vary independently. Both a low- and high-mass tail are necessary to describe the signal shape. The fit parameters are collected in Tab. 3, where n and α represent the power-law slope parameter and transition point for the high- and low-mass tails. See `RooCBShape` documentation for details on the implemented Crystal Ball functions: https://root.cern.ch/doc/master/classRooCBShape.html
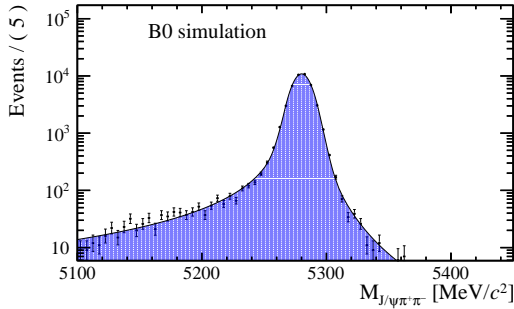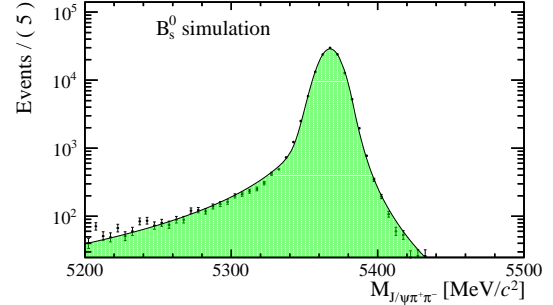

Figure 9: Fit to $B^0 \to J/\psi\pi^+\pi^-$ simulation.

Figure 10: Fit to $B_s^0 \to J/\psi\pi^+\pi^-$ simulation.

The $J/\psi\pi^+\pi^-$ data sample is divided into independent bins of event multiplicity. A simultaneous fit is performed to all bins, where the signal shapes are constrained to be the same in each multiplicity bin. The mean and width are allowed to vary, while the Crystal Ball tail parameters and relative fraction of each Crystal Ball function are fixed to the values found in simulation. The background is represented by an exponential, which describes the like-sign $J/\psi\pi^+\pi^+$ and π^-pim well, with a slope and normalization that is allowed to vary independently in each bin. An example of the resulting fits is shown in Fig. 11, and all the individual fits are shown in the appendix Sec. A. The resulting ratio of B_s^0/B^0 counts versus multiplicity is shown in Fig. 12, and the yields in each multiplicity bin are shown in Tab. 4 for the p_T-integrated sample, and Tabs 5 though 8 for the various p_T bins.

As a crosscheck, the fits are repeated with the fixed parameters for the B^0 and B_s^0 peak shapes swapped, i.e. the parameters extracted from the B_s^0 simulation are used to fit the B^0 and vice-versa. This changes the extracted values of the ratio of B_s^0/B^0 counts by less than one percent in each multiplicity bin, which is negligible.

3.2 Removal of $K_s^0 \to \pi^+\pi^-$ contribution to B^0 yield

The goal of this analysis is to measure the ratio of B_s^0 to B^0 cross sections. This measurement must therefore be corrected for the branching fraction of B^0 decays to

N^{VELO}_{tracks}	B^0_s counts	B^0 counts	background counts	χ^2/NDF
5-20	36.8586 ± 6.34493	29.8272 ± 5.99712	11.3288 ± 4.81688	1.04129
21-30	126.198 ± 11.967	79.5974 ± 10.032	42.2119 ± 9.36913	1.40848
31-40	219.621 ± 16.0309	163.786 ± 14.1495	95.6137 ± 13.3476	1.14251
41-50	308.108 ± 18.9077	211.649 ± 16.1923	133.222 ± 15.7069	1.49713
51-60	347.302 ± 20.3094	217.729 ± 16.9245	185.94 ± 18.396	1.03665
61-70	363.515 ± 20.8864	229.557 ± 17.431	222.886 ± 19.7416	0.801035
71-80	363.617 ± 20.8044	210.138 ± 16.7185	199.215 ± 18.8907	1.49064
81-100	589.433 ± 26.6063	349.318 ± 21.3608	311.111 ± 23.8844	1.43473
101-125	414.611 ± 22.345	230.746 ± 17.7689	273.595 ± 21.5358	0.938066
126-150	156.564 ± 13.7342	79.134 ± 10.2975	82.285 ± 12.2273	1.09318
151-250	40.5375 ± 7.02236	21.2781 ± 5.54784	31.1635 ± 7.14685	1.31692

Table 4: Fit summary for the p_{T}−integrated data sample.

N^{VELO}_{tracks}	B^0_s counts	B^0 counts	background counts	χ^2/NDF
5-20	18.2122 ± 4.38734	18.8239 ± 4.52475	3.97327 ± 2.1641	2.71373
21-30	64.2063 ± 8.55374	43.1366 ± 7.49887	27.628 ± 7.2488	1.57377
31-40	93.9295 ± 10.9881	71.1873 ± 9.81497	78.8674 ± 11.731	1.20796
41-50	116.779 ± 12.015	88.0543 ± 10.682	89.1756 ± 12.2088	1.67429
51-60	138.522 ± 13.4893	80.295 ± 11.0505	142.195 ± 15.4379	1.21473
61-70	124.75 ± 12.9877	79.328 ± 11.0357	172.912 ± 16.4175	0.762238
71-80	145.787 ± 13.7553	58.979 ± 9.67456	143.254 ± 15.1761	1.72197
81-90	222.97 ± 17.1795	114.648 ± 13.1391	222.403 ± 19.2333	0.914737
101-125	164.754 ± 15.0066	78.6578 ± 11.3233	224.53 ± 18.6109	0.939373
126-150	50.9383 ± 8.26364	20.5057 ± 5.76594	60.546 ± 9.68138	1.03832
151-250	20.2492 ± 5.09244	7.81923 ± 3.67558	22.9321 ± 5.91678	1.43001

Table 5: Fit summary for the data in the range $0 < p_{\mathrm{T}} < 6$ GeV/c.

N^{VELO}_{tracks}	B^0_s counts	B^0 counts	background counts	χ^2/NDF
5-20	17.2552 ± 4.1909	12.1063 ± 3.59521	0.639121 ± 1.20975	0.817746
21-30	49.0541 ± 7.07989	32.5153 ± 5.87072	8.43155 ± 3.12139	0.765033
31-40	105.669 ± 10.3786	77.2239 ± 9.12611	8.10836 ± 3.72451	2.28967
41-50	149.876 ± 12.7174	83.6581 ± 10.0734	27.4665 ± 8.12905	1.11304
51-60	157.126 ± 13.0786	107.067 ± 11.2781	31.8085 ± 8.55935	1.1035
61-70	181.957 ± 14.1217	95.755 ± 10.7236	41.2884 ± 9.19486	1.41513
71-80	166.038 ± 13.2311	119.699 ± 12.3229	37.263 ± 9.42093	1.42208
81-100	286.199 ± 17.7763	189.155 ± 15.0229	65.6459 ± 12.1741	1.55102
101-125	199.729 ± 14.5697	120.936 ± 12.0927	26.3343 ± 8.74914	0.949523
126-150	76.9672 ± 9.39173	41.3151 ± 7.12435	13.7185 ± 6.30266	1.10413
151-250	16.1705 ± 4.07164	14.8739 ± 3.91279	0.95698 ± 0.999628	4.32217

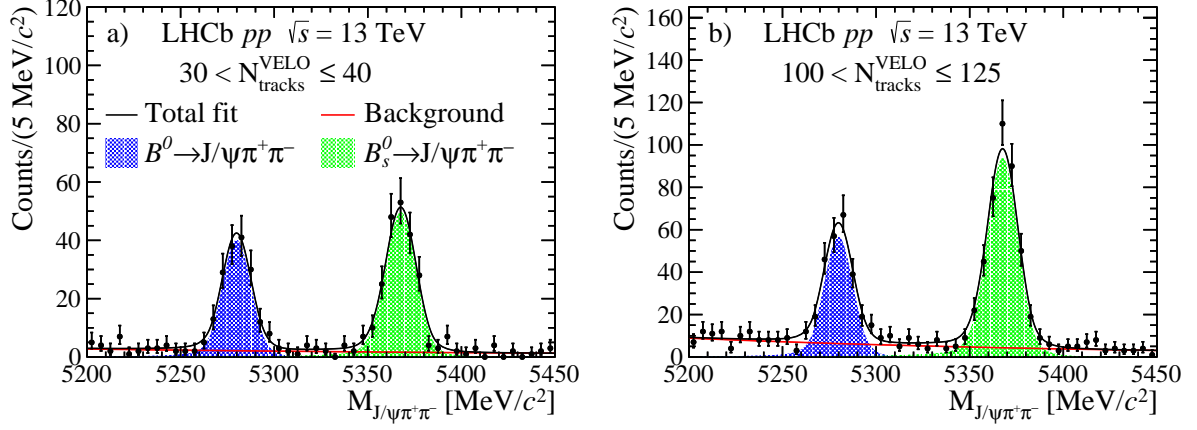Table 6: Fit summary for the data in the range $6 < p_{\mathrm{T}} < 12$ GeV/c.

Figure 11: Example fits to $J/\psi\pi^+\pi^-$ mass distribution in low and high multiplicity bins. An increase of the B_s^0 yield relative to the B^0 yield is apparent.
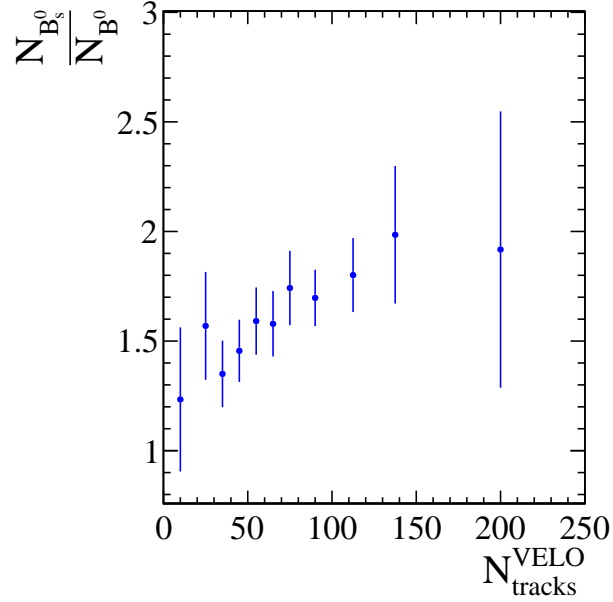

Figure 12: The ratio of B_s^0/B^0 counts found by fitting the $J/\psi\pi^+\pi^-$ data.

N_{tracks}^{VELO}	B_s^0 counts	B^0 counts	background counts	χ^2/NDF
5-30	16.7248 ± 4.41185	7.55553 ± 3.20199	4.71449 ± 3.42288	1.34115
31-50	58.8276 ± 7.78653	54.3063 ± 7.73845	7.89128 ± 3.9557	1.26259
51-70	88.9679 ± 9.51195	82.1839 ± 9.46953	9.8776 ± 4.23027	1.59184
71-90	93.8675 ± 10.1157	54.4287 ± 7.87484	14.7153 ± 5.84037	1.55914
91-125	70.049 ± 8.74242	48.028 ± 7.86692	20.8856 ± 6.84815	1.31457
126-250	27.4128 ± 5.3678	16.4376 ± 4.5214	6.1561 ± 3.49324	0.881664

Table 7: Fit summary for the data in the range $12 < p_T < 20$ GeV/c.

10

N_{tracks}^{back}	B_s^0 counts	B^0 counts	background counts	χ^2/NDF
0-10	713.677 ± 29.0882	478.797 ± 25.2539	442.506 ± 27.7685	1.46803
11-15	592.076 ± 26.3072	371.292 ± 21.7914	290.686 ± 22.8001	1.20988
16-20	535.965 ± 25.0489	292.282 ± 19.5953	275.797 ± 21.9416	1.29806
21-25	374.618 ± 21.0631	233.57 ± 17.4513	234.822 ± 19.7751	1.59811
26-30	267.624 ± 17.6613	171.126 ± 14.7264	139.279 ± 15.5009	1.41023
31-40	313.14 ± 19.3277	176.338 ± 15.4414	193.566 ± 18.1937	1.69609
41-60	153.382 ± 13.4179	94.0845 ± 11.071	79.5256 ± 11.889	1.25811

Table 8: Fit summary for the data in the range $0 < p_\mathrm{T} < 20$ GeV/c as a function of N_{tracks}^{back}.

$J/\psi\pi^+\pi^-$ to give the total yield. In the literature, the contribution from the decays $B^0 \to J/\psi K_s^0$, where the daughter K_s^0 subsequently decays to $\pi^+\pi^-$, are excluded from the total branching fraction of B^0 decays to $J/\psi\pi^+\pi^-$ [4,5]. Therefore, for consistency when using the previously measured branching fractions, the contribution from $B^0 \to J/\psi K_s^0(\to \pi^+\pi^-)$ must be removed from this measurement.

Using the method of sWeights, the dipion mass distribution for signal B^0 decays is extracted from the data (see Sec. 4.1 for details), and shown in Fig. 13. Various structures, including the K_s^0 at ~500 MeV/c^2, are apparent. A local fit of the region containing the K_s^0 region is performed and shown in Fig. 14, where the peak is represented by Gaussian and the background by an exponential. The mean value of the Gaussian is found to be 497.8$±0.5MeV/c^2$, in good agreement with the known neutral kaon mass of 497.611±0.013 MeV/c^2 The fit returns the fraction of all dipions which are in the K_s^0 peak, which is found to be 2.3%±0.5% of the total. To exclude these decays, the measured B^0 yield is decreased by 2.3%, and the 0.5% uncertainty on the correction is taken as a systematic uncertainty. As a cross-check, the same procedure is followed for low- and high-multiplicity data sample (defined as having less than or greater than 75 tracks) and returns contributions of 2.7%±0.7% and 2.0±0.8%, which are consistent with the multiplicity-integrated sample.
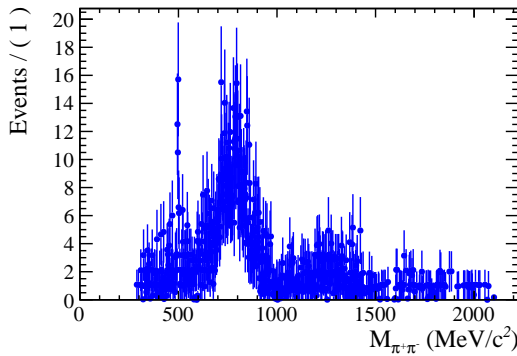

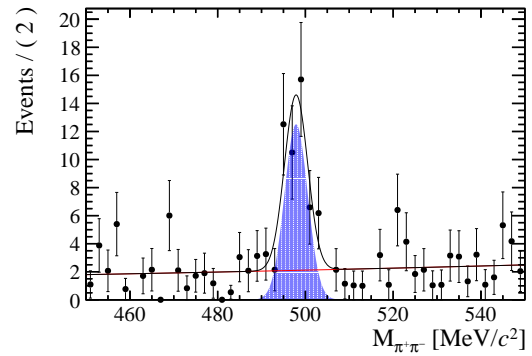Figure 13: The dipion mass distribution from $B^0 \to J/\psi\pi^+\pi^-$ decays.

Figure 14: Fit to the K_s^0 peak in the $\pi^+\pi^-$ mass distribution.

Due to the kinematics of the decay process and variations of the reconstruction efficiency with dipion kinematics, the fraction of dipions from K_s^0 decays may vary with

¹⁵² parent B^0 meson p_T. To study this, the above procedure for finding the K_s^0 fraction is
¹⁵³ repeated in the bins B^0 meson p_T used in this analysis: 0-6, 6-12, and 12-20 GeV/c^2, and
¹⁵⁴ the fits are shown in Figs. 15 through 17. The results are collected in Tab. 9; in all cases
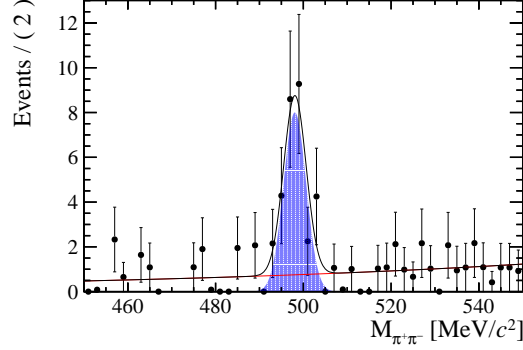¹⁵⁵ the corrections and uncertainties are small and subdominant.

Figure 15: Fit to the K_s^0 peak in the $\pi^+\pi^-$ mass distribution for B^0 in the range $p_\mathrm{T} <$6 GeV/c.
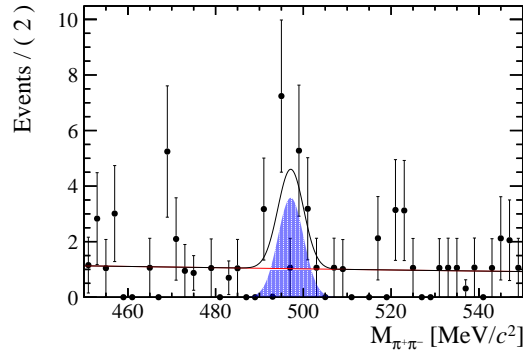
Figure 16: Fit to the K_s^0 peak in the $\pi^+\pi^-$ mass distribution for B^0 in the range $6< p_\mathrm{T} <$12 GeV/c.
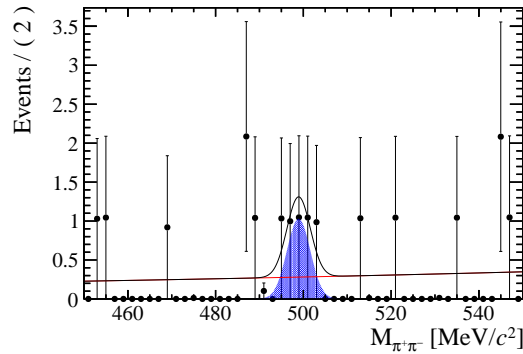
Figure 17: Fit to the K_s^0 peak in the $\pi^+\pi^-$ mass distribution for B^0 in the range $12< p_\mathrm{T} <$20 GeV/c.

12

B^0 p_{T} range	dipion fraction in K_s^0
p_{T} <20 GeV/c	2.3%±0.5%
p_{T} <6 GeV/c	4.1%±0.9%
6< p_{T} <12 GeV/c	1.6%±0.5%
12< p_{T} <20 GeV/c	1.3%±0.9%

Table 9: Fraction of dipions under the K_s^0 peak in bins of B^0 meson p_{T}.

3.3 Cross check:Primary Vertex Reconstruction

In order to characterize each event, a selection on the number of reconstructed primary vertices nPV=1 is made, to avoid track contributions from multiple PVs that occur in the same beam crossing (pile up). However, the average LHCb primary vertex reconstruction efficiency has been determined to be $\sim$ 94% for minimum bias events [6], so in some events with multiple PVs, only a single PV will be reconstructed, contaminating the sample of actual single PV events. This effect is studied in Monte Carlo by preparing a set of simulated PVs, assigning each a number of tracks and z vertex, and applying efficiency curves from [6], as shown in Fig. 20, to these simulated events. Thereby the amount of contamination in each bin of nVeloTracks from neighboring bins with an unreconstructed PV can be quantified. Spoiler alert: the effect is negligible.

The simulation samples consist of 10^7 events. To construct these simulated events, first a number of PVs is chosen by randomly sampling from a distribution of nPV taken from the DIMUON stripped data considered here, shown in Fig. 18. Each PV in an event is assigned a z coordinate by randomly sampling from the PVZ distribution obtained from the data to obtain the generated PV distributions shown in Fig. 19. Similarly, each vertex is also assigned a track multiplicity: one vertex (representing the signal event) is assigned a multiplicity by randomly sampling from the measured track multiplicity from B^0 data shown in Fig. 6. The other vertices in the event are assigned a multiplicity by randomly sampling from the NoBias track multiplicity distribution shown in the same figure. Following the definitions in [6], the generated primary vertices are characterized as "isolated" if their assigned z position is greater than 10 mm from any other PV in the event, and characterized as "close" if they are less than 10 mm from any other PV. The reconstruction efficiencies for close and isolated PVs from [6] shown in Fig. 20 is applied to each PV, depending on its isolation status.

From these simulated samples, events are selected which have exactly one reconstructed primary vertex. These selected events are binned according to the track multiplicity assigned to this reconstructed vertex, and the total track multiplicity of the event, defined as the sum of tracks from all PVs in the event (reconstructed plus non-reconstructed), is plotted in Fig. 21 for each bin. We see that the majority of events are correctly identified, however there are some events with at least one unreconstructed primary vertex that would be incorrectly identified as a higher multiplicity single PV event and placed in the wrong bin. Most of this bin migration moves data into the neighboring higher bin, due to the relatively low efficiency for reconstructing vertices with < 10 tracks and our bin widths of 10 tracks or greater. The fraction of truth events in each measured bin is given in Tab. 10. We see there is contamination from neighboring bins of $\sim$several percent.

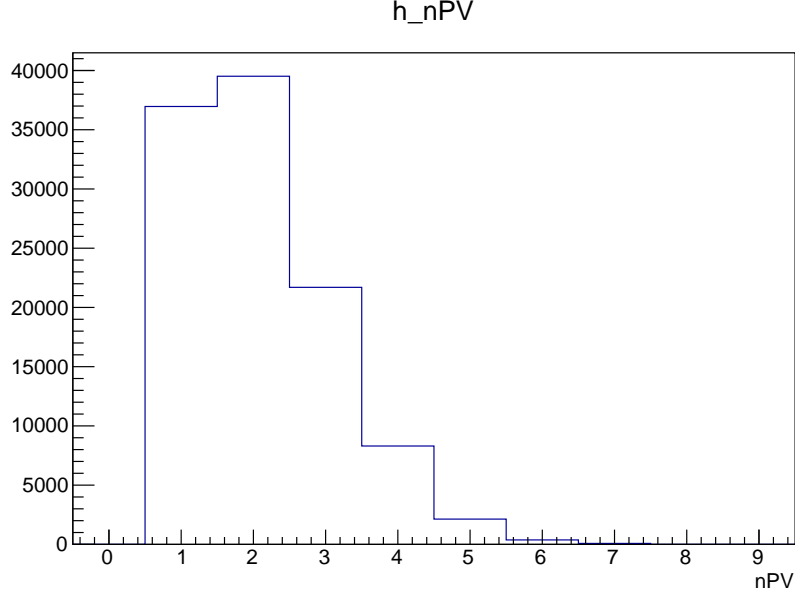The true values of the B_s^0/B^0 cross section ratio in each multiplicity bin can be

Figure 18: The number of primary vertices distribution from the data considered in this analysis. Random sampling from this distribution is used to set number of primary vertices (nPV) values used in the Monte Carlo simulation.
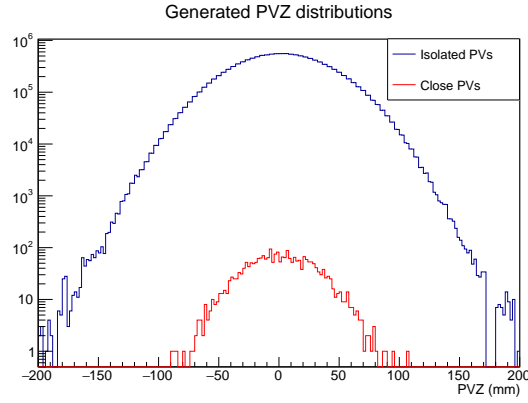

Figure 19: Primary vertex z (PVZ) values of the close and isolated generated PVs.

unfolded from the data as follows: A measurement M_i in the ith multiplicity bin will consist of a linear combination of data which correctly is identified as coming from that multiplicity bin plus contributions from other bins which are incorrectly placed due to an unreconstructed PV, which are weighted by their relative contributions to the ith bin. For example, in the bin corresponding to the 51-60 track multiplicity, the measurement in that bin is described by

$$M_4 = f_{0in4}Y_0 + f_{1in4}Y_1 + f_{2in4}Y_2 + f_{3in4}Y_3 + f_{4in4}Y_4 \tag{1}$$

where f_{jin4} is the fraction of events placed in bin 4 that actually come from bin j,

14
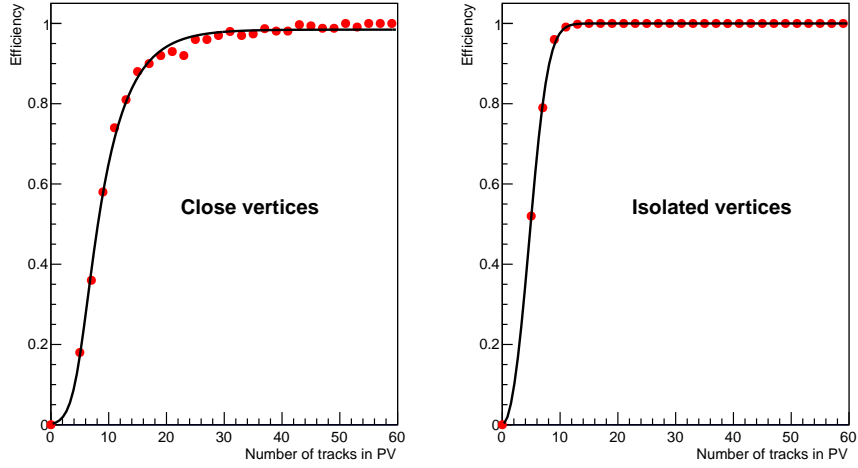
Figure 20: Efficiencies for reconstructing "close" and "isolated" primary vertices, from [6].
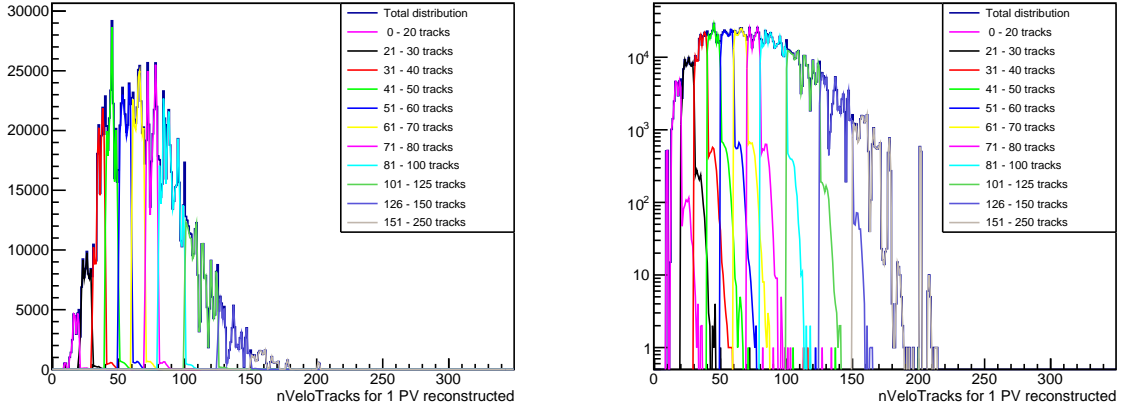
Figure 21: Distribution of number of tracks when selecting 1 reconstructed PV, with the specified number of tracks from that reconstructed PV. Both panels show the same plot in a linear (left) and log (right) vertical axis scale.

given in Tab. 10, and Y_i is the true measurement in bin i. Equivalently, this can be expressed in matrix form as

$$
\begin{pmatrix}
1 & 0 & 0 & 0 & 0 & \\
f_{0in1} & f_{1in1} & 0 & 0 & 0 & 0 \\
f_{0in2} & f_{1in2} & f_{2in2} & 0 & 0 & 0 \\
f_{0in3} & f_{1in3} & f_{2in3} & f_{3in3} & 0 & 0 \\
f_{0in4} & f_{1in4} & f_{2in4} & f_{3in4} & f_{4in4} & 0 \\
f_{0in5} & f_{1in5} & f_{2in5} & f_{3in5} & f_{4in5} & f_{5in5}
\end{pmatrix}
\times
\begin{pmatrix}
Y_0 \\
Y_1 \\
Y_2 \\
Y_3 \\
Y_4 \\
Y_5
\end{pmatrix}
=
\begin{pmatrix}
M_0 \\
M_1 \\
M_2 \\
M_3 \\
M_4 \\
M_5
\end{pmatrix}
$$

(2)

15

Bin	5-20	21-30	31-40	41-50	51-60	61-70	71-80	81-100	101-125	126-150	151-250
5-20	1	0	0	0	0	0	0	0	0	0	0
21-30	0.06	0.93	0	0	0	0	0	0	0	0	0
31-40	0	0.03	0.97	0	0	0	0	0	0	0	0
41-50	0	0	0.07	0.93	0	0	0	0	0	0	0
51-60	0	0	0	0.05	0.95	0	0	0	0	0	0
61-70	0	0	0	0	0.07	0.93	0	0	0	0	0
71-80	0	0	0	0	0	0.04	0.96	0	0	0	0
81-100	0	0	0	0	0	0	0.04	0.96	0	0	0
101-125	0	0	0	0	0	0	0	0.06	0.94	0	0
126-150	0	0	0	0	0	0	0	0	0.09	0.91	0
151-250	0	0	0	0	0	0	0	0	0	0.055	0.945

Table 10: Relative contributions in each measured multiplicity bin from truth multiplicity bins.

This therefore gives a system of equations which can be solved for the quantities of interest Y_i via matrix inversion (there should actually be 11 rows and columns, corresponding to the 11 multiplicity bins used here, but we only show 0-5 for simplicity). We note that in the case of the first bin, corresponding to the lowest number of tracks, $M_0 = Y_0$, since there can be no migration to bins of lower multiplicity ($f_{0in0} = 1$). The diagonal row of Tab. 10 gives the fraction of true events in each bin, which is greater than 90% in all cases. Therefore the possible bin migration effects are expected to be small.

This formalism is applied to the p_{T}-integrated ratio of B_s^0/B^0 counts measured as a function of multiplicity shown in Fig. 12. The results are collected in Tab. 11. In each bin, the effect is less than 1/10th the magnitude of the statistical uncertainty on the measurement of B_s^0/B^0, and is therefore negligibly small.

Bin	B_s^0/B^0 before correction (M_i)	B_s^0/B^0 after correction (Y_i)	change in value
5-20	1.23	1.23	0
21-30	1.58	1.60	1%
31-40	1.34	1.33	0.6%
41-50	1.46	1.47	0.7%
51-60	1.60	1.61	0.4%
61-70	1.58	1.58	0.1%
71-80	1.73	1.74	0.3%
80-100	1.69	1.69	0.1%
100-125	1.80	1.81	0.4%
126-150	1.98	1.99	0.8%
151-250	1.91	1.90	0.3%

Table 11: Effect of multiplicity bin migration due to missing PV reconstruction, using the p_{T}-integrated data sample.

4 Efficiencies

The goal of this analysis is to determine the ratio of the cross sections $\sigma_{B_s^0}/\sigma_{B^0}$. The $\sigma_{B_s^0}/\sigma_{B^0}$ ratio is given by:

$$\frac{\mathcal{B}[B_s^0 \to J/\psi\pi^+\pi^-]}{\mathcal{B}[B^0 \to J/\psi\pi^+\pi^-]} \times \frac{\sigma_{B_s^0}}{\sigma_{B^0}} = \frac{N_{B_s^0}}{N_{B^0}}\frac{\epsilon_{B^0}}{\epsilon_{B_s^0}} \tag{3}$$

where N_{B^0} and $N_{B_s^0}$ are the number of B^0 and B_s^0 counts extracted by fitting the peaks in the $J/\psi\pi^+\pi^-$ mass spectra, $\frac{\epsilon_{B^0}}{\epsilon_{B_s^0}}$ is the ratio of the efficiencies for reconstructing those states, and the branching fractions $\mathcal{B}$ reflect the fact that these measurements are made in the $J/\psi\pi^+\pi^-$ decay channel. The efficiencies can in turn be factorized into several independent terms:

$$\frac{\epsilon_{B^0}}{\epsilon_{B_s^0}} = \frac{\epsilon_{B^0}^{acc}\epsilon_{B^0}^{trig}\epsilon_{B^0}^{rec}\epsilon_{B^0}^{PID}}{\epsilon_{B_s^0}^{acc}\epsilon_{B_s^0}^{trig}\epsilon_{B_s^0}^{rec}\epsilon_{B_s^0}^{PID}}, \tag{4}$$

where ϵ^{acc} is the acceptance of the LHCb spectrometer for the given decay, ϵ^{trig} is the efficiency for triggering on the given decay, ϵ^{rec} is the efficiency for selecting and reconstructing the parent particle, and ϵ^{PID} is the total particle ID efficiency for the daughters of the decay.

In this section we describe each of these efficiencies that are required to determine the ratio of the cross sections in the transverse momentum range $p_{\mathrm{T}} > 0$ GeV/c and rapidity range $2 < y < 4.5$. Monte Carlo simulations using the PYTHIA8 event generators coupled to full GEANT4 simulations of the LHCb detector are used to determine the acceptance, reconstruction, and selection efficiencies. The momentum distributions used in the simulations are reweighted to match the momentum distributions extracted from the data by the method of sWeights [7], which uses the previously described fits to the invariant mass spectrum as the discriminating variable between signal and background. Corrections are applied to the efficiencies determined from the Monte Carlo simulations in order to reflect differences measured between the MC and data. Calibrated data samples from the PIDCalib package (available at https://twiki.cern.ch/twiki/bin/view/LHCb/PIDCalibPackage) are used to determine the muon and pion identification efficiencies. The trigger efficiencies are determined from the data via the TISTOS method. Systematic uncertainties on these corrections are discussed in the relevant subsections.

4.1 sWeighted signal

The method of sWeights is commonly used to statistically unfold the distribution of signal and background events in a data sample (see Ref. [7] and https://indico.cern.ch/event/257864/contributions/1587661/attachments/453353/628570/sweff.pdf for details). Here we use the invariant mass of the $J/\psi\pi^-\pi^-$ candidates as the discriminating variable for separating signal and background, via the fits that were previously discussed. This method is used to extract p_{T} and nSPDhits distributions and $\pi^+\pi^-$ invariant mass spectra from the data (see Figs. 22, 23 and 24). We note here that the $\pi^+\pi^-$ mass distribution from B_s^0 is dominated by the $f(980)$ and $f(1500)$ components, while the $\pi^+\pi^-$ pairs from B^0 are dominated by the $\rho(770)$ resonance, and are generally

lower mass, as was observed in LHCB-PAPER-2013-069 and LHCB-PAPER-2014-012 respectively. The simulations are weighted to match the distributions taken from data to ensure an accurate representation of reality.
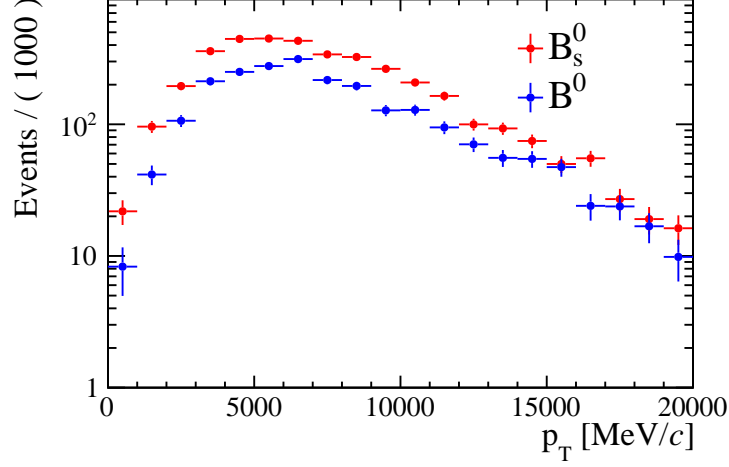

Figure 22: The p_T distributions of B_s^0 and B^0 signals extracted from the data set.
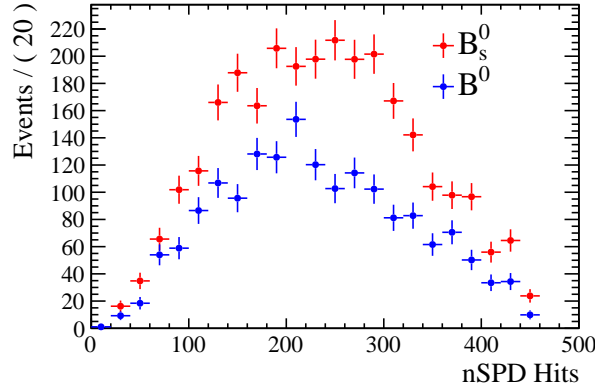

Figure 23: The nSPD Hits distributions extracted from the $B_s^0, B^0 \to J/\psi \pi^+ \pi^-$ data.

4.2 LHCb Acceptance Correction

First, we consider the acceptance for particles which are produced in our selected range of transverse momentum, rapidity, and primary vertex z range to produce daughters that are within the LHCb spectrometer solid angle, defined as 10 mrad $< \theta <$ 400 mrad. This acceptance is defined as

$$\epsilon_{acc} = \frac{\text{Number of parents in selected pt, y, PVZ range with all daughters in LHCb acceptance}}{\text{Number of parents generated in selected pt, y, PVZ range}}$$

(5)

where the selected transverse momentum range is $p_T >0$ GeV/c, the rapidity range is $2< y <4.5$, and the primary vertex z range is -60mm<PVZ<120mm. To obtain cross

18
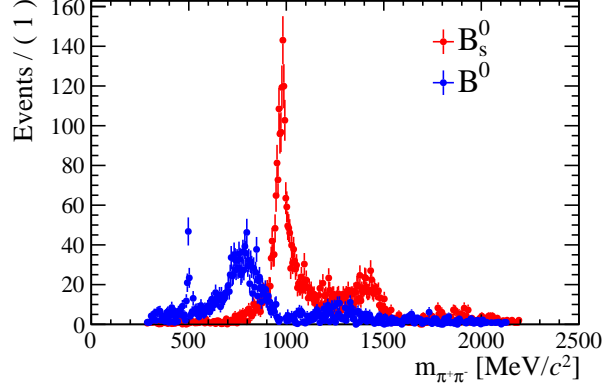
Figure 24: The $\pi^+\pi^-$ invariant mass spectra extracted from the $B_s^0, B^0 \to J/\psi\pi^+\pi^-$ data.

263 sections, the measured number of counts must be corrected by the factor $1/\epsilon_{acc}$ to account
264 for decays with some daughter products that travel outside the LHCb acceptance (in
265 addition to other corrections). This is evaluated using generator-level simulations of event
266 types 13144031 and 11144061 for B_s^0 and B^0 decays, respectively, with DecProdCuts
267 removed. From these simulations approximately 45% of the total B mesons generated
268 over 4π fall within the accepted rapidity range.

269   The kinematics of the parent, and thereby decay products, may affect the fraction of
270 accepted decays. To be sure the generator-level simulations reflect reality, the simulated p_T
271 distributions are weighted to match the distributions obtained from previous measurements
272 as follows:

273   • The shape of the B^+ and B^0 p_T distributions are expected to be the same due to
274   isospin considerations; this was confirmed at 7 TeV in [8]. The B^+ cross section in
275   13 TeV pp collisions has been measured as a function of p_T in [9]. This data is fit
276   and the simulations used here are weighted to match the measured B^0 distribution,
277   see Fig. 25.

278   • The ratio of fragmentation fractions f_s/f_d is parameterized as a function of p_T
279   in [10]. The measured B^0 p_T distribution is multiplied by this ratio to give the B_s^0
280   p_T distribution. The raw B_s^0 simulation from PYTHIA is then weighted to match
281   this resulting B_s^0 p_T distribution.

282   The resulting acceptance factors for B_s^0, B^0 decays to $J/\psi\pi^+\pi^-$, obtained using the
283 simulations weighted to match the p_T distributions of the signal from the data described
284 above, are shown as a function of p_T in Fig 26. The p_T-integrated acceptance factors are
285 determined to be $\epsilon_{acc} = 0.741$ for B^0 and $\epsilon_{acc} = 0.731$ for B_s^0.
286   A systematic uncertainty is determined by running 100 trials where the p_T distributions
287 from data are varied within their uncertainties and the simulations are reweighted to
288 match the resulting distributions. The f_s/f_d ratio is also varied when performing the
289 B_s^0 calculations. The variation is performed in each p_T bin by randomly sampling from
290 a Gaussian distribution that has a mean of the central value and width equal to the
291 uncertainty in a given bin. The weights are varied independently in each of the 100
292 trials. The results of the 100 trials are collected and the mean value of the 100 trials is
293 taken as the value of the ratio of acceptance while the standard deviation is taken as the

19
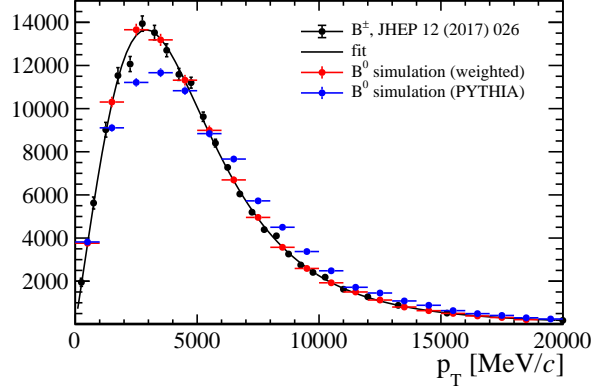
Figure 25: Measured B^+ meson p_{T} distribution (black), the simulated B^0 distribution from PYTHIA (blue), and the simulation after weighting to match the data (red).
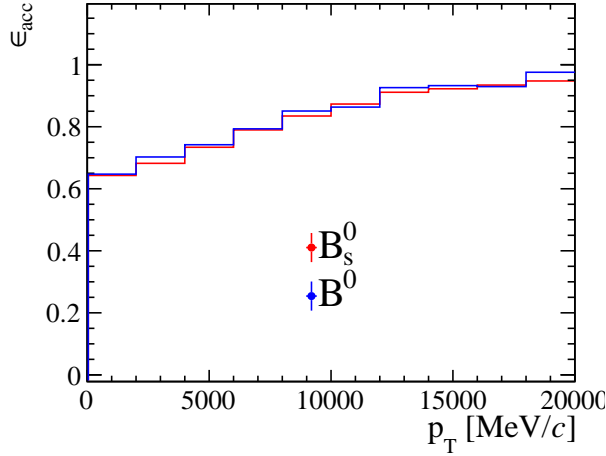
Figure 26: The acceptance ϵ_{acc} for $B_s^0, B^0 \to J/\psi \pi^+ \pi^-$ decays as a function of p_{T}.

uncertainty. In all cases, this leads to uncertainties of less than 1%. Using these methods, and rounding the uncertainty up to 1%, we find

$$\frac{\epsilon_{B^0}^{acc}}{\epsilon_{B_s^0}^{acc}} = 1.01 \pm 0.01 \tag{6}$$

for the p_{T}-integrated ratios of efficiencies. The ratios in the various p_{T} ranges used in the final results are given in Tab. 12, where an additional 1% systematic has been added to account for the finite simulation size in the p_{T} bins above 5 GeV/c.

4.2.1   Crosscheck: multiplicity dependence

If the p_{T} distributions of the B^0 and B_s^0 mesons vary significantly with multiplicity, then the kinematics of the muons and pions from their decays could be modified such that the acceptance varies. This is studied by weighting the simulated B^0 and B_s^0 p_{T} distributions to match p_{T} distributions extracted from the data in high and low multiplicity bins,

20

p_T range	ratio	value
$p_T > 0$ GeV/c	$\frac{\epsilon^{acc}_{B^0}}{\epsilon^{acc}_{B^0_s}}$	1.01±0.01
$0 < p_T < 6$ GeV/c	$\frac{\epsilon^{acc}_{B^0}}{\epsilon^{acc}_{B^0_s}}$	1.02±0.01
$6 < p_T < 12$ GeV/c	$\frac{\epsilon^{acc}_{B^0}}{\epsilon^{acc}_{B^0_s}}$	1.01±0.02
$12 < p_T < 20$ GeV/c	$\frac{\epsilon^{acc}_{B^0}}{\epsilon^{acc}_{B^0_s}}$	1.00±0.02

Table 12: Transverse momentum dependence of the ratios of acceptances.

p_T range	Multiplicity range	value
$p_T > 0$ GeV/c	$N^{tracks}_{VELO} < 75$	1.02
$p_T > 0$ GeV/c	$N^{tracks}_{VELO} > 75$	1.01
$0 < p_T < 6$ GeV/c	$N^{tracks}_{VELO} < 75$	1.03
$0 < p_T < 6$ GeV/c	$N^{tracks}_{VELO} > 75$	1.01
$6 < p_T < 12$ GeV/c	$N^{tracks}_{VELO} < 75$	1.00
$6 < p_T < 12$ GeV/c	$N^{tracks}_{VELO} > 75$	0.99
$12 < p_T < 20$ GeV/c	$N^{tracks}_{VELO} < 75$	1.00
$12 < p_T < 20$ GeV/c	$N^{tracks}_{VELO} > 75$	0.99

Table 13: Transverse momentum dependence of the ratios of acceptances $\frac{\epsilon^{acc}_{B^0}}{\epsilon^{acc}_{B^0_s}}$, with p_T distributions weighted to match data in low and high multiplicity bins.

defined as having more or less than 75 VELO tracks, respectively. The reuslts are collected in Tab. 13. For both the high and low multiplicity weightings, variations of the ratio of efficiencies $\frac{\epsilon^{acc}_{B^0}}{\epsilon^{acc}_{B^0_s}}$ are small and fall within the quoted systematic uncertainty.

4.3   Trigger Efficiencies

Candidates considered in this analysis are required to satisfy the L0Muon TOS, HLT1DiMuonHighMassDecision TOS, and HLT2DiMuonDetachedJPsiDecision TOS trigger criteria. The L0 and HLT1 triggers are hardware triggers, and their combined efficiencies are determined here from the data, following methods described in [11]. The TISTOS method uses data selected from two independent triggers, "Triggered on Signal" (TOS) and "Triggered Independent of Signal" TIS. Some events satisfy both TIS and TOS criteria (TISTOS). Therefore the TOS efficiency for J/ψ can be measured by calculating the number of events that satisfy TISTOS divided by the number that satisfy TIS:

$$\epsilon_{TOS} = \frac{N_{TISTOS}}{N_{TIS}} \tag{7}$$

We note here that the HLT2 trigger is a software selection trigger that is applied offline, and is well described by simulations. The HLT2 efficiency is therefore evaluated along with the reconstruction and selection efficiency described in the following section.

The quantities N_{TISTOS} and N_{TIS} from Eq. 7 are found by counting J/ψ candidates from each of the 6 run periods considered in this analysis (magnet up and magnet down in 2016, 2017, and 2018) by integrating the counts in the mass spectrum in a 3σ window around the J/ψ peak. These are combined by performing a weighted average of the values from each run period, where the weight is the luminosity sampled during that specific run period. The resulting efficiency curve is shown in Fig. 27.
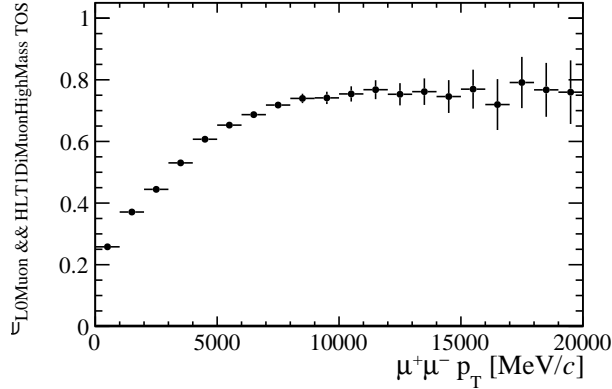
Figure 27: The L0Muon && HLT1DiMuonHighMass trigger efficiency, as a function of dimuon p_{T}.

Since the L0 and HLT1 triggers fire on the J/ψ produced in the meson decay, rather than the parent meson itself, this trigger efficiency that is measured as a function of J/ψ p_{T} must be folded with the spectrum of J/ψ produced in the decay of interest in order to produce the efficiency as a function of parent p_{T}. Monte Carlo simulations of the decays are weighted so that the parent p_{T} spectra match the previously measured distributions as described in the preceding section, and the efficiencies are applied event-by-event to produce the trigger efficiency curves as a function of parent p_{T} shown in the left panels of Fig. 28.

The right panel of Fig. 28 shows that the ratio of B^0 to B_s^0 efficiencies is close to one across the entire range of p_{T}. The masses of these hadrons differ by only ~ 90 MeV, so the kinematics of the daughter J/ψ mesons, and thus their trigger efficiencies, are very similar.

Systematic uncertainty on the relative trigger efficiency correction arises from the statistical uncertainties on the trigger efficiency, shown as error bars in Fig. 27, and uncertainties on the weights applied to the simulation in order to match the data. To account for these uncertainties, 100 independent trials are run, where in each trial the individual points on the dimuon trigger efficiency curve and the p_{T} weights in each bin are randomly varied within their uncertainties. The mean and standard deviation from the 100 trials are taken as the central value and uncertainty of the ratio of trigger efficiencies. In this case the uncertainty is small, as expected from the fact that the uncertainties on the dimuon trigger efficiency shown in Fig. 27 are small, and the fact that variations within these uncertainties have similar effects on all the decays considered, since they use the same trigger and have similar kinematics. The p_{T}-integrated ratios of trigger efficiencies are thereby found to be:
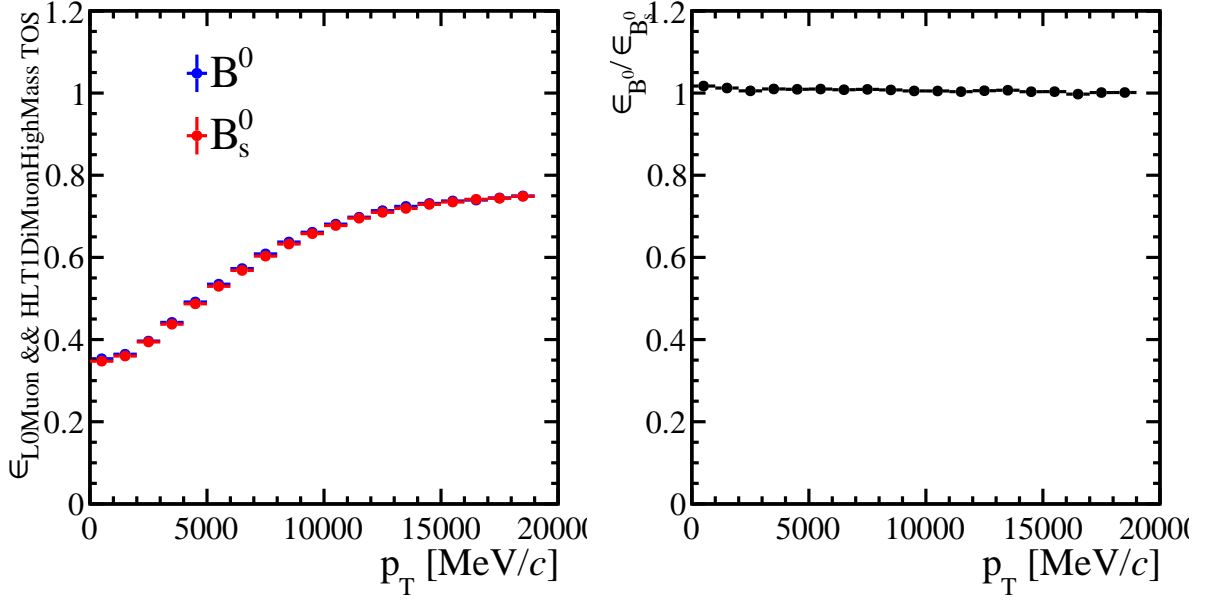
Figure 28: The L0Muon && HLT1DiMuonHighMass trigger efficiency for B_s^0 and B^0 mesons as a function of p_{T} (left), and the ratio of efficiencies (right).

p_{T} range	ratio	value
$p_{\text{T}} > 0$ GeV/c	$\frac{\epsilon_{B^0}^{trig}}{\epsilon_{B_s^0}^{trig}}$	1.01 ± 0.01
$0 < p_{\text{T}} < 6$ GeV/c	$\frac{\epsilon_{B^0}^{trig}}{\epsilon_{B_s^0}^{trig}}$	1.01 ± 0.01
$6 < p_{\text{T}} < 12$ GeV/c	$\frac{\epsilon_{B^0}^{trig}}{\epsilon_{B_s^0}^{trig}}$	1.01 ± 0.01
$12 < p_{\text{T}} < 20$ GeV/c	$\frac{\epsilon_{B^0}^{trig}}{\epsilon_{B_s^0}^{trig}}$	1.00 ± 0.01

Table 14: Transverse momentum dependence of the ratios of trigger efficiencies.

$$\frac{\epsilon_{B^0}^{trig}}{\epsilon_{B_s^0}^{trig}} = 1.01 \pm 0.01 \tag{8}$$

The ratios in the various p_{T} ranges used in the final results are given in Tab. 14.

4.4 Reconstruction and Selection Efficiencies

The next step is determining the efficiency for reconstructing and selecting the parent particles from the daughters that are in the LHC acceptance, given the selection criteria imposed by the requirements imposed by the stripping and analysis cuts. This efficiency ϵ_{rec} is defined as

23

$$\epsilon_{rec} = \frac{\text{No. reconstructed, selected, triggered parents in selected pt, y, PVZ range}}{\text{No. parents in selected pt, y, PVZ range with daughters in LHCb acceptance and triggered}}.$$

(9)

357   We use the Gauss package with the full GEANT4 simulation of the LHCb detector
358 to create simulated samples of events containing our particles of interest. The same
359 stripping selections used in the data are applied to the simulation samples, specifically,
360 the `FullDSTDiMuonJpsi2MuMuDetached` selections. PYTHIA8 is the underlying event
361 generator, using event types 13144031 and 11144061 for B_s^0 and B^0 decays, respectively.
362 Simulations are performed for the MagUp and MagDown field configurations separately.
363   Weights are applied to the simulations in order to match the distributions extracted
364 from the data via sWeights. Figs. 29 and 30 show the p_T, nSPDHits, and dipion mass
365 distributions for B^0 and B_s^0 decays extracted from the data (black), from the raw PYTHIA
366 simulations (red), and from the simulations after weighting to match the data (blue),
367 from the 2018 MagDown simulations and data. We see there is significant disagreement
368 between the raw simulations and data, which is alleviated when the weights are applied.
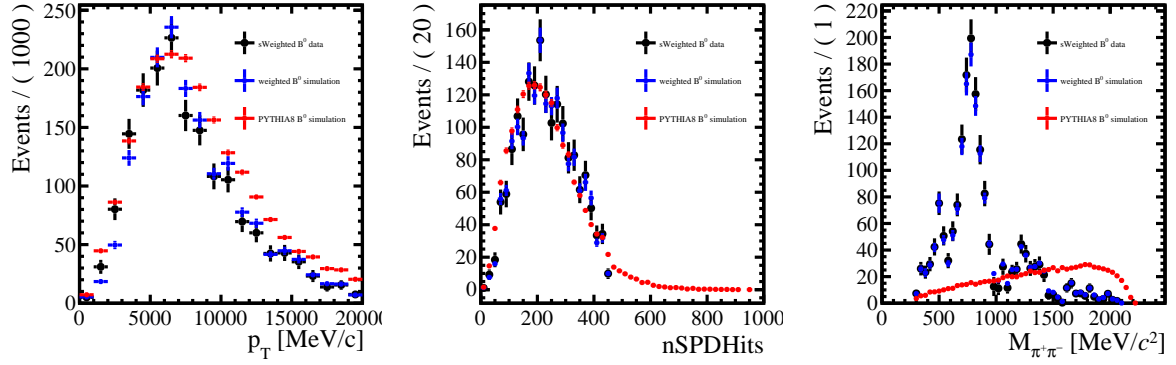
Figure 29: The p_T, nSPDHits, and dipion mass distributions for B^0 decays from the 2018 MagDown simulations before weighting (red), after weighting (blue) and the data (black).
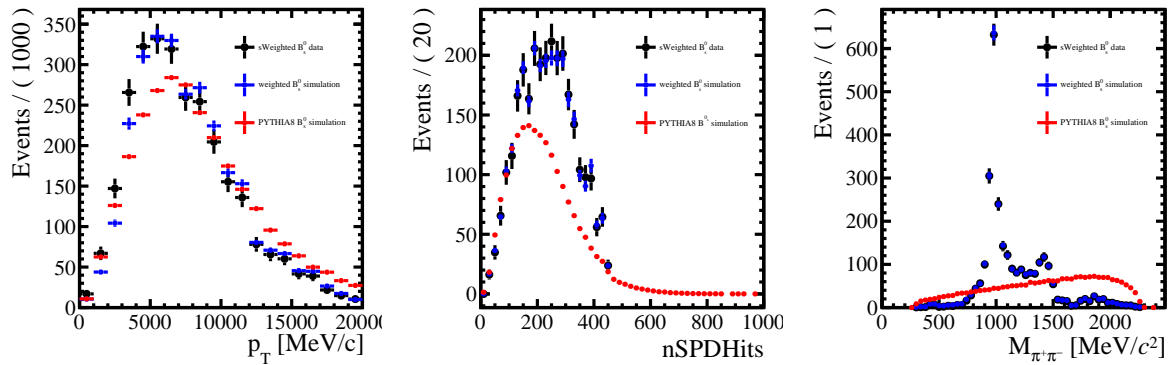
Figure 30: The p_T, nSPDHits, and dipion mass distributions for B_s^0 decays from the 2018 MagDown simulations before weighting (red), after weighting (blue) and the data (black).

369   It is known that there are slight differences between the reconstruction efficiency deter-
370 mined directly from Monte Carlo simulations, and reconstruction efficiencies determined

via tag-and-probe methods applied to the data. These differences have been extensively studied and quantified for this data set, as documented on the Tracking Efficiencies Twiki: https://twiki.cern.ch/twiki/bin/view/LHCbInternal/LHCbTrackingEfficiencies. By comparing the Monte Carlo and data, a map of correction factors has been prepared, as shown in Fig. 31. These corrections are applied track-by-track when calculating the reconstruction efficiencies, in order to correct the Monte Carlo simulations to the measured efficiencies.

To account for the uncertainties on the distributions derived from the data and the MC correction tables, sets of 100 simulation trials are run where the p_{T}, nSPDHits, dipion mass distributions, and MC corrections are randomly varied within their uncertainties. In each trial the simulations are reweighted to match the data. The reconstruction efficiency is recalculated for each trial, and the mean values of the 100 trials are taken as the central value for the reconstruction efficiency, while the standard deviation of the 100 values is taken as the uncertainty. This is done independently for each simulated run period and magnet configuration. As an example, the reconstruction and selection efficiency for B_s^0 and B^0 mesons from a single trial of the 2016 Mag Up simulation sample is shown in Fig. 32 as a function of B meson transverse momentum. The distribution of the ratio of efficiencies among the 100 trials is shown in Fig. 33 for the p_{T} bins used here. The resulting ratios of the reconstruction efficiencies are collected in Tab. 15, for each simulation set, and the final values for each p_{T} bin are collected in Tab 16. The uncertainties are dominated by the variations of the dipion mass distribution weights and p_{T} weights, each of which contribute about half of the total uncertainty in the p_{T}-integrated sample. This is expected since the MC/data track corrections and nSPD weightings largely cancel out when making the ratio efficiencies, due to the similarities of the B_s^0 and B^0 decay final states.
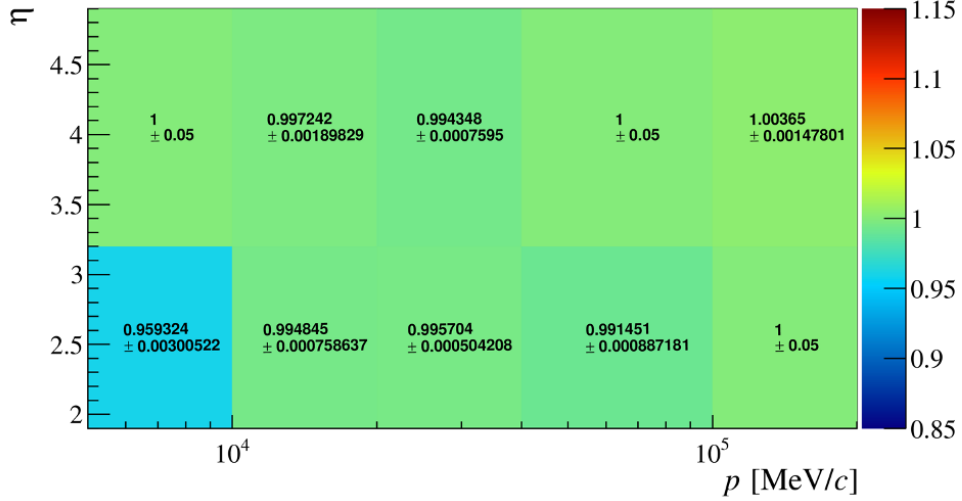
Figure 31: Map of differences between tracking efficiencies determined via data and Monte Carlo. These corrections are applied track-by-track when calculating the reconstruction efficiencies.

We see that the reconstruction ratio is slightly less than one. This is due to the difference in dipion mass distributions from the B_s^0 and B^0 decays: we see in Fig. 24 that the pion pairs from B_s^0 decays favor higher masses than the pairs from B^0 decays, as was previously studied in detail in LHCB-PAPER-2013-069 and LHCB-PAPER-2014-012. The reconstruction and selection efficiency for pion pairs from the decays of interest is shown in
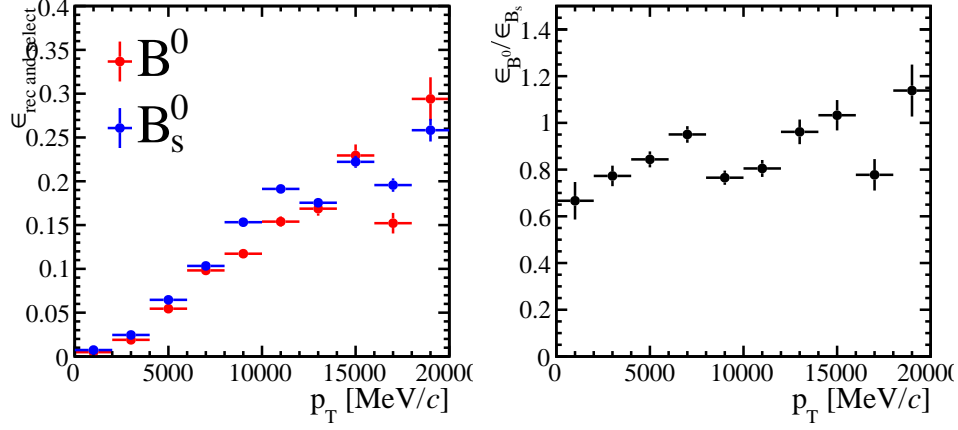
Figure 32: Left: the reconstruction and selection efficiency for B_s^0 and B^0 mesons, from a single trial run over the 2016 Mag Up simulation sample. Right: the ratio of efficiencies.
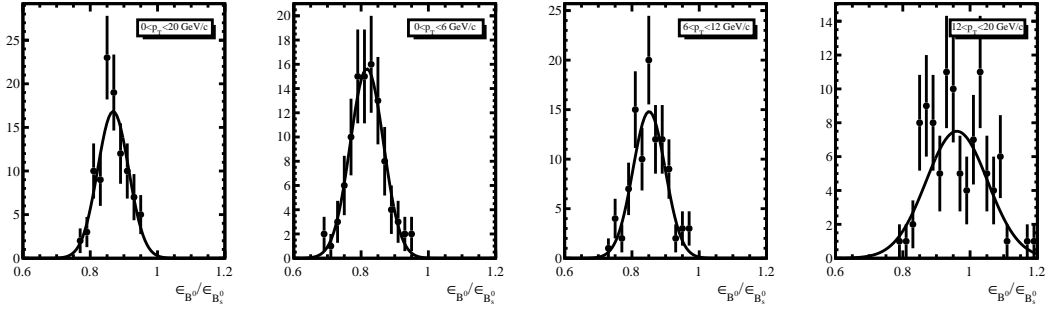
Figure 33: Distribution of B^0/B_s^0 efficiencies from 100 trials run over the 2016 Mag Up simulation sample, in various p_T bins used in the analysis. The mean±standard deviation are taken as the central value and uncertainty.

Fig. 34, where we see that the efficiency increases with dipion invariant mass. Therefore, the higher mass pion pairs from B_s^0 decays will be reconstructed with a slightly higher efficiency than the lower mass pairs from B^0 decays, giving the B_s^0 a larger reconstruction efficiency than the B^0 and driving the ratio of B^0/B_s^0 reconstruction efficiencies below one.

Year	Magnet Configuration	$\epsilon_{rec}^{B^0}/\epsilon_{rec}^{B_s^0}$
2018	up	0.87±0.04
2018	down	0.84±0.04
2017	up	0.87±0.04
2017	down	0.84±0.05
2016	up	0.86±0.04
2016	down	0.86±0.04
Weighted average:		0.86±0.04

Table 15: The ratio of reconstruction efficiencies $\epsilon_{rec}^{B^0}/\epsilon_{rec}^{B_s^0}$ in the range $p_T < 20$ GeV/c .

26

p_T range	$\epsilon_{rec}^{B^0}/\epsilon_{rec}^{B_s^0}$
$p_T <20$ GeV/c	0.86 ± 0.04
$0 < p_T <6$ GeV/c	0.81 ± 0.05
$6 < p_T <12$ GeV/c	0.85 ± 0.05
$12 < p_T <20$ GeV/c	0.96 ± 0.11

Table 16: The ratio of reconstruction efficiencies $\epsilon_{rec}^{B^0}/\epsilon_{rec}^{B_s^0}$ in the p_T ranges used here.
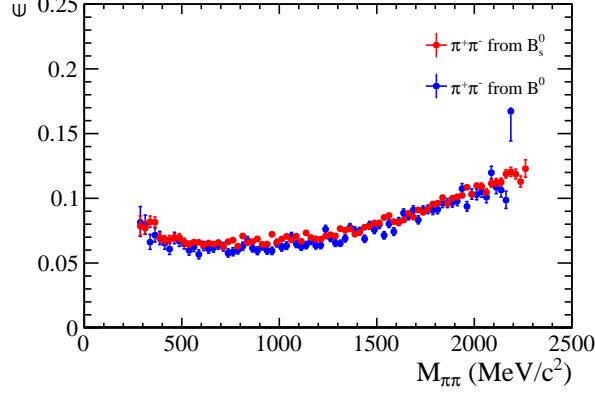
Figure 34: The efficiency for reconstructing and selecting the $\pi^+\pi^-$ pair.

4.4.1 Crosscheck: weighting in individual p_T and multiplicity bins

The preceding calculations of the relative efficiencies used simulations that are reweighted to match distributions extracted from the inclusive samples of B mesons that pass the selection criteria. However, there may exist correlations between the multiplicity and, for example, p_T and dipion mass spectra selected in the data that may affect the efficiency calculations, but are diluted in the inclusive sample. To examine any possible effects, the data are divided into high and low multiplicity samples (defined as having greater than or less than 75 Velo tracks, respectively) and the p_T, nSPDHits, and dipion mass distributions are extracted from these samples in each p_T bin considered in this analysis. The simulations are then reweighed to match these distributions, and the efficiency corrections are recalculated for each case. The resulting efficiencies are collected in Tab. 17, using the 2018 MagUp simulation sample as an example. The quoted uncertainty on the recalculated efficiencies is also given for comparison, which is found using the same methods as described above by varying the weights within their uncertainties. However we note that these uncertainties are not independent from the nominal uncertainties given on the inclusive weighted sample, as they are calculated using a subset of the inclusive data. We see that the central values of the efficiency ratios calculated using the multiplicity and p_T binned weights fall within the uncertainties of the efficiencies calculated using the inclusive weights, so any correlations are effectively accounted for and no additional systematic uncertainty is assigned.

	$0 < p_\mathrm{T} < 6\,\mathrm{GeV}/c$	$6 < p_\mathrm{T} < 12\,\mathrm{GeV}/c$	$12 < p_\mathrm{T} < 20\,\mathrm{GeV}/c$
Inclusive	0.81±0.05	0.88±0.05	0.98±0.11
Low mult $0 < p_\mathrm{T} < 6\,\mathrm{GeV}/c$	0.84±0.09		
High mult $0 < p_\mathrm{T} < 6\,\mathrm{GeV}/c$	0.85±0.1		
Low mult $6 < p_\mathrm{T} < 12\,\mathrm{GeV}/c$		0.87±0.08	
High mult $6 < p_\mathrm{T} < 12\,\mathrm{GeV}/c$		0.88±0.08	
Low mult $12 < p_\mathrm{T} < 20\,\mathrm{GeV}/c$			1.03±0.20
High mult $12 < p_\mathrm{T} < 20\,\mathrm{GeV}/c$			0.85±0.17

Table 17: The ratio of reconstruction efficiencies $\epsilon^{B^0}_{rec}/\epsilon^{B^0_s}_{rec}$ from the 2018 MagUp simulation sample, with weights derived from data with various multiplicity and p_T selections.

4.5 Particle Identification Efficiencies

The PIDCalib package provides calibrated samples of identified particles that are used to determine the efficiencies for identifying the pions and muons. The specific PID requirements used in this analysis are `IsMuon` for muons and `ProbNNpi>0.9 && !IsMuon` for pions. The resulting PIDCalib efficiencies for muon and pion identification using these selections are shown in Fig 35 versus reconstructed momentum (left), rapidity (center), and number of long tracks (right), taken from the 2018 Mag Down data. For clarity, we note here that this nTracks variable is the number of reconstructed long tracks, and is not equivalent to the number of reconstructed VELO tracks that are used to characterize the events.
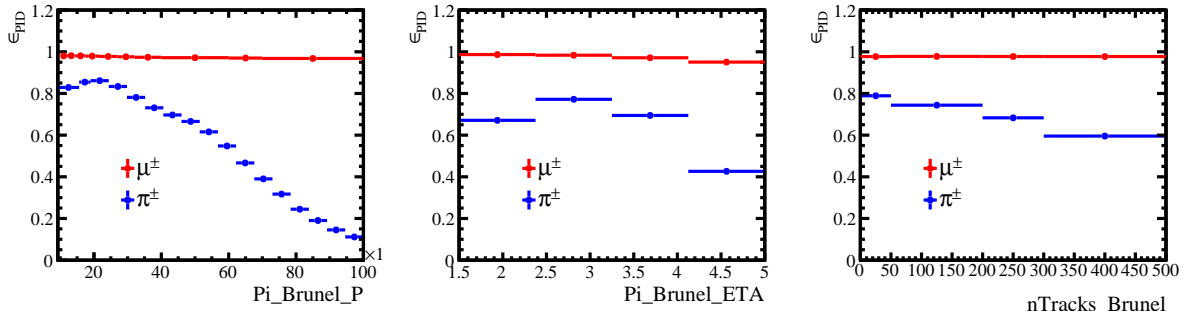
Figure 35: Particle identification efficiencies for muons and pions as a function of reconstructed momentum (left), rapidity (center), and number of long tracks (right).

Similar to the previously discussed trigger efficiencies, the PID efficiencies determined for the pions and muons must be folded with the spectra of daughters from the decays of interest. This done done by running over the simulated samples of decays and applying the efficiencies individually to each daughter product. Each run period has its own simulation set and PIDCalib tables, and each is considered separately. A representative set of the ratio of particle identification efficiencies for pions (left) and muons (right) from B^0 decays to B^0_s decays is shown in Fig. 36.

Again, weights are applied to the simulations in order to match the p_T, $nTracks$, and $m_{\pi^+\pi^-}$ distributions taken from the data. A systematic uncertainty is determined by randomly varying the extracted distributions within their uncertainties. The efficiencies
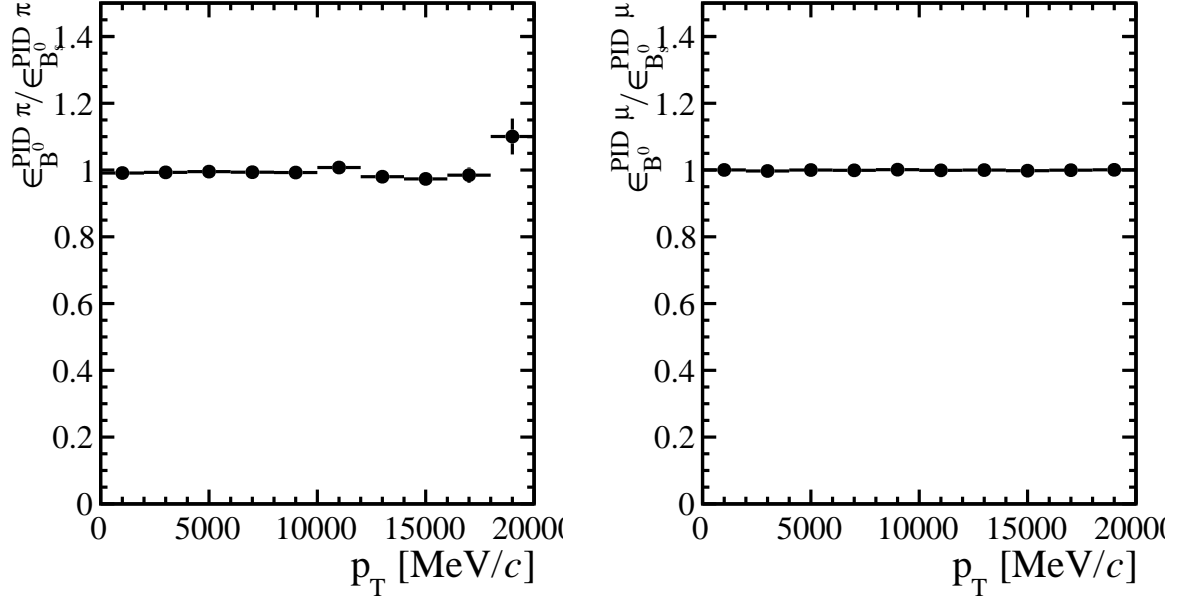
Figure 36: Ratio of particle identification efficiencies for pions (left) and muons (right) from B^0 decays to B_s^0 decays for the 2018 Mag Down run period.

Year	Magnet Configuration	$\epsilon_{\pi^\pm PID}^{B^0}/\epsilon_{\pi^\pm PID}^{B_s^0}$	$\epsilon_{\mu^\pm PID}^{B^0}/\epsilon_{\mu^\pm PID}^{B_s^0}$
2018	up	1.012±0.008	0.9997±0.0016
2018	down	1.003±0.004	1.000±0.0005
2017	up	1.012±0.004	0.9992±0.0016
2017	down	1.009±0.004	0.9999±0.0007
2016	up	1.000±0.005	1.0039±0.006
2016	down	1.001±0.007	1.0005±0.0015
Weighted average:		1.006±0.005	1.000±0.002

Table 18: The ratio of PID efficiencies $\epsilon_{PID}^{B^0}/\epsilon_{PID}^{B_s^0}$.

from PIDCalib are also varied randomly within their uncertainties. A set of 100 trials is run for each run period and magnet configuration, and the mean ± standard deviation of the set of 100 trials is taken as the central value ± uncertainty. Positive and negative charges are considered separately and averaged to give the value taken for each trial. The resulting efficiencies are given in Tab. 18 for each PIDCalib set. As previously, the efficiencies determined for each run period are combined via an average weighted by the luminosity sampled in each period to give the final efficiency. In all cases the uncertainties are less than 1%.

4.5.1 Multiplicity dependence

We see from the right panel of Fig. 35 that, while the muon ID efficiencies are constant with track multiplicity, there is some variation in the pion ID efficiency as multiplicity increases. This could potentially give a multiplicity-dependent ratio of PID efficiencies

29

nTracks	$\epsilon^{B^0}_{\pi^\pm PID}/\epsilon^{B^0_s}_{\pi^\pm PID}$	$\epsilon^{B^0}_{\mu^\pm PID}/\epsilon^{B^0_s}_{\mu^\pm PID}$
<50	1.008	1.002
50-100	1.010	0.9999
100-150	0.9934	1.0005
150-200	1.007	0.9996
200-300	1.009	0.9999
>300	1.010	0.9995
average	1.006	1.000

Table 19: Variation of PID efficiencies $\epsilon^{B^0}_{PID}/\epsilon^{B^0_s}_{PID}$ with multiplicity.

$p_{\rm T}$ range	$\epsilon^{B^0}_{\pi^\pm PID}/\epsilon^{B^0_s}_{\pi^\pm PID}$	$\epsilon^{B^0}_{\mu^\pm PID}/\epsilon^{B^0_s}_{\mu^\pm PID}$
$0 < p_{\rm T} <$20 GeV/c	1.01±0.01	1.00±0.01
$0 < p_{\rm T} <$6 GeV/c	1.01±0.01	1.00±0.01
$6 < p_{\rm T} <$12 GeV/c	1.01±0.01	1.00±0.01
$12 < p_{\rm T} <$20 GeV/c	1.02±0.01	1.00±0.01

Table 20: The ratio of PID efficiencies $\epsilon^{B^0}_{PID}/\epsilon^{B^0_s}_{PID}$ in the $p_{\rm T}$ bins used here.

that would need to be taken into account. This potential effect is studied by running the relative efficiency calculations over simulated data sets where the nTracks range is limited and varies from low to high multiplicity. The resulting calculations of relative PID efficiencies are collected in Tab. 19, where we see the standard deviation among the ratio of pion PID efficiencies is 0.6% and 0.1% for the ratio of muon ID efficiencies, and there is no significant deviation from the multiplicity-integrated results shown in 18.

To account for this potential variation, we take the weighted averages from Tab. 18 and round up all uncertainties to 1%, giving the ratio of PID efficiencies for B^0 to B^0_s decays shown in Tab. 20, all of which are consistent with one.

5 Results

The ratio of B^0_s to B^0 cross sections in the $J/\psi\pi^+\pi^-$ decay channel is given by

$$\frac{\mathcal{B}[B^0_s \to J/\psi\pi^+\pi^-]}{\mathcal{B}[B^0 \to J/\psi\pi^+\pi^-]} \times \frac{\sigma_{B^0_s}}{\sigma_{B^0}} = \frac{N_{B^0_s}}{N_{B^0}} \frac{\epsilon^{acc}_{B^0}\epsilon^{trig}_{B^0}\epsilon^{rec}_{B^0}(\epsilon^{\pi PID}_{B^0})^2(\epsilon^{\mu PID}_{B^0})^2}{\epsilon^{acc}_{B^0_s}\epsilon^{trig}_{B^0_s}\epsilon^{rec}_{B^0_s}(\epsilon^{\pi PID}_{B^0_s})^2(\epsilon^{\mu PID}_{B^0})^2} \tag{10}$$

where the relevant factors are:

- $N_{B^0_s}$ and N_{B^0} are the number of B^0_s and B^0 counts extracted by fitting the peaks in the $J/\psi\pi^+\pi^-$ mass spectra, as described in Sec. 3.1 and shown in Fig. 12. The N_{B^0} is corrected to remove the small contribution from K^0_s as discussed in Sec. 3.2, which contributes a systematic uncertainty ranging from 0.5% to 0.9% as shown in Tab. 9.

474 • $\frac{\epsilon_{B^0}^{acc}}{\epsilon_{B_s^0}^{acc}}$ is the ratio of the acceptance of the LHCb spectrometer for the daughter from

475 the B^0 and B_s^0 decays, as discussed in Sec. 4.2. This term is consistent with one

476 and contributes a systematic uncertainty of 1-2% as shown in Tab. 12.

477 • $\frac{\epsilon_{B^0}^{trig}}{\epsilon_{B_s^0}^{trig}}$ is the ratio of efficiencies for triggering on the B^0 and B_s^0 decays, as discussed in

478 Sec. 4.3. This term is consistent with one and contributes a systematic uncertainty

479 of 1% as shown in Tab. 14.

480 • $\frac{\epsilon_{B^0}^{rec}}{\epsilon_{B_s^0}^{rec}}$ is the ratio of reconstruction efficiencies for the B^0 and B_s^0 decays, as discussed

481 in Sec. 4.4. This term contributes a systematic uncertainty that ranges from 6% at

482 low p_{T} to 11% at high p_{T} as shown in Tab. 15.

483 • $\frac{\epsilon_{B^0}^{\pi PID}}{\epsilon_{B_s^0}^{\pi PID}}$ and $\frac{\epsilon_{B^0}^{\mu PID}}{\epsilon_{B_s^0}^{\mu PID}}$ are the ratio of pion and muon particle identification efficiencies,

484 discussed in Sec. 4.5. These terms are consistent with one and contribute a

485 systematic uncertainty of 1% as shown in Tab. 20.

486 • For comparison with other decay channels, it is necessary to correct these measure-

487 ments by the B_s^0 and B^0 branching fractions to $\pi^+\pi^-$, which are $\mathcal{B}[B^0 \to J/\psi\pi^+\pi^-]$

488 $= (4.00\pm0.15)\times10^{-5}$ from the PDG and $\mathcal{B}[B_s^0 \to J/\psi\pi^+\pi^-] = (2.01\pm0.12)\times10^{-4}$

489 from LHCb-PAPER-2020-046. The resulting ratio of branching fractions is thereby

490 $\mathcal{B}_{B^0}/\mathcal{B}_{B_s^0} = 0.199\pm0.014$, where the uncertainty on the branching fractions is taken

491 as systematic uncertainty of 7% on the corrected ratio of B_s^0 to B^0 cross sections.

492 First we consider the multiplicity integrated ratio of B_s^0 to B^0 cross sections. A fit

493 to the multiplicity-integrated $J/\psi\pi^+\pi^-$ invariant mass spectrum (using the techniques

494 described in Sec. 3.1) gives a ratio of counts $N_{B_s^0}/N_{B^0} = 1.649 \pm 0.055$. Following Eq.

495 10, and applying the relevant efficiency ratios and branching fractions, we find

496 we find a value of

$$\frac{\sigma_{B_s^0}}{\sigma_{B^0}} = 0.30 \pm 0.01 \pm 0.026 \tag{11}$$

497 for the multiplicity-integrated ratio, where the uncertainties are statistical and system-

498 atic, respectively (the uncertainty on the branching fractions is included in the systematic

499 uncertainty quoted here).

500 For comparison, LHCb-PAPER-2020-046 reports a value of

$$f_s/f_d = 0.2539 \pm 0.0079 \tag{12}$$

501 in pp collisions at 13 TeV, over the interval 0.5< p_{T} <40 GeV/c and 2< η <6.4,

502 which is similar (although not identical) to the range 0< p_{T} <20 GeV/c and 2< η <4.5

503 used in the measurements here. Adding the systematic and statistical uncertainties in

504 quadrature and comparing, we see that the measurement presented here and the previous

505 measurement of f_s/f_d are in good agreement at the $\sim1.5\sigma$ level.

506 The multiplicity dependence of the ratio of cross sections is shown in Fig. 37, where

507 the error bars represent statistical uncertainties from the fit, which are uncorrelated

508 point-to-point, and the error boxes represent systematic uncertainties from the various

509 efficiency corrections, which are correlated point-to-point. The horizontal error bars

31

represent the bin width and all points are plotted at the bin center. The horizontal axis N_{tracks}^{VELO} scale has been normalized by the average number of VELO tracks in an event (taken from Fig. 6).
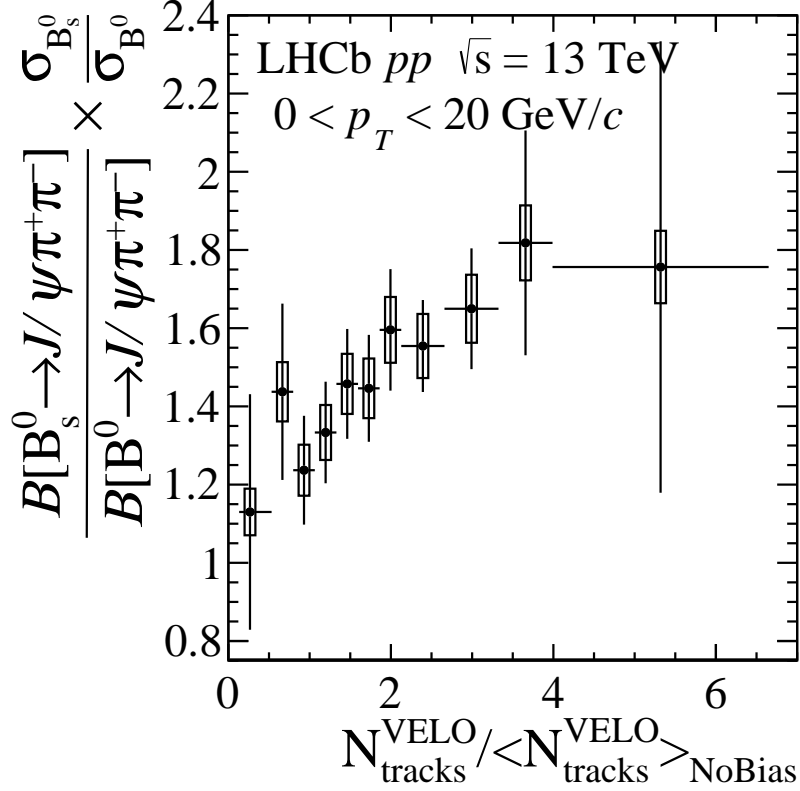
Figure 37: The ratio of B_s^0 to B^0 cross sections in the $J/\psi\pi^+\pi^-$ channel versus multiplicity in the range $0 < p_{\mathrm{T}} < 20$ GeV/c.

To estimate the significance of the rising trend, a linear function $y = mx + b$ is fit to the data, considering only the point-to-point uncorrelated uncertainties, as the correlated systematic uncertainties do not affect the slope. The slope of this line deviates from 0 (which represents the null hypothesis) by 2.7σ.

The same analysis is also performed in three transverse momentum bins: $0 < p_{\mathrm{T}} < 6$ GeV/c, $6 < p_{\mathrm{T}} < 12$ GeV/c, and $12 < p_{\mathrm{T}} < 20$ GeV/c, and the results are shown in Figs. 38, 39, and 40, respectively. We see that the enhancement is concentrated in the lowest p_{T} range, as expected in a scenario where B hadrons form via coalescence with other quarks that constitute the low p_{T} bulk of the underlying event. Following the same procedure as above for estimating the significance and fitting the data with a line, we see that the 0 to 6 GeV/c has a positive slope with a significance of 3.1σ, while the 6 to 12 and 12 to 20 GeV/c data are consistent with no slope at the 0.2σ and 1.3σ levels, respectively.

Another way to present this data is to divide out the branching fractions and compare with the f_s/f_d ratio measured at e^+e^- colliders. The HFLAV group reports a value of $f_s/f_d = 0.262+0.052-0.043$ from e^+e^- collisions at the $\Upsilon(5S)$ resonance, and $f_s/f_d = 0.249\pm0.023$ at the Z^0, which is included in Figs. 41 through 44. In these plots, the correlated systematic uncertainty boxes include an additional 7% (added in quadrature) due to the uncertainty in the B_s^0 and B^0 branching fractions to $J/\psi\pi^+\pi^-$.
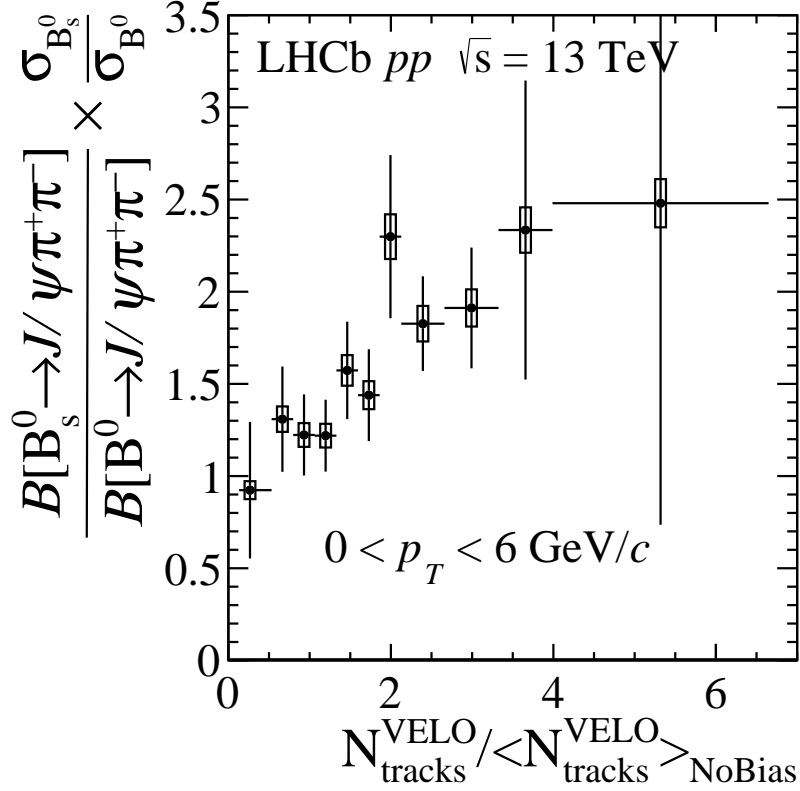
Figure 38: The ratio of B_s^0 to B^0 cross sections versus multiplicity in the range $0< p_{\mathrm{T}} <6$ GeV/c, as measured in the $J/\psi\pi^+\pi^-$ decay channel.

It is interesting to note that the cross section ratio in the low multiplicity region of the p_{T}-integrated data in Fig. 41 and the low p_{T} data in Fig. 42 are consistent with the f_s/f_d value from e^+e^- collisions, and increases at high multiplicity. The higher p_{T} data shows no significant variation with multiplicity and is consistent across the full range measured with the e^+e^- data.

This data set can also be examined as a function of the activity in the backwards direction, using the number of backwards VELO tracks to characterize the event, rather than the sum of all tracks (the backwards tracks are a subset of the total number of VELO tracks). This gives an interval of ~ 4 units of rapidity (or more) between the measured B mesons and the tracks used to characterize the event. The resulting dependence of the B_s^0/B^0 cross section ratio is shown in Figs. 45 where the horizontal axis scale has been normalized by the average number of back tracks in an event (taken from Fig. 6). There is no significant dependence on the backwards track multiplicity; the linear fit gives a slope with a significance of 1.1σ. This indicates that the enhancement effect is correlated with the local particle multiplicity in a similar rapidity region as the b hadron, which is expected in a scenario where B hadrons form via coalescence with other quarks in the event when their wave functions overlap at chemical freezeout.

33
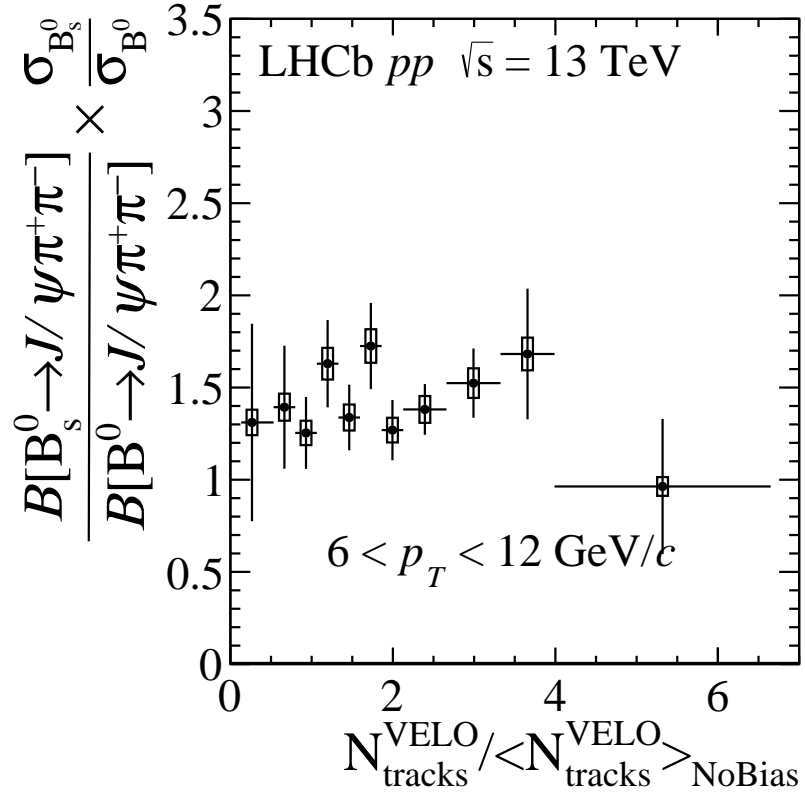
Figure 39: The ratio of B_s^0 to B^0 cross sections versus multiplicity in the range 6< p_{T} <12 GeV/c, as measured in the $J/\psi\pi^+\pi^-$ decay channel.
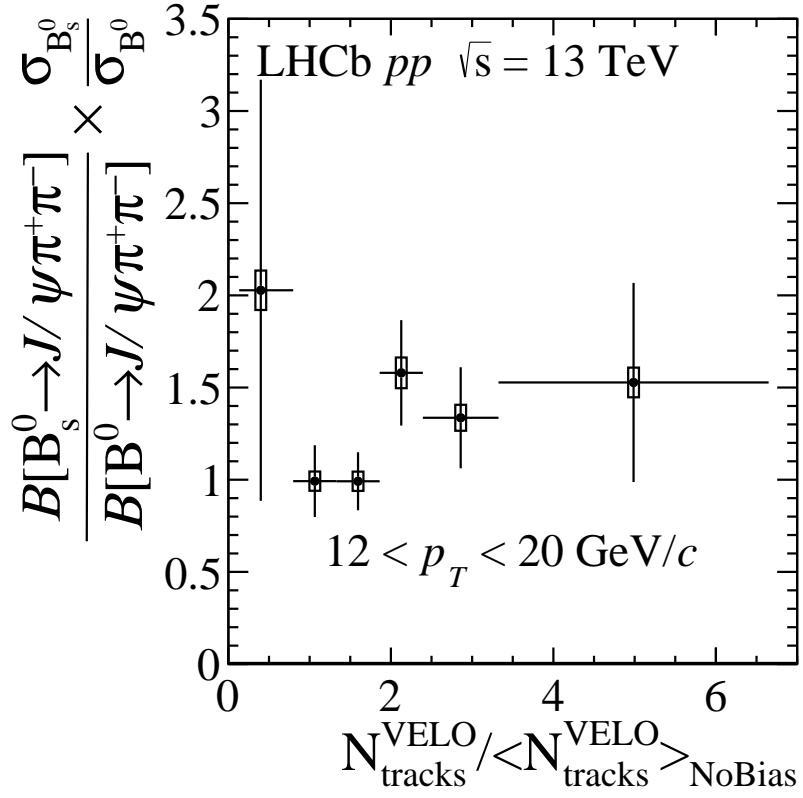
Figure 40: The ratio of B_s^0 to B^0 cross sections versus multiplicity in the range $12 < p_{\text{T}} < 20$ GeV/c, as measured in the $J/\psi\pi^+\pi^-$ decay channel.
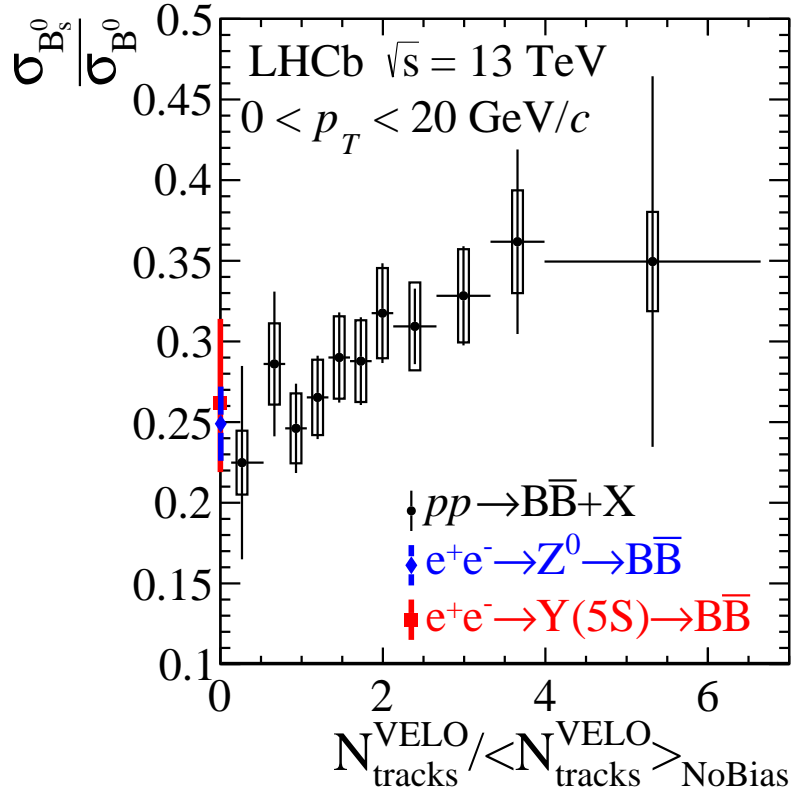
Figure 41: The ratio of B_s^0 to B^0 cross sections versus multiplicity in the range $0 < p_{\mathrm{T}} < 20$ GeV/c, compared with the f_s/f_d ratio from $\Upsilon(5S)$ and Z^0 decays.
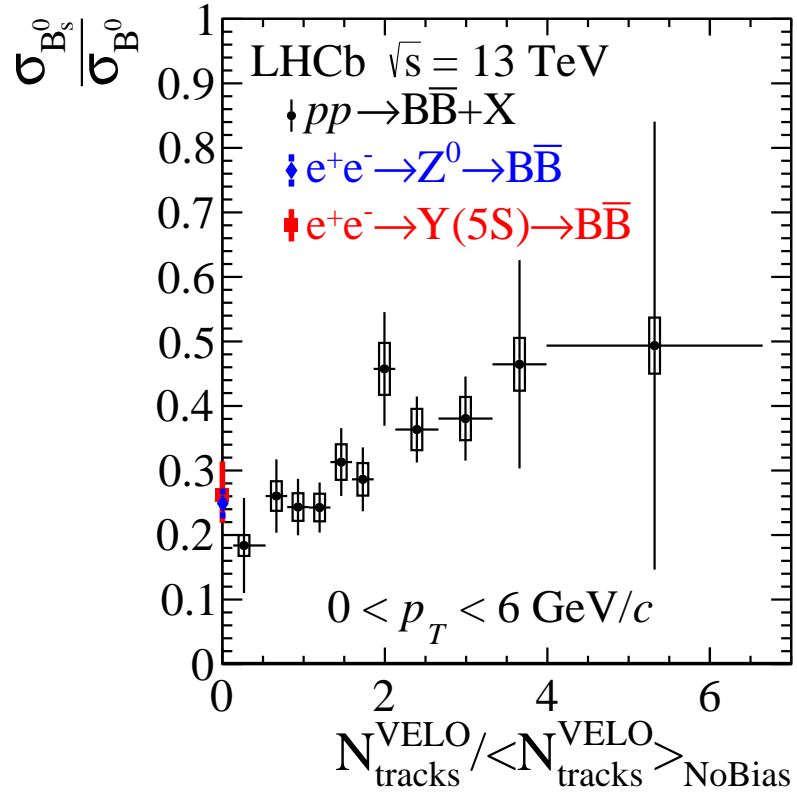
Figure 42: The ratio of B_s^0 to B^0 cross sections versus multiplicity in the range $0 < p_T < 6$ GeV/c, compared with the f_s/f_d ratio from $\Upsilon(5S)$ and Z^0 decays.
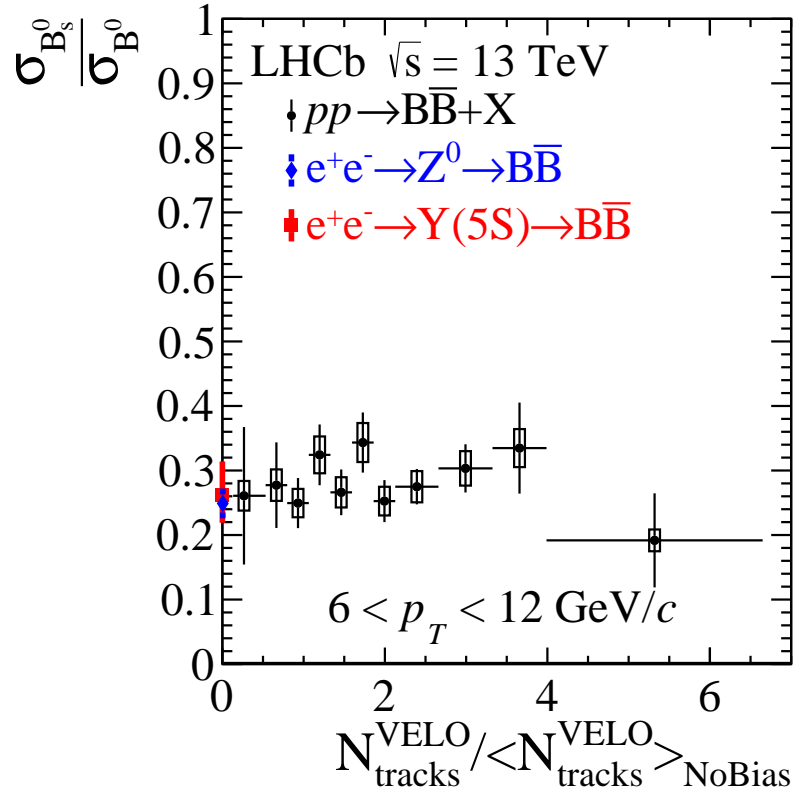
Figure 43: The ratio of B_s^0 to B^0 cross sections versus multiplicity in the range $6 < p_{\mathrm{T}} < 12$ GeV/c, compared with the f_s/f_d ratio from $\Upsilon(5S)$ and Z^0 decays.
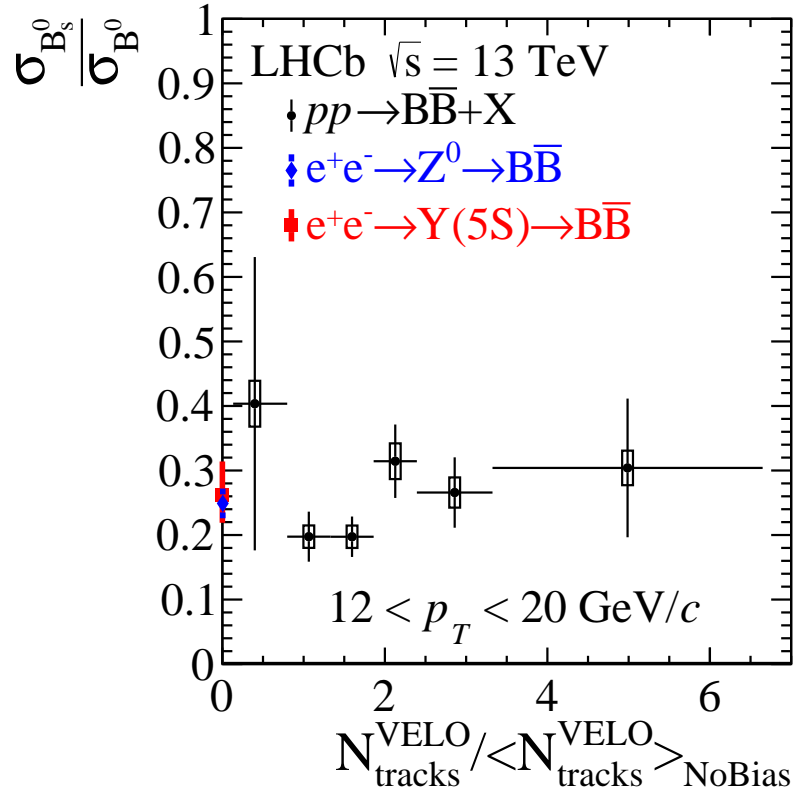
Figure 44: The ratio of B_s^0 to B^0 cross sections versus multiplicity in the range $12 < p_{\mathrm{T}} < 20$ GeV/c, compared with the f_s/f_d ratio from $\Upsilon(5S)$ and Z^0 decays.
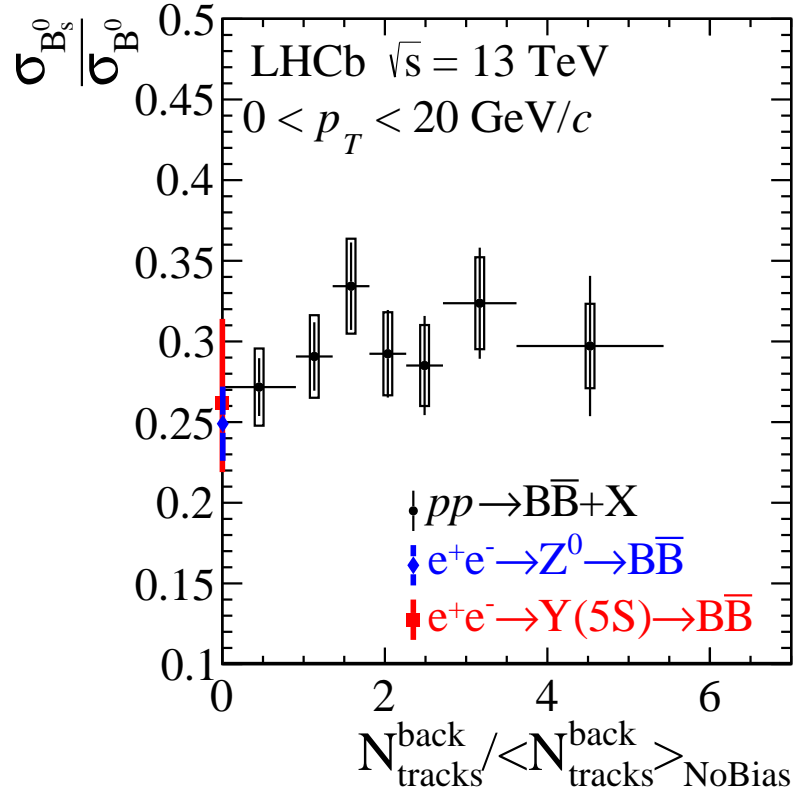
Figure 45: The ratio of B_s^0 to B^0 cross sections versus multiplicity measured in the backwards direction.

Appendices

A B_s^0/B^0 fits for $0 < p_{\mathrm{T}} < 20$ GeV/c
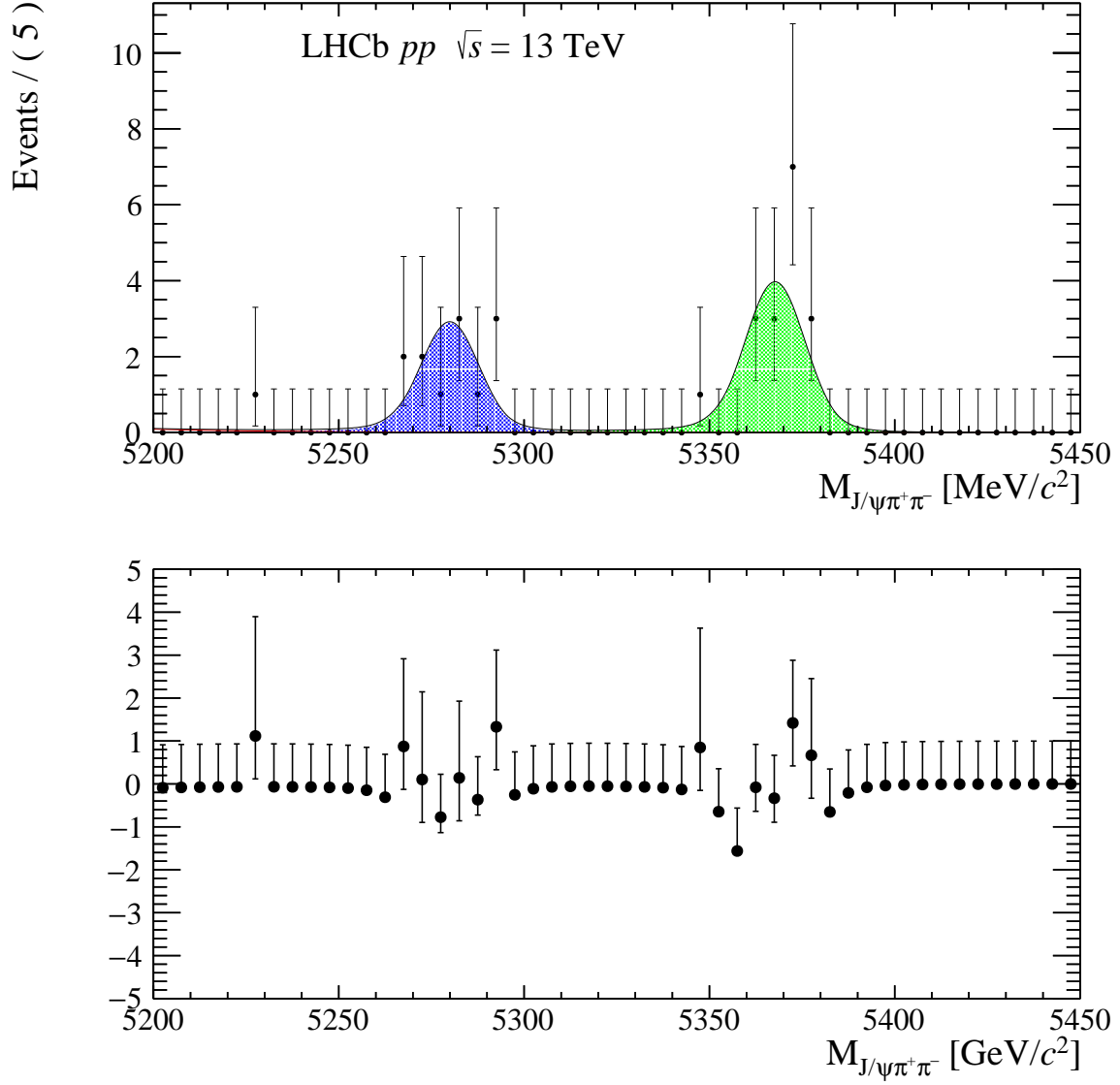
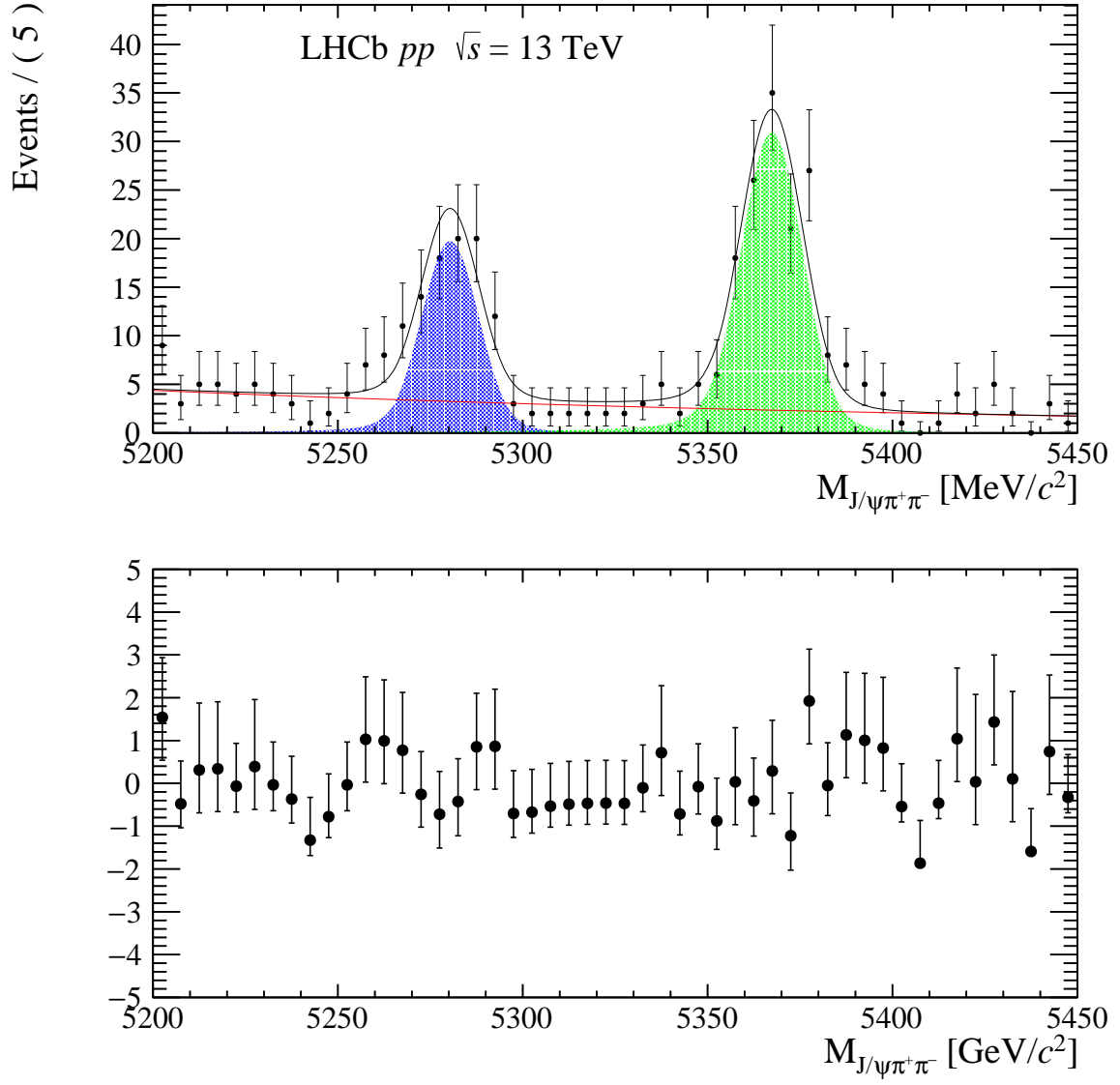Figure 46: Fit to the $J/\psi\pi^+\pi^-$ mass spectrum in the multiplicity range $5 \leq N_{tracks}^{VELO} \leq 20$.
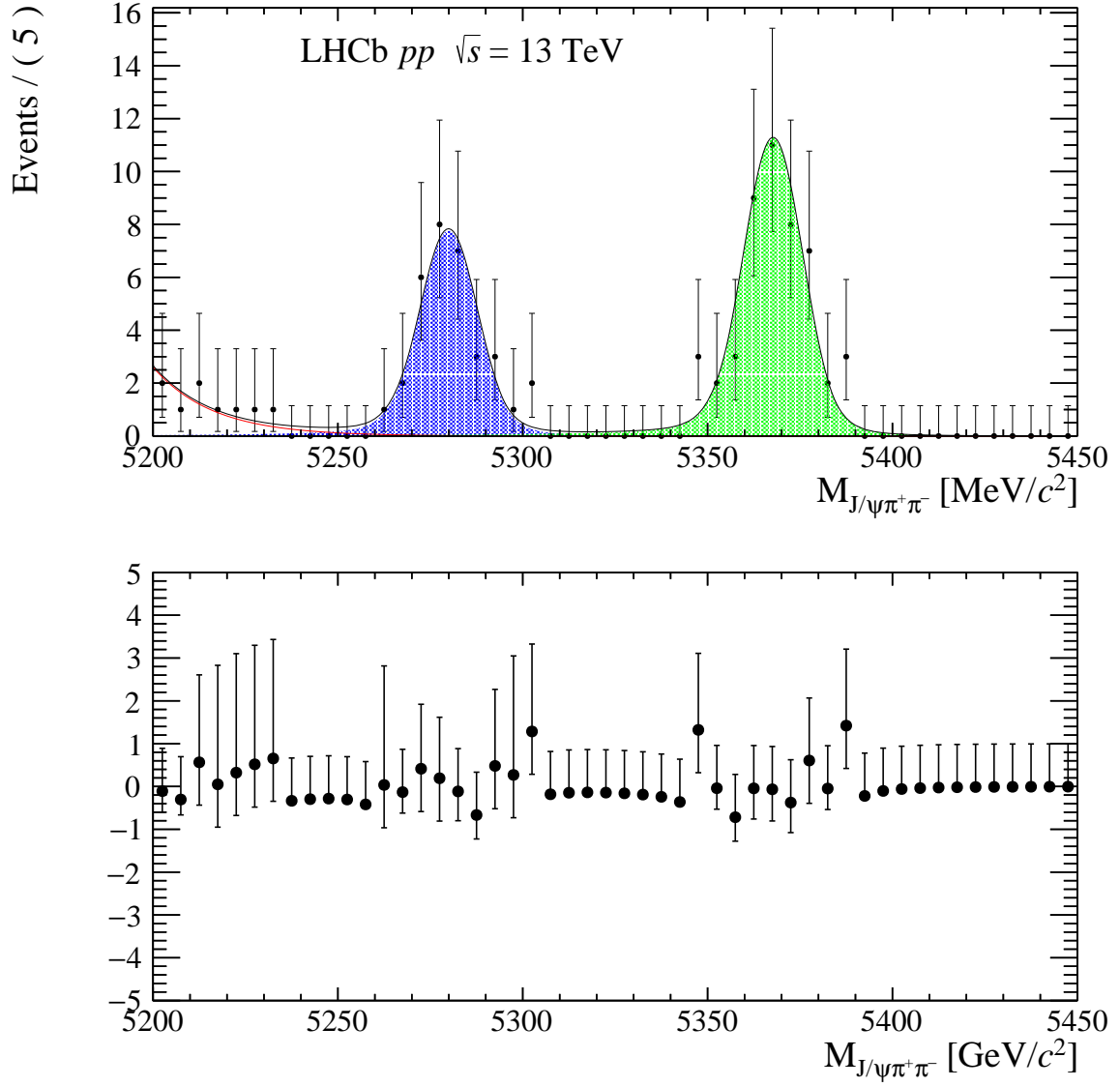
Figure 47: Fit to the $J/\psi\pi^+\pi^-$ mass spectrum in the multiplicity range $21 \leq N_{tracks}^{VELO} \leq 30$.
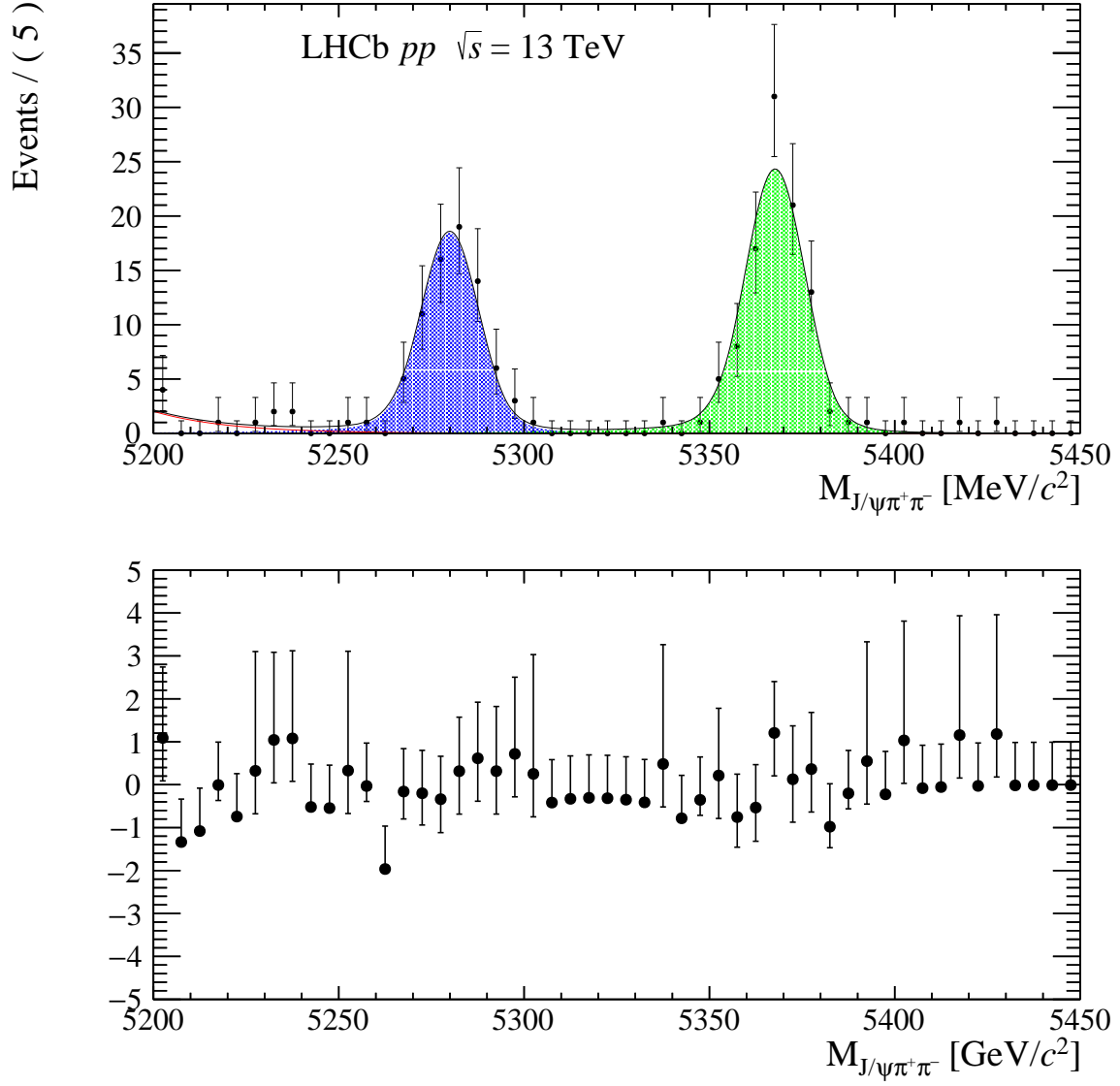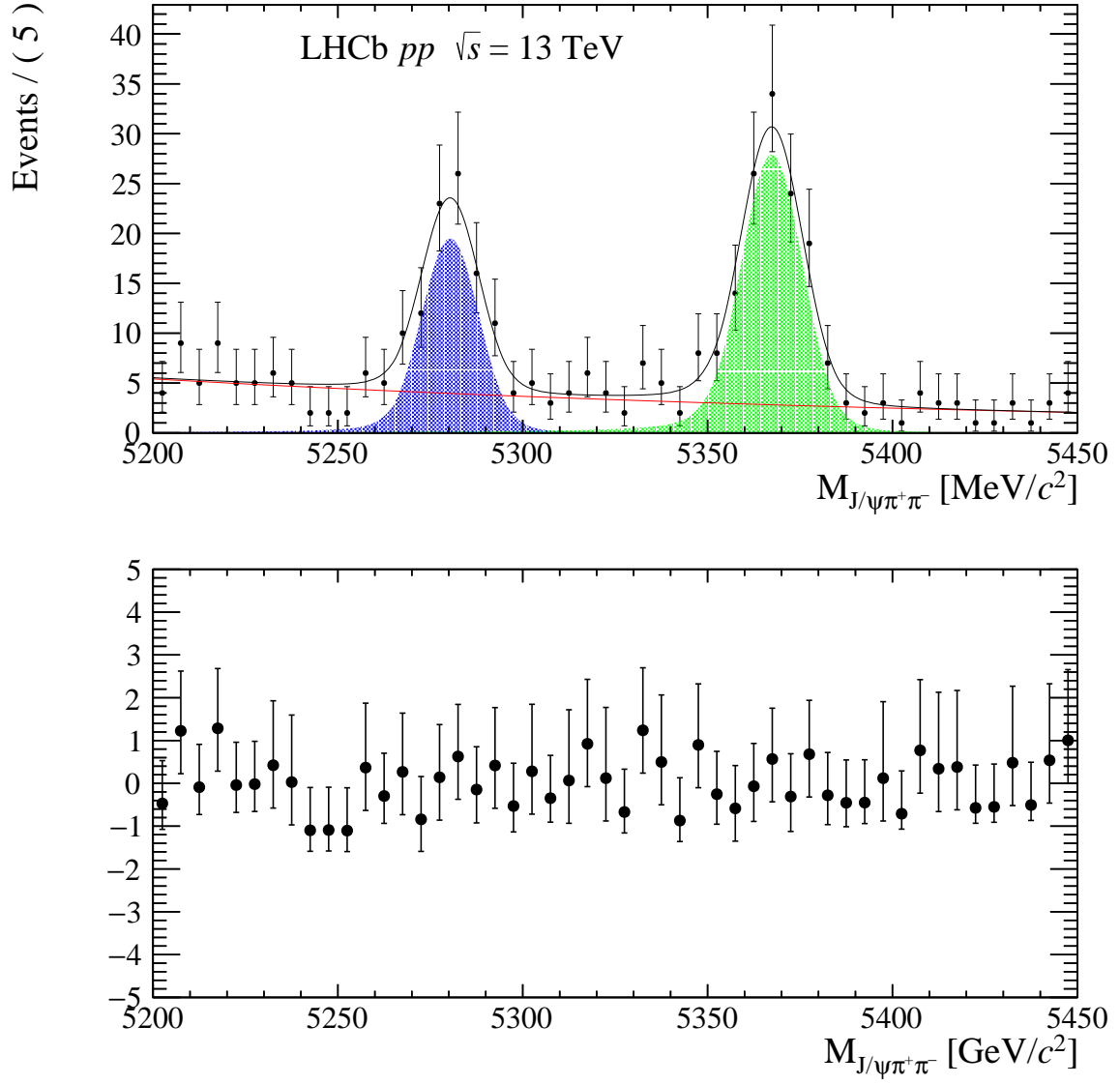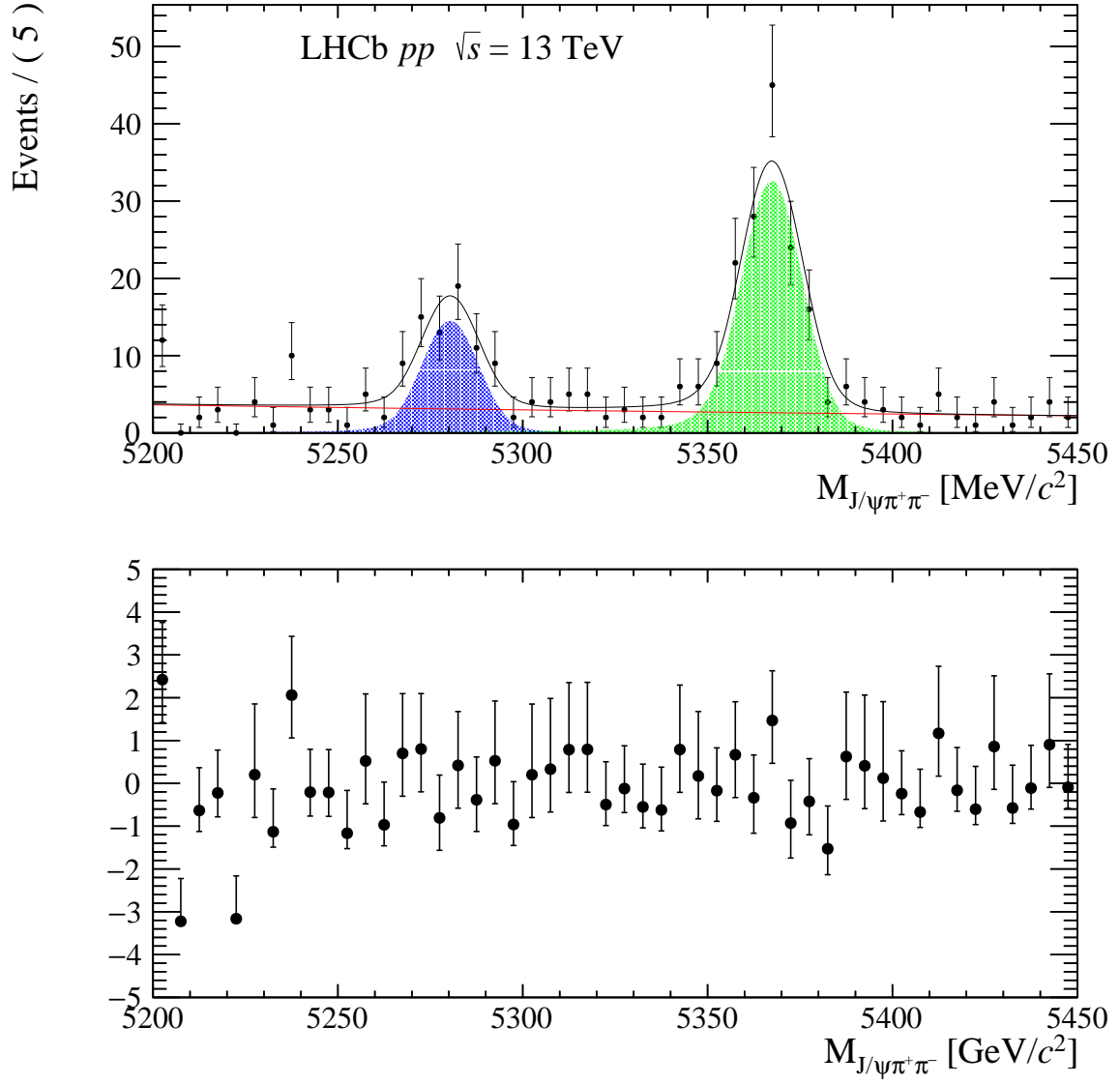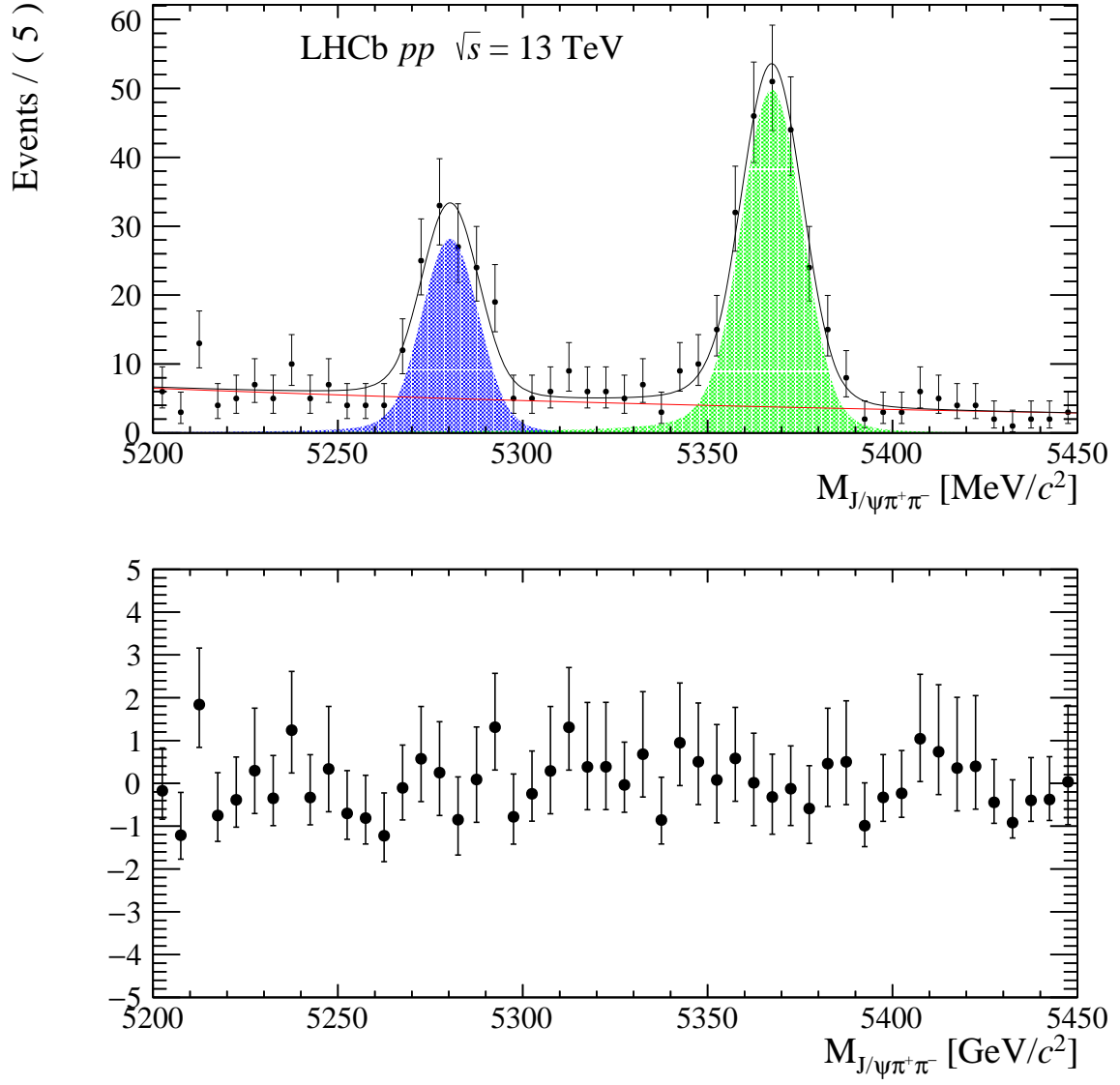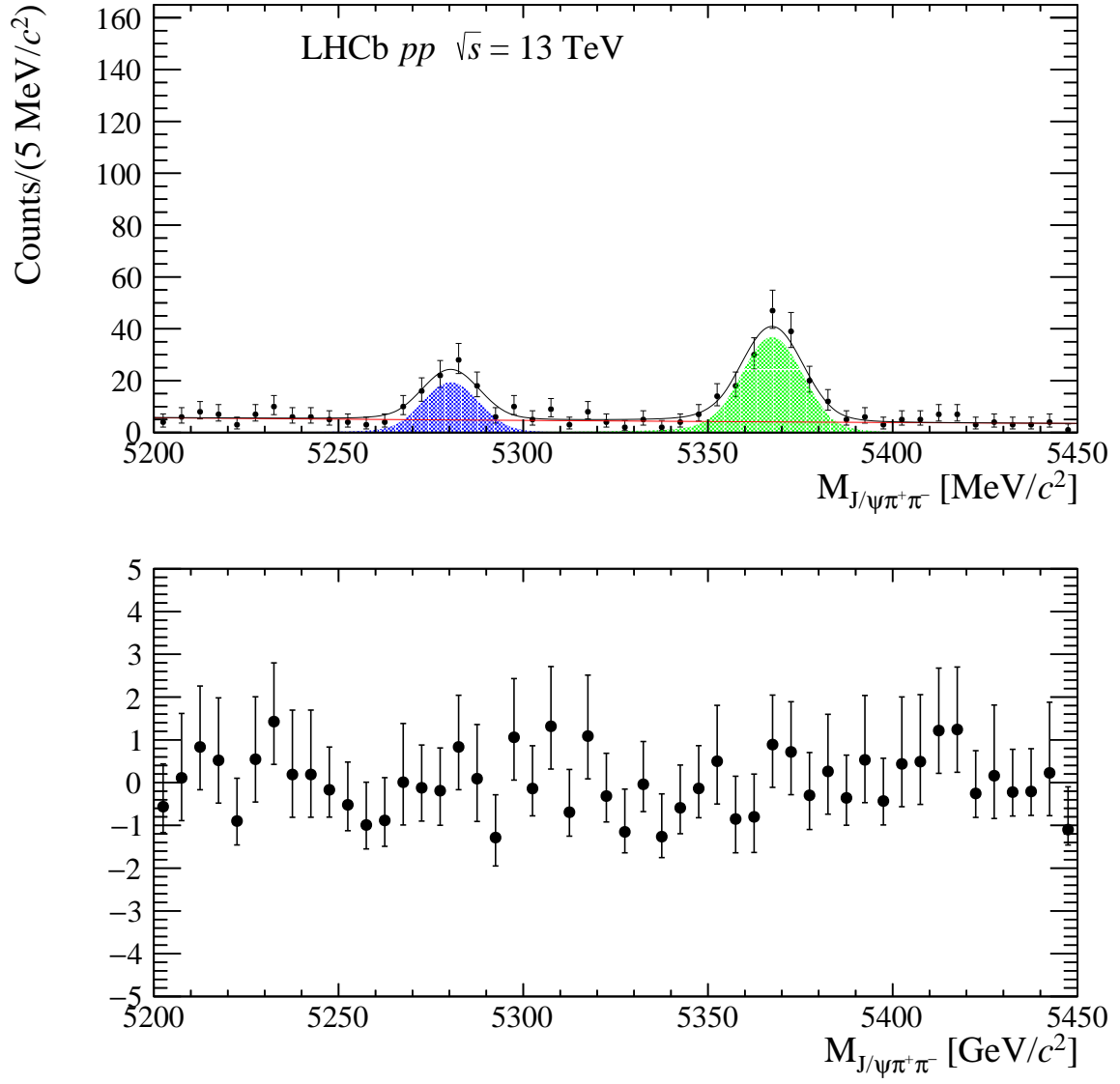
Figure 48: Fit to the $J/\psi\pi^+\pi^-$ mass spectrum in the multiplicity range $31 \leq N_{tracks}^{VELO} \leq 40$.

B $\quad B_s^0/B^0$ fits for $0 < p_T < 6$ GeV/c

C $\quad B_s^0/B^0$ fits for $6 < p_T < 12$ GeV/c

D $\quad B_s^0/B^0$ fits for $12 < p_T < 20$ GeV/c

E $\quad B_s^0/B^0$ fits for $0 < p_T < 20$ GeV/c as a function of backwards track multiplicity

References

[1] P. Koch, B. Muller, and J. Rafelski, *Strangeness in Relativistic Heavy Ion Collisions*, Phys. Rept. **142** (1986) 167.
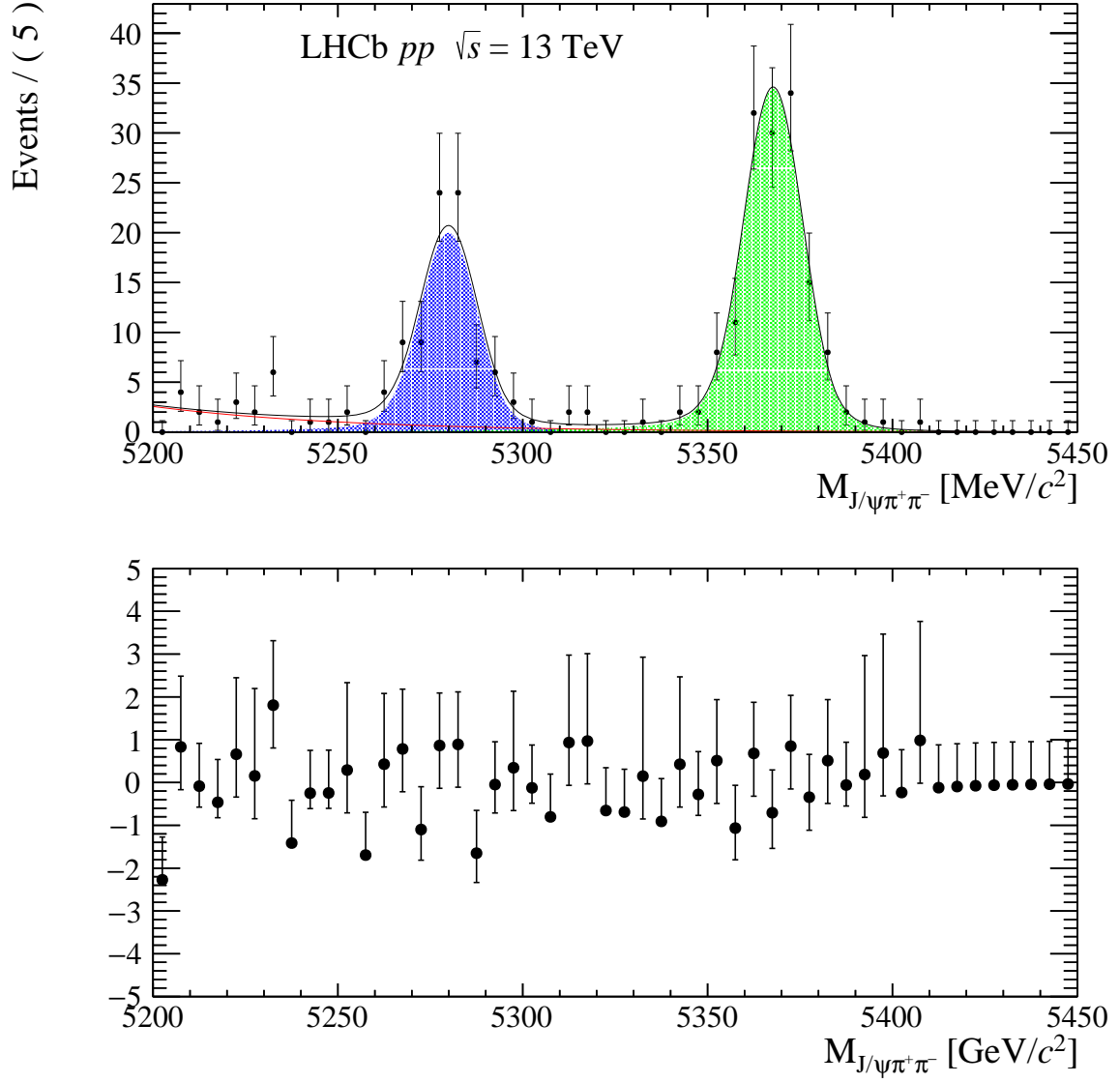
Figure 49: Fit to the $J/\psi\pi^+\pi^-$ mass spectrum in the multiplicity range $41 \leq N_{tracks}^{VELO} \leq 50$.

[2] ALICE, J. Adam *et al.*, *Enhanced production of multi-strange hadrons in high-multiplicity proton-proton collisions*, Nature Phys. **13** (2017) 535, arXiv:1606.07424.

[3] R. Aaij *et al.*, *Performance of the LHCb Vertex Locator*, JINST **9** (2014) P09007, arXiv:1405.7808.

[4] BaBar, B. Aubert *et al.*, *A measurement of the $B^0 \to J/\psi\pi^+\pi^-$ branching fraction*, Phys. Rev. Lett. **90** (2003) 091801, arXiv:hep-ex/0209013.

[5] LHCb collaboration, R. Aaij *et al.*, *Analysis of the resonant components in $\overline{B}^0 \to J/\psi\pi^+\pi^-$*, Phys. Rev. **D87** (2013) 052001, arXiv:1301.5347.

[6] M. Kucharczyk, P. Morawski, and M. Witek, *Primary Vertex Reconstruction at LHCb*, LHCb-PUB-2014-044. CERN-LHCb-PUB-2014-044, CERN, Geneva, 2014.
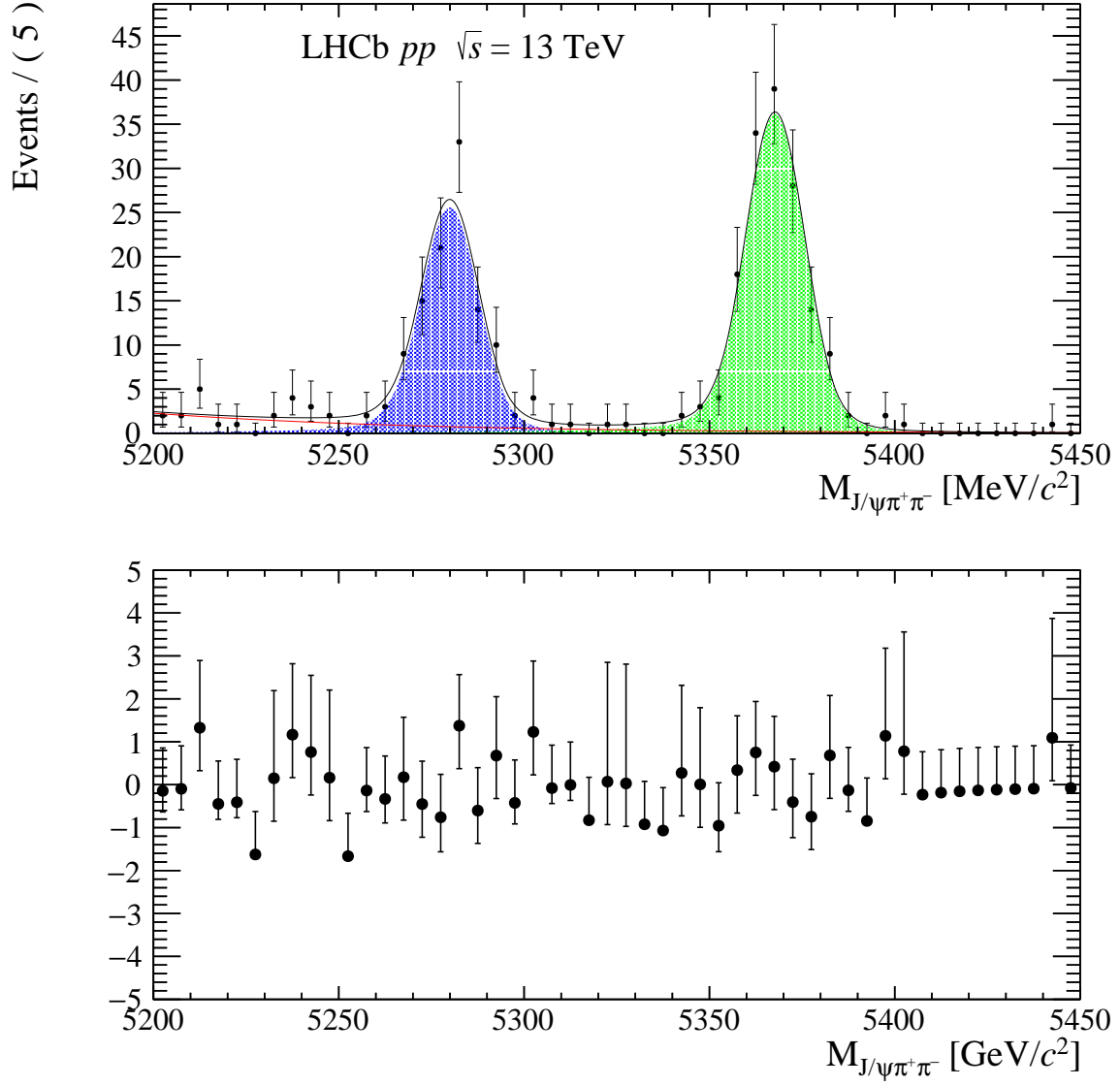
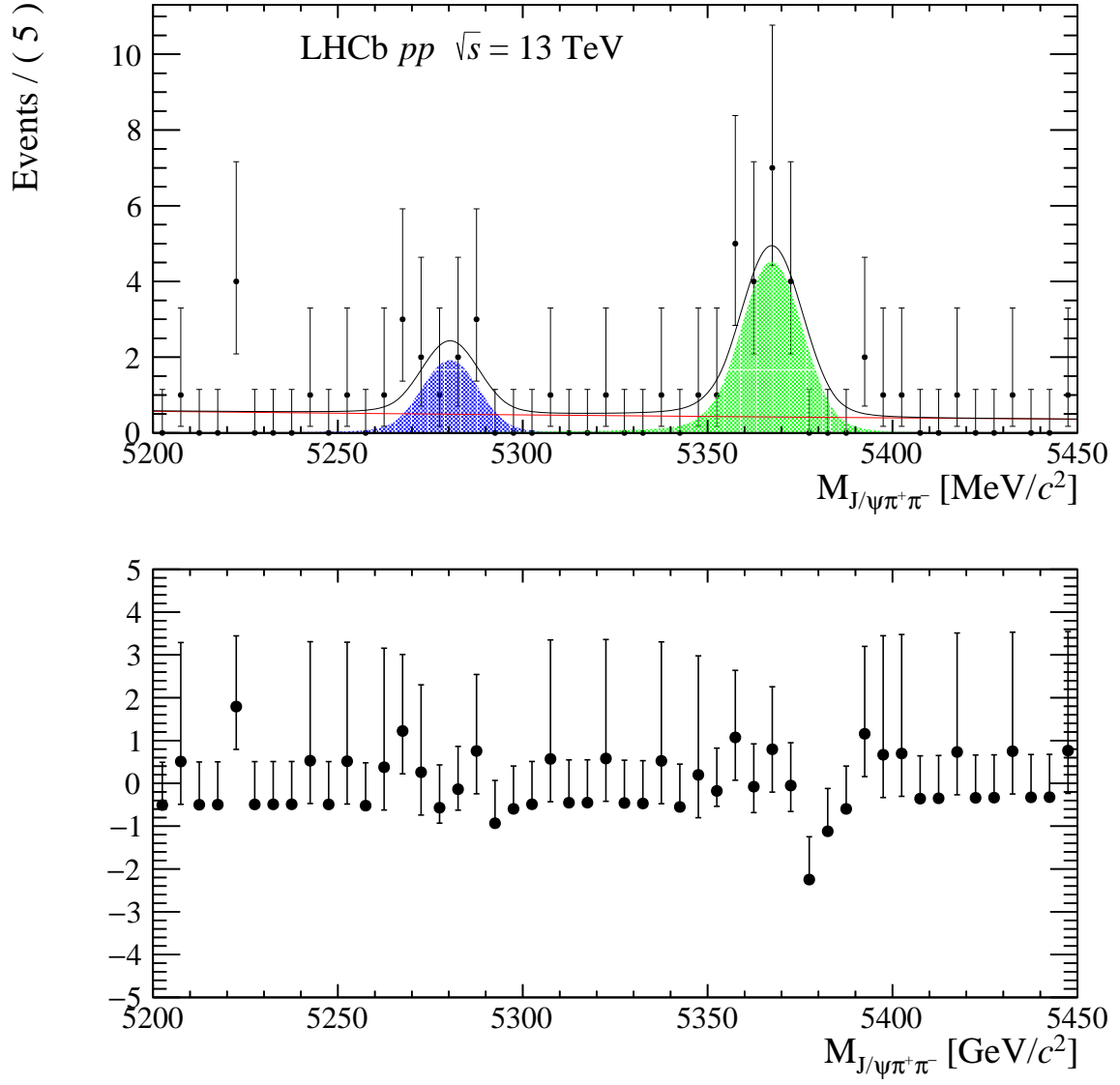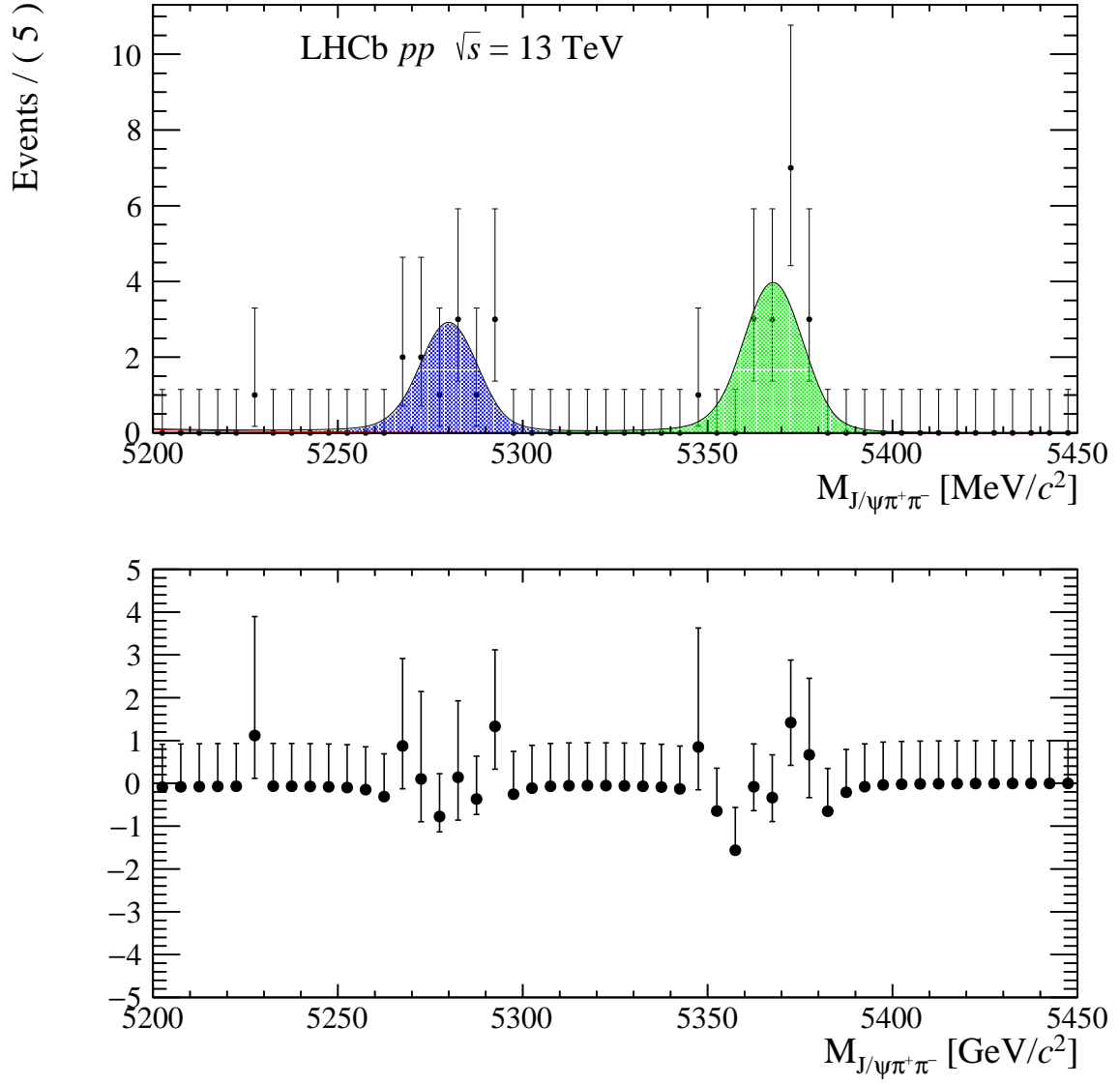Figure 50: Fit to the $J/\psi\pi^+\pi^-$ mass spectrum in the multiplicity range $51 \leq N_{tracks}^{VELO} \leq 60$.

[7] M. Pivk and F. R. Le Diberder, *SPlot: A Statistical tool to unfold data distributions*, Nucl. Instrum. Meth. **A555** (2005) 356, arXiv:physics/0402083.

[8] LHCb collaboration, R. Aaij *et al.*, *Measurement of B meson production cross-sections in proton-proton collisions at $\sqrt{s} = 7$ TeV*, JHEP **08** (2013) 117, arXiv:1306.3663.

[9] LHCb collaboration, R. Aaij *et al.*, *Measurement of the $B^\pm$ production cross-section in pp collisions at $\sqrt{s} = 7$ and 13 TeV*, JHEP **12** (2017) 026, arXiv:1710.04921.

[10] LHCb collaboration, R. Aaij *et al.*, *Precise measurement of the f_s/f_d ratio of hadronisation fractions and of B_s^0 decay branching fractions*, arXiv:2103.06810, Submitted to PRD.
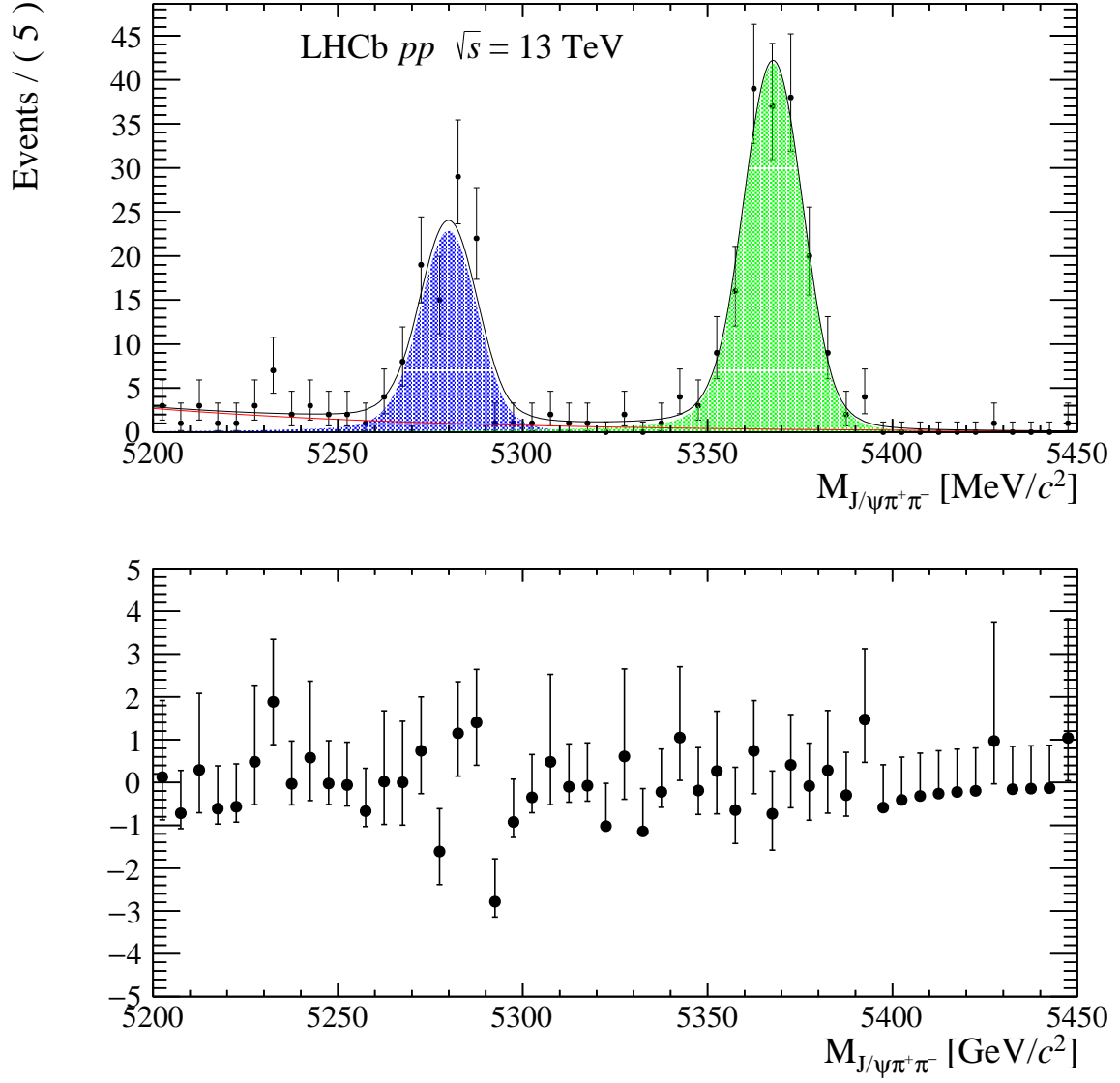
Figure 51: Fit to the $J/\psi\pi^+\pi^-$ mass spectrum in the multiplicity range $61 \leq N_{tracks}^{VELO} \leq 70$.

[11] S. Tolk, J. Albrecht, F. Dettori, and A. Pellegrino, *Data driven trigger efficiency determination at LHCb*, LHCb-PUB-2014-039. CERN-LHCb-PUB-2014-039, CERN, Geneva, 2014.
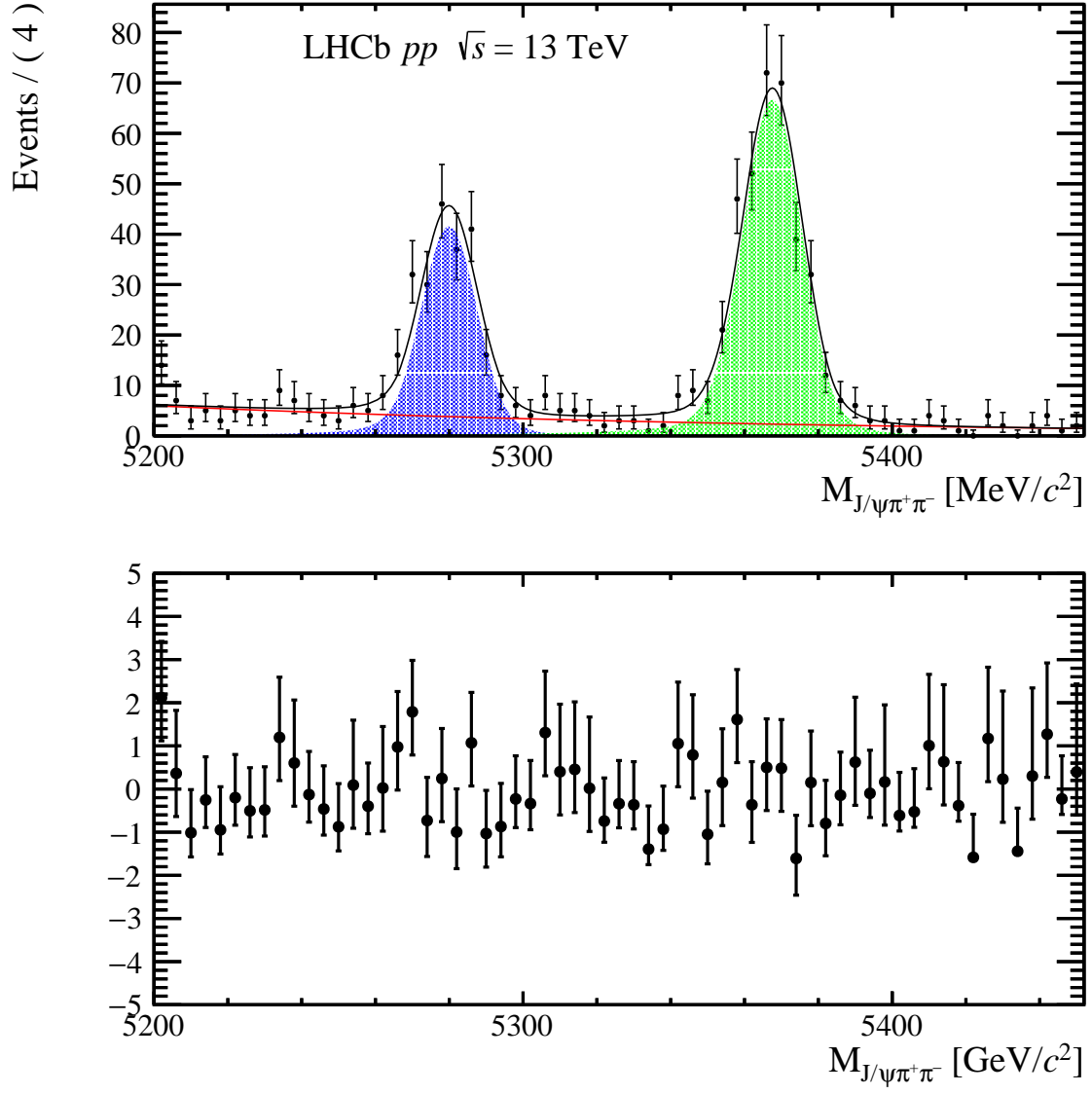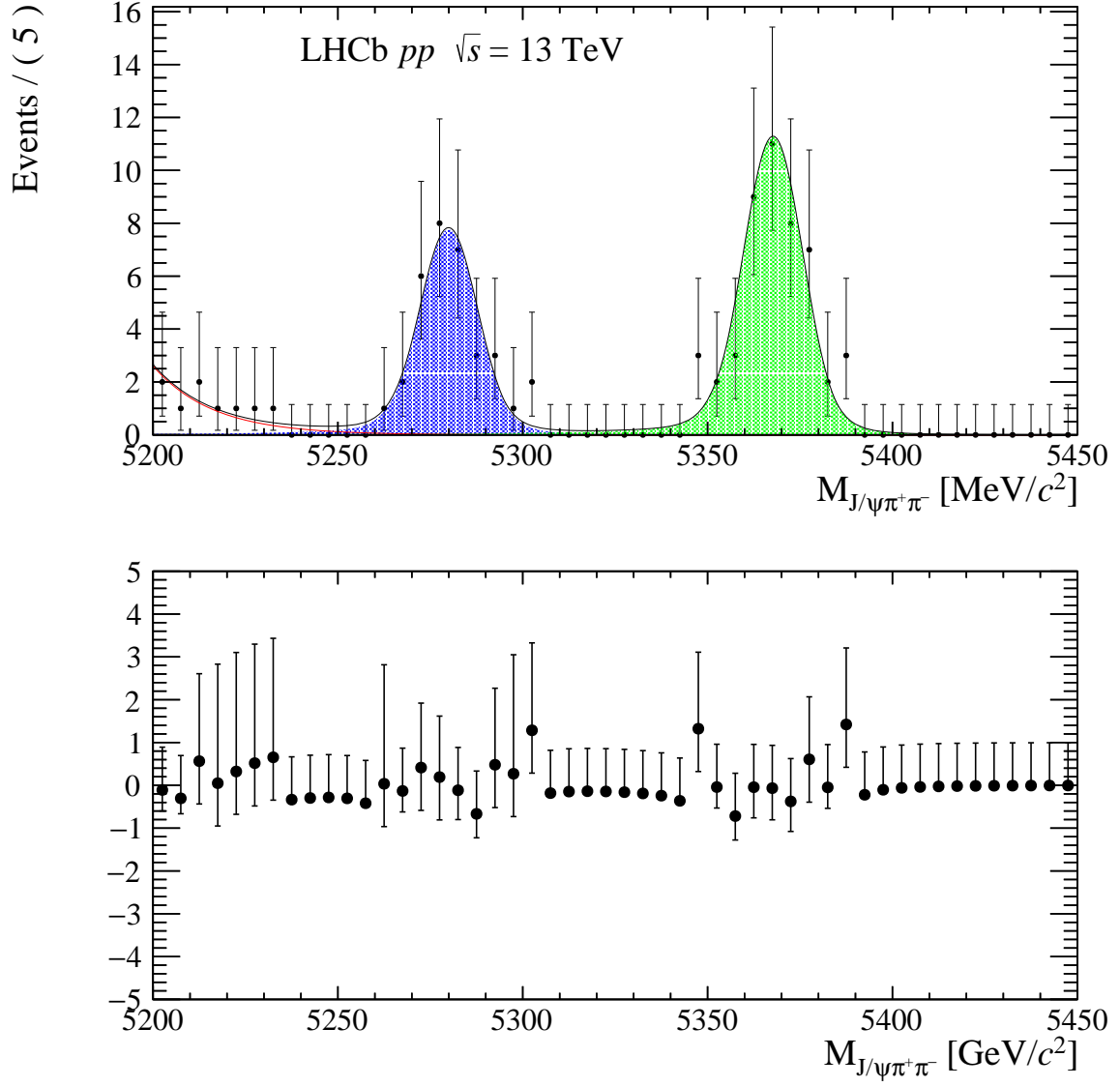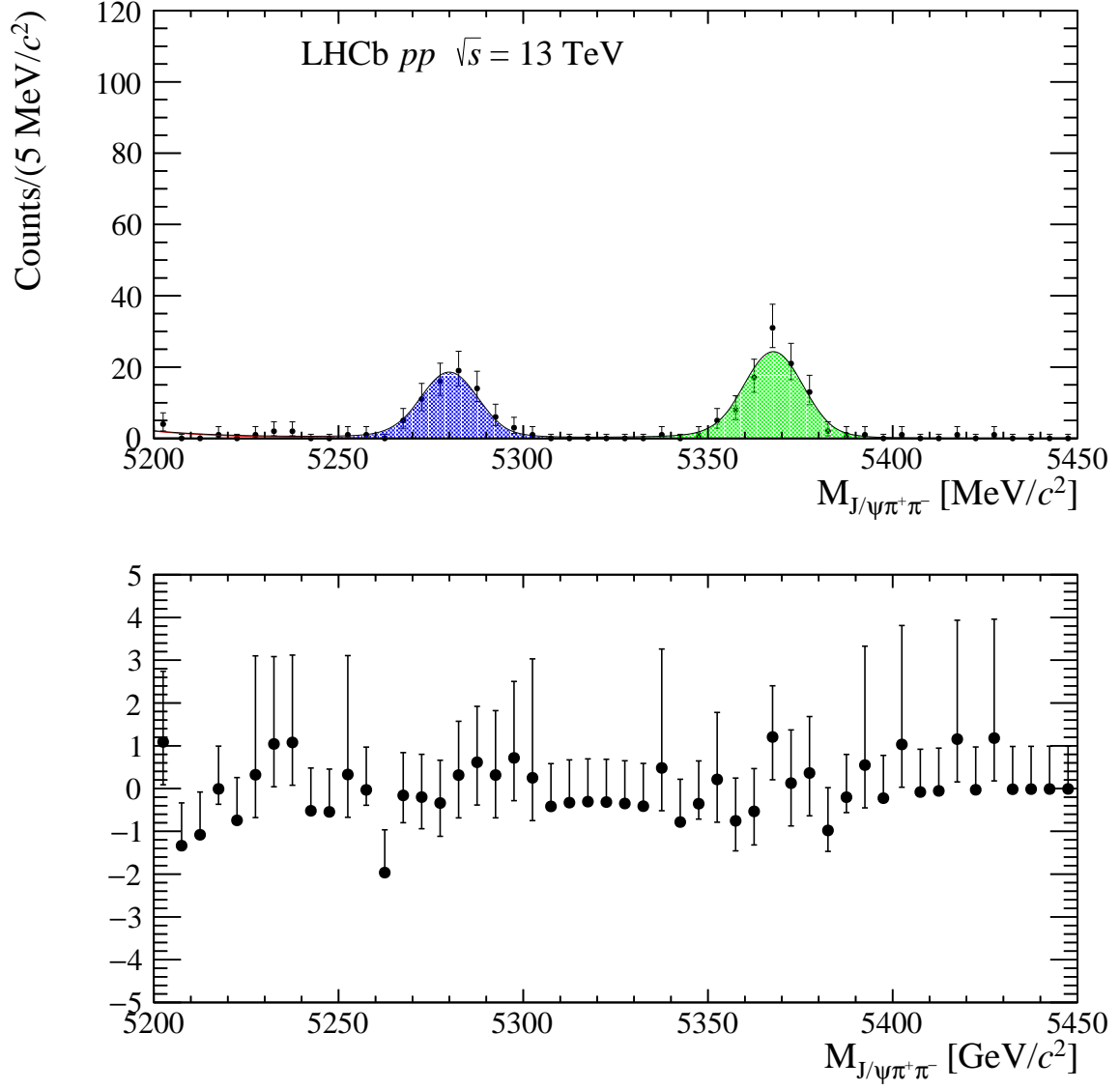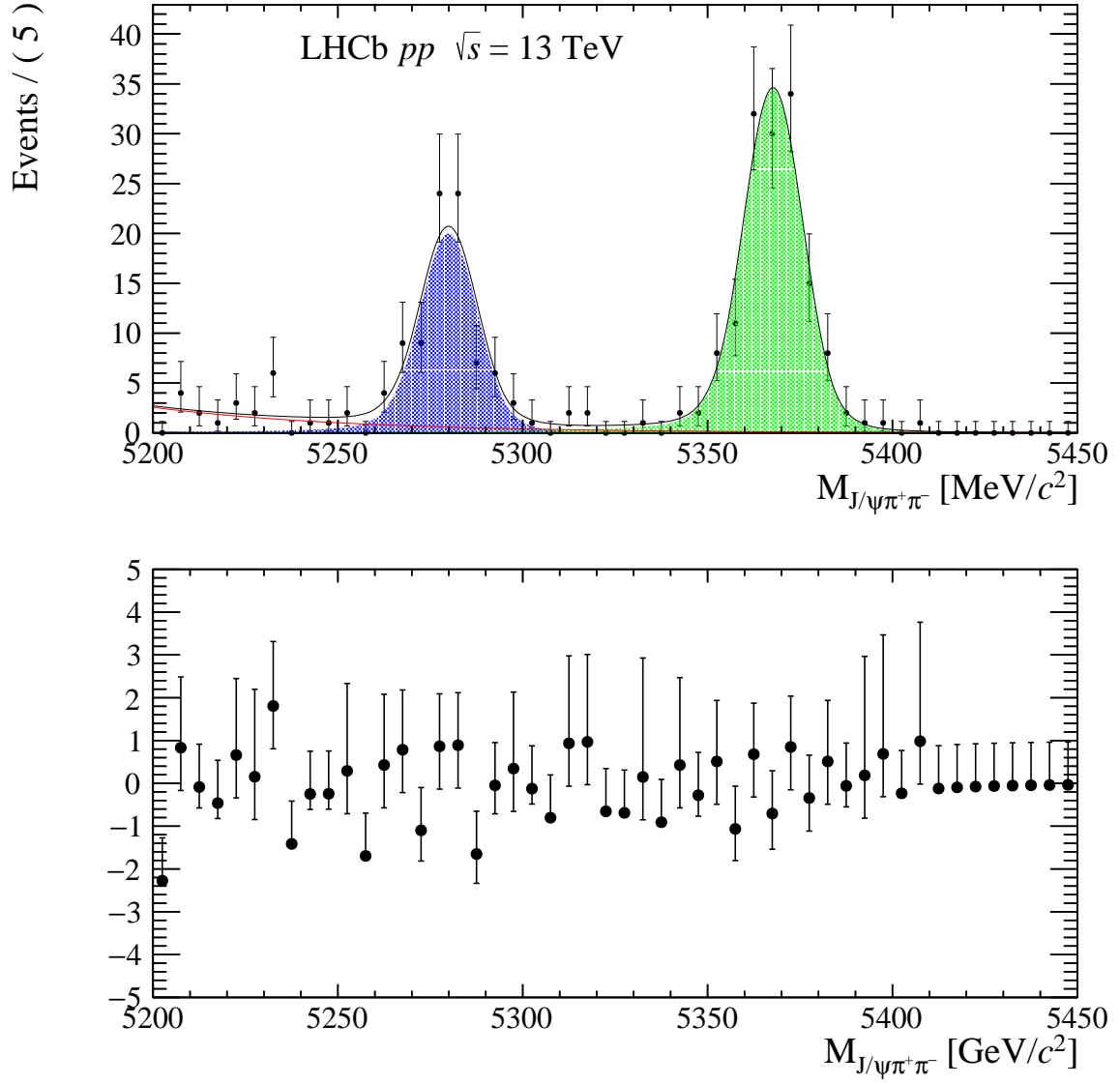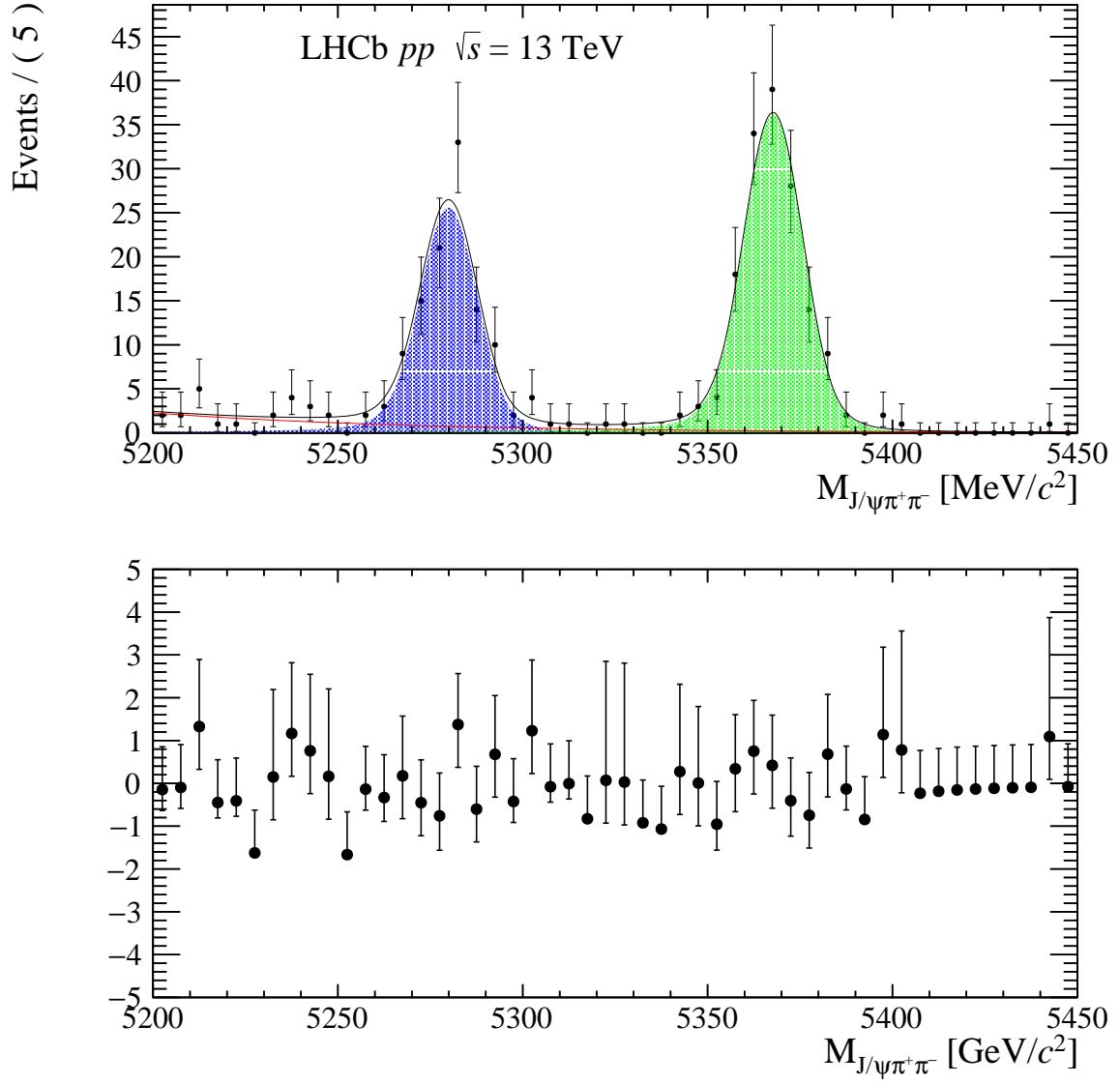
Figure 52: Fit to the $J/\psi\pi^+\pi^-$ mass spectrum in the multiplicity range $71 \le N_{tracks}^{VELO} \le 80$.
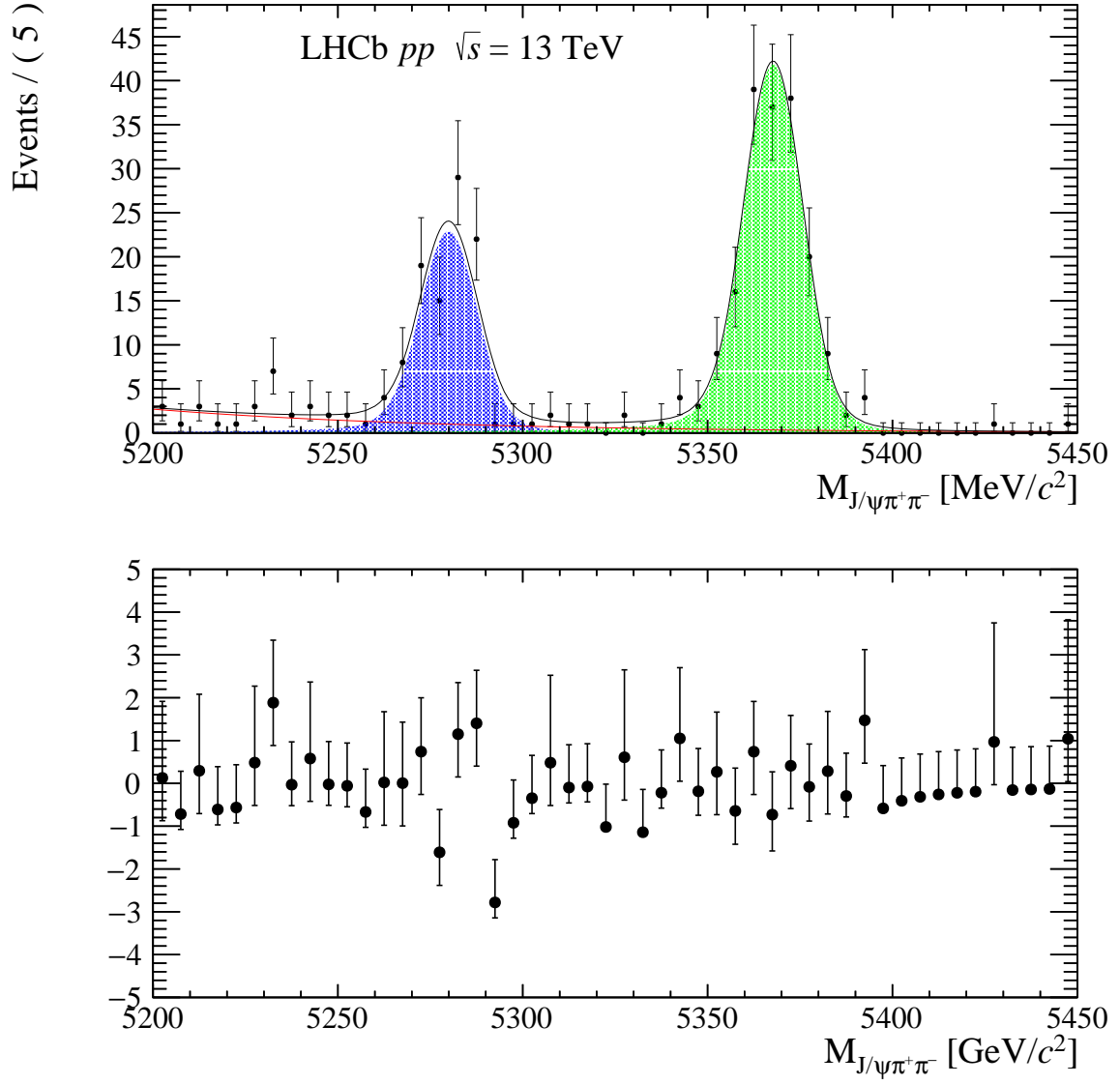
47
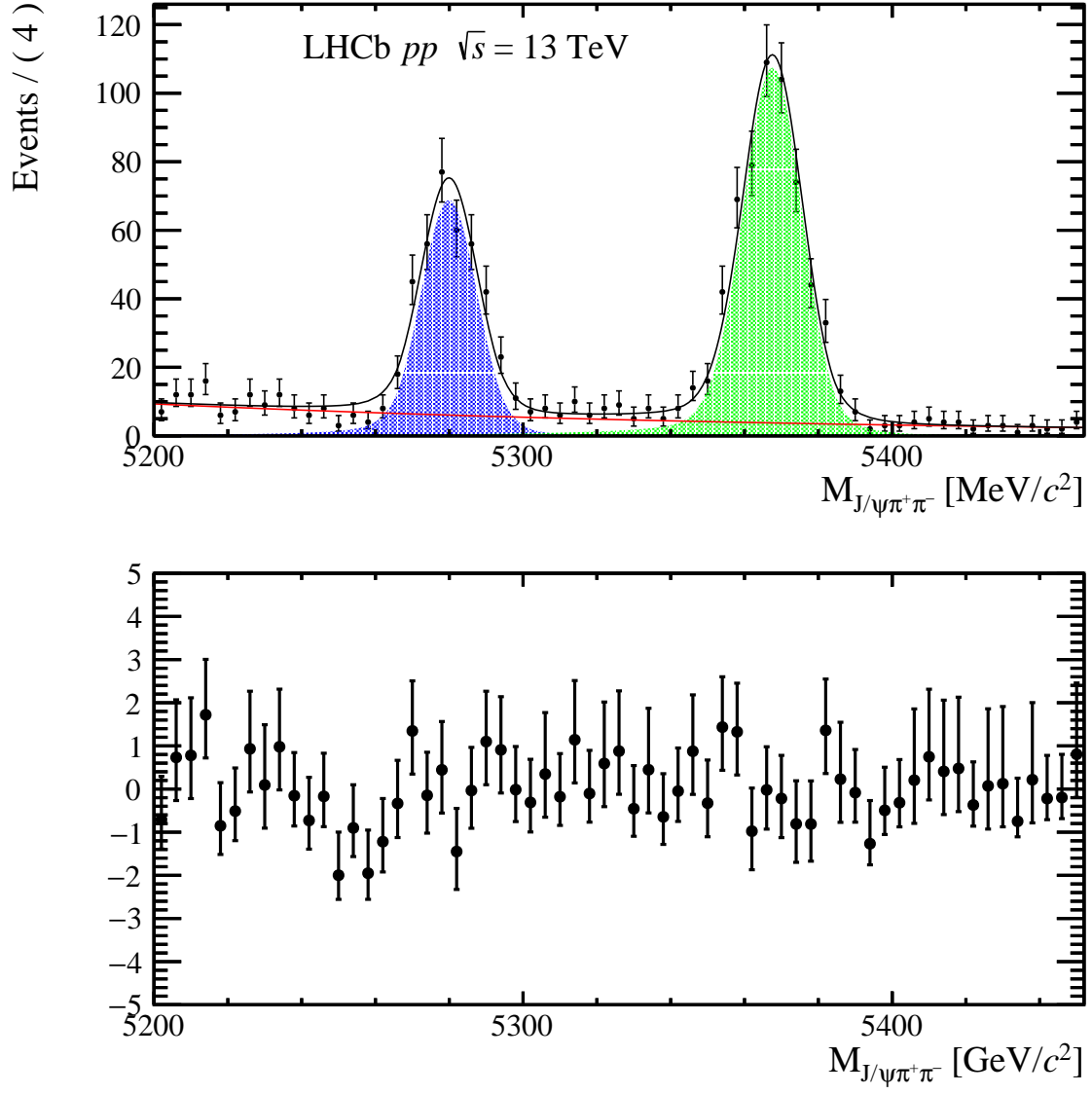
Figure 53: Fit to the $J/\psi\pi^+\pi^-$ mass spectrum in the multiplicity range $81 \leq N_{tracks}^{VELO} \leq 100$.
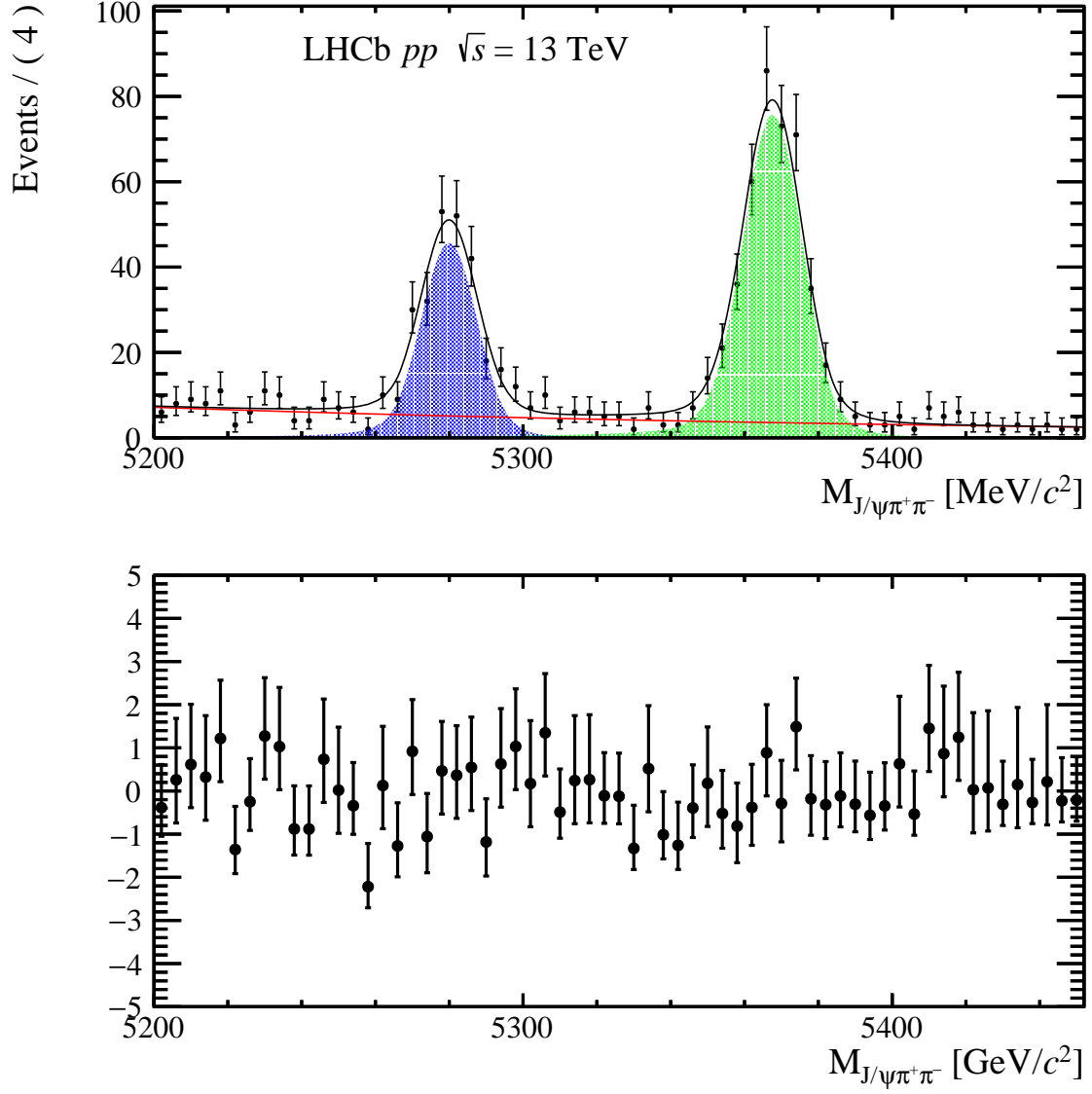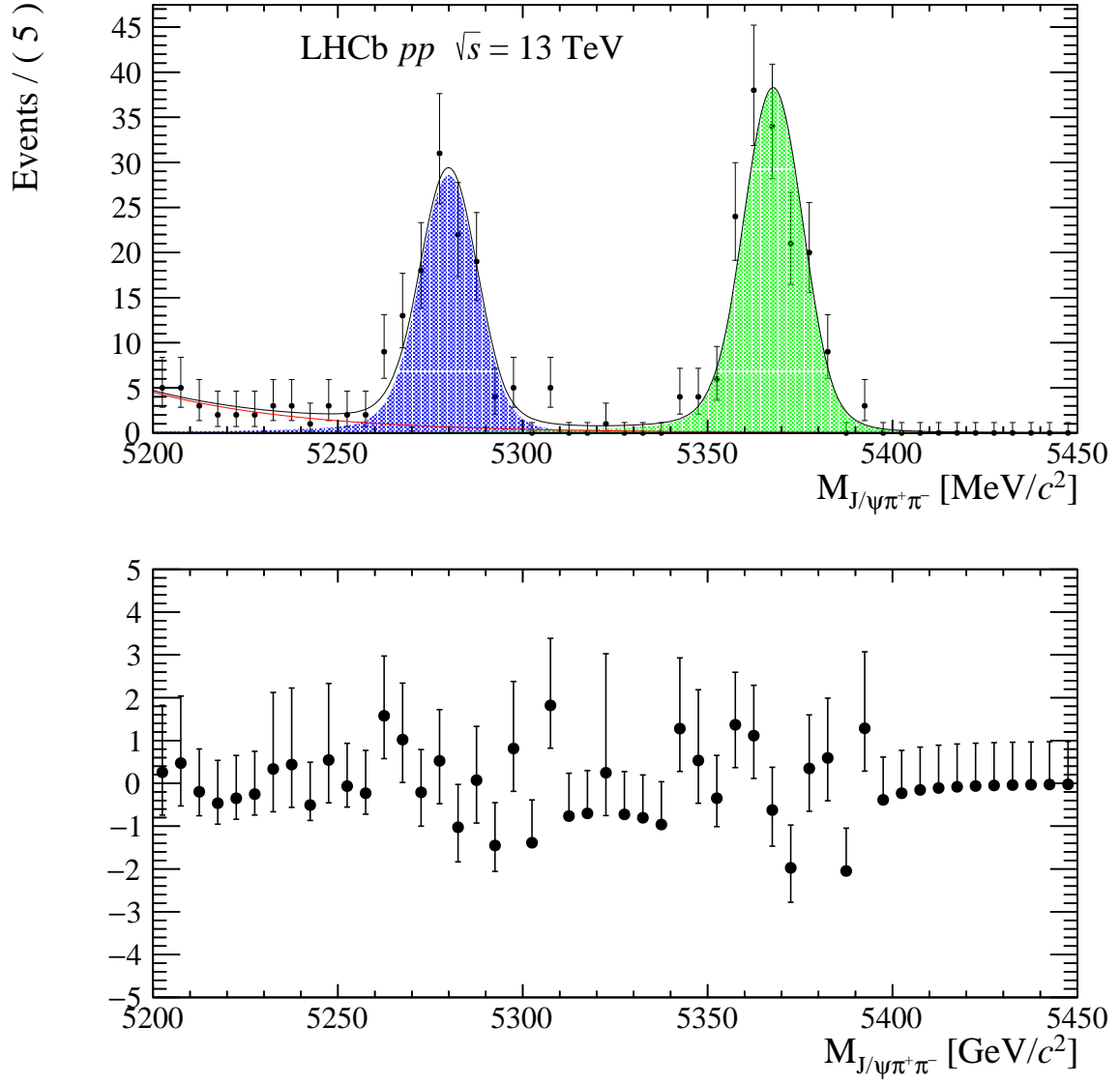
Figure 54: Fit to the $J/\psi\pi^+\pi^-$ mass spectrum in the multiplicity range $101 \leq N_{tracks}^{VELO} \leq 125$.
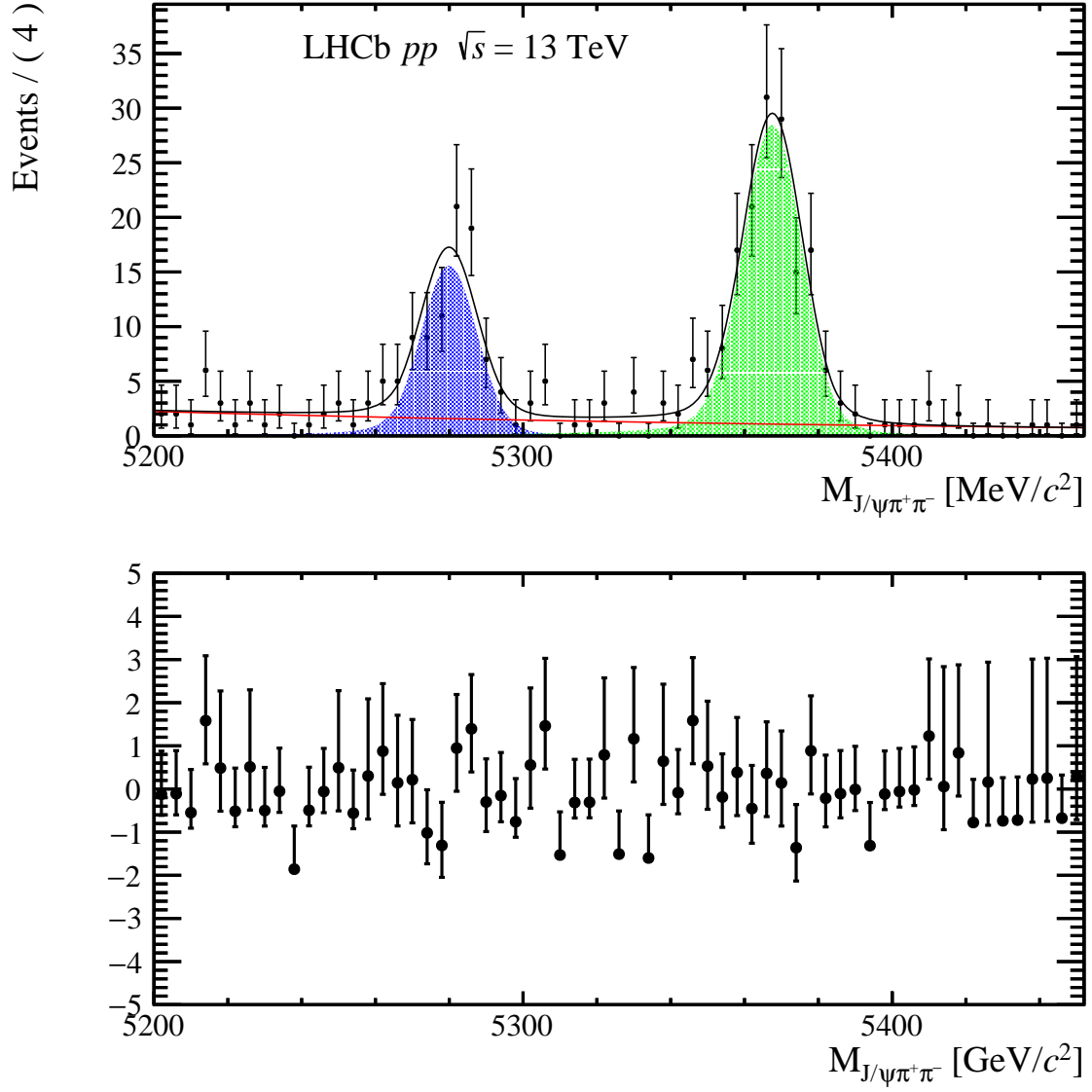
Figure 55: Fit to the $J/\psi\pi^+\pi^-$ mass spectrum in the multiplicity range $126 \leq N_{tracks}^{VELO} \leq 1500$.
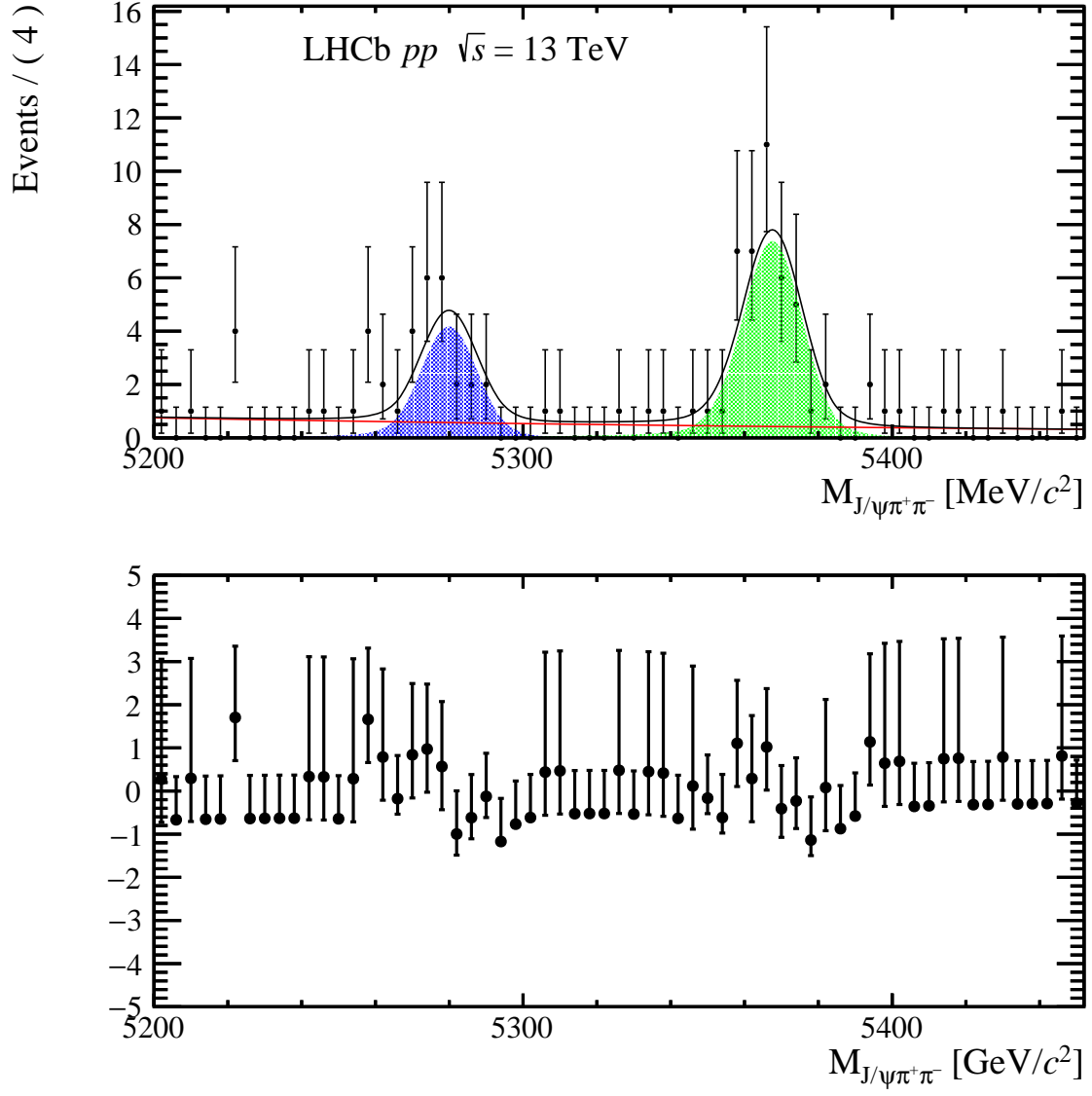
Figure 56: Fit to the $J/\psi\pi^+\pi^-$ mass spectrum in the multiplicity range $151 \le N_{tracks}^{VELO} \le 250$.
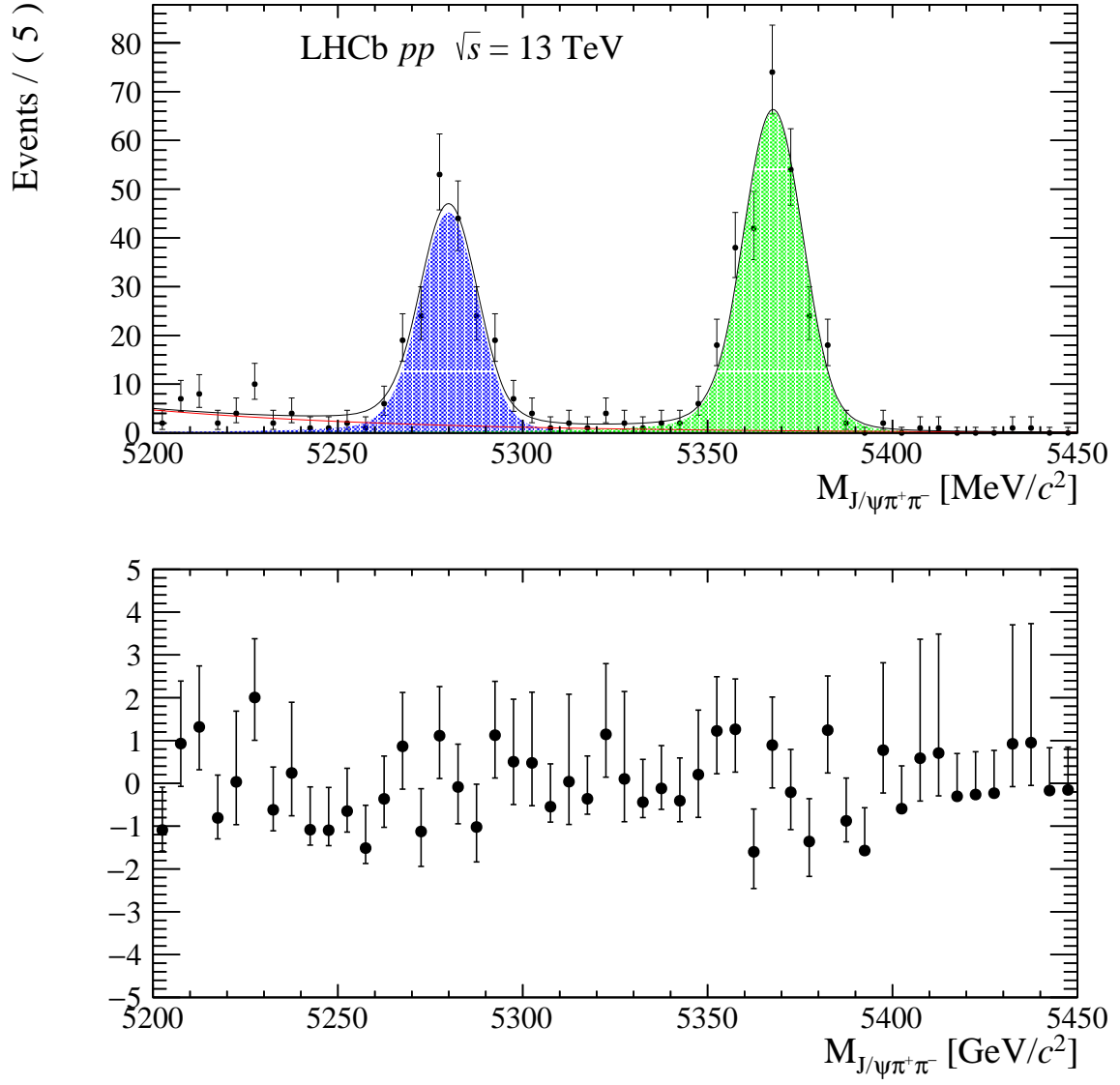
51
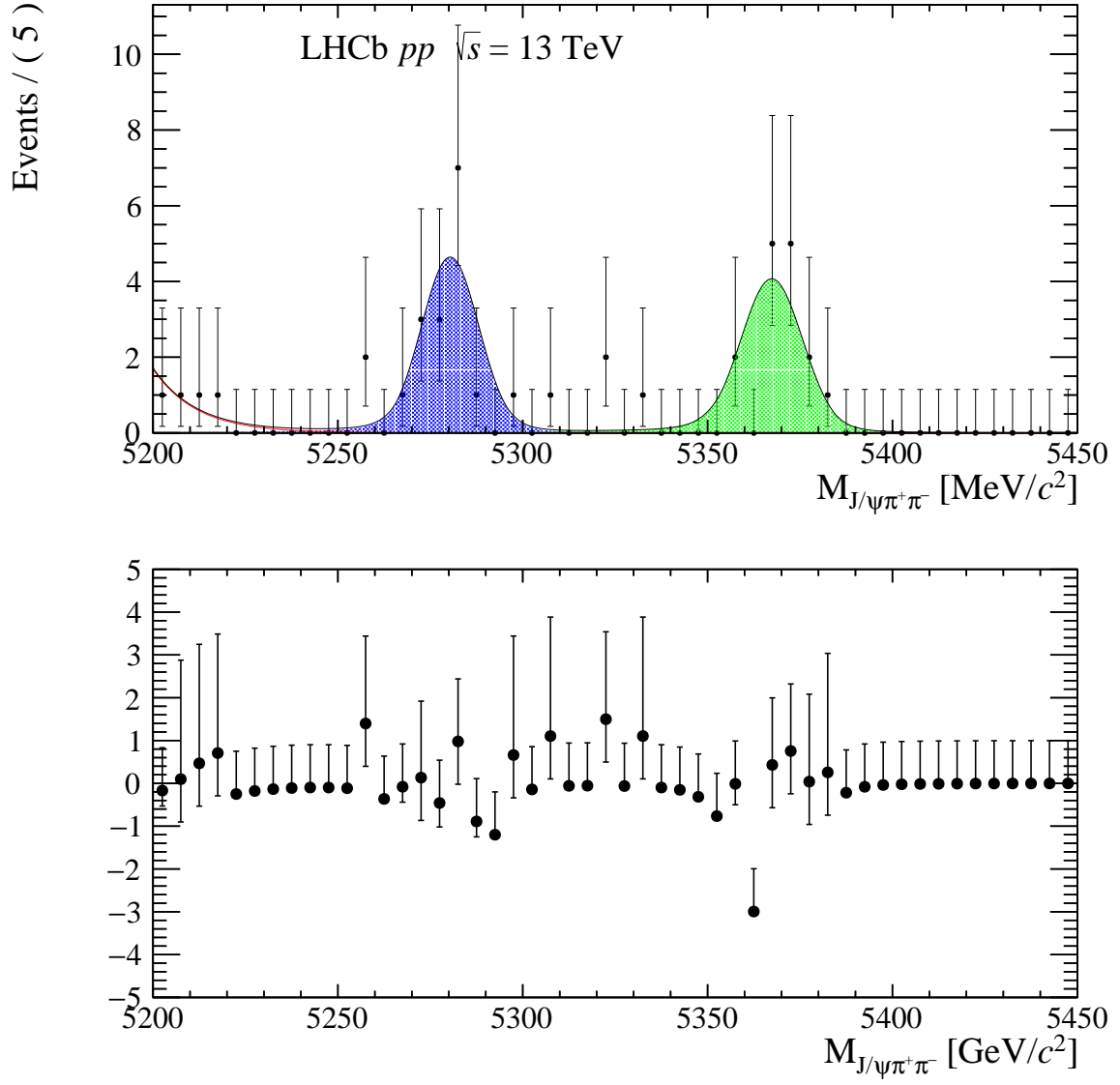
Figure 57: Fit to the $J/\psi\pi^+\pi^-$ mass spectrum in the multiplicity range $5 \leq N_{tracks}^{VELO} \leq 20$.
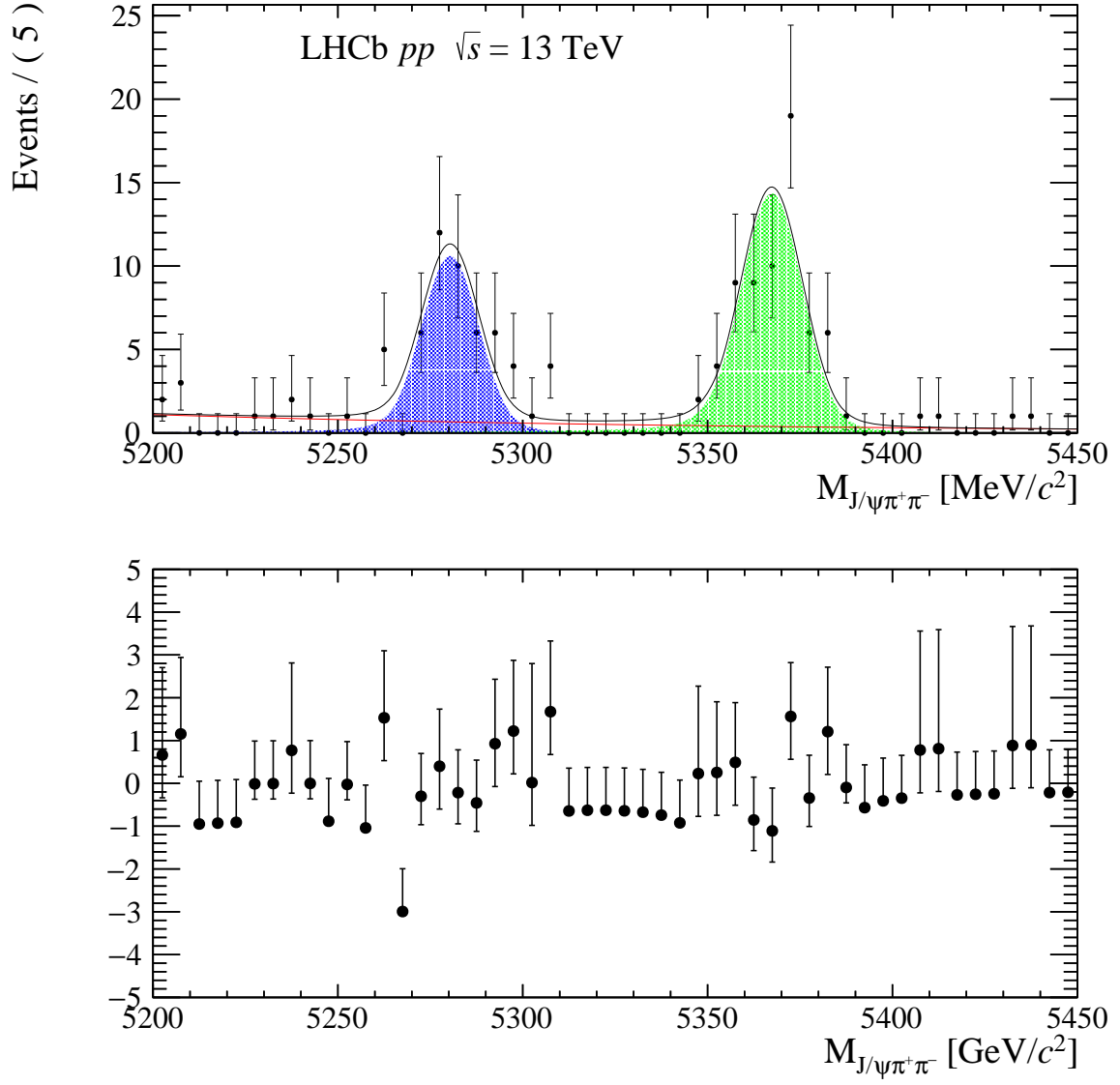
Figure 58: Fit to the $J/\psi\pi^+\pi^-$ mass spectrum in the multiplicity range $21 \leq N^{VELO}_{tracks} \leq 30$.
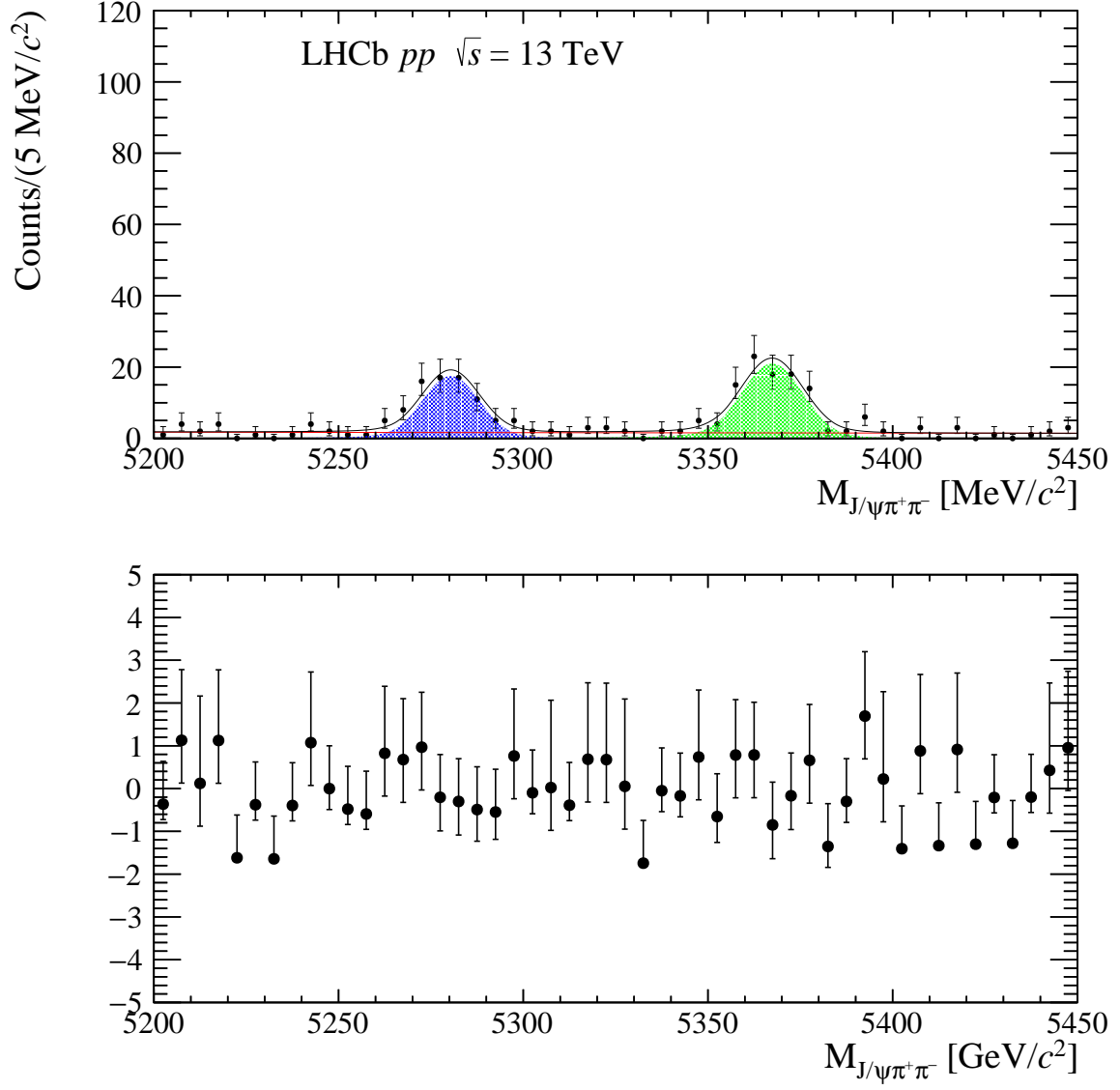
Figure 59: Fit to the $J/\psi\pi^+\pi^-$ mass spectrum in the multiplicity range $31 \leq N_{tracks}^{VELO} \leq 40$.
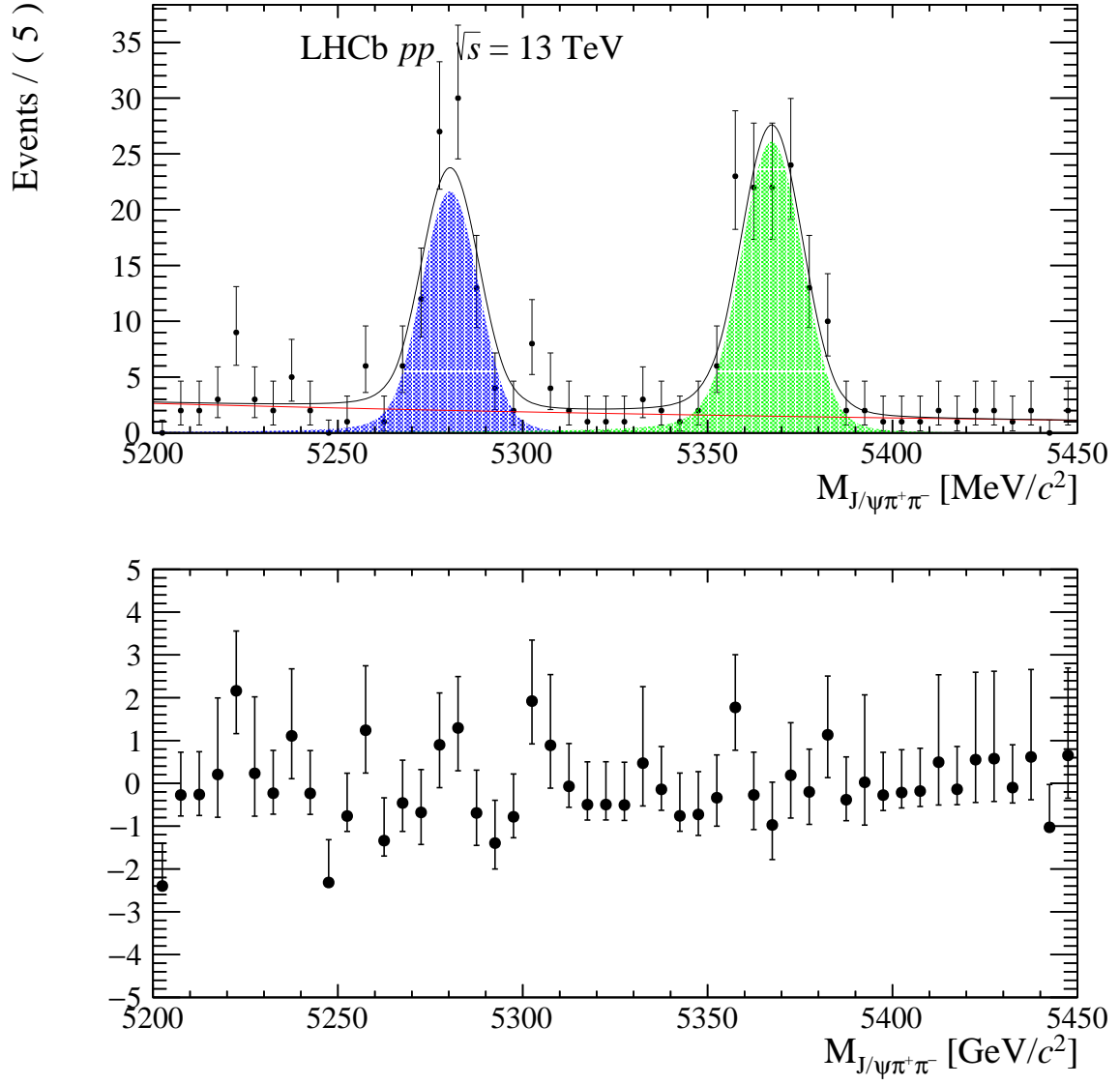
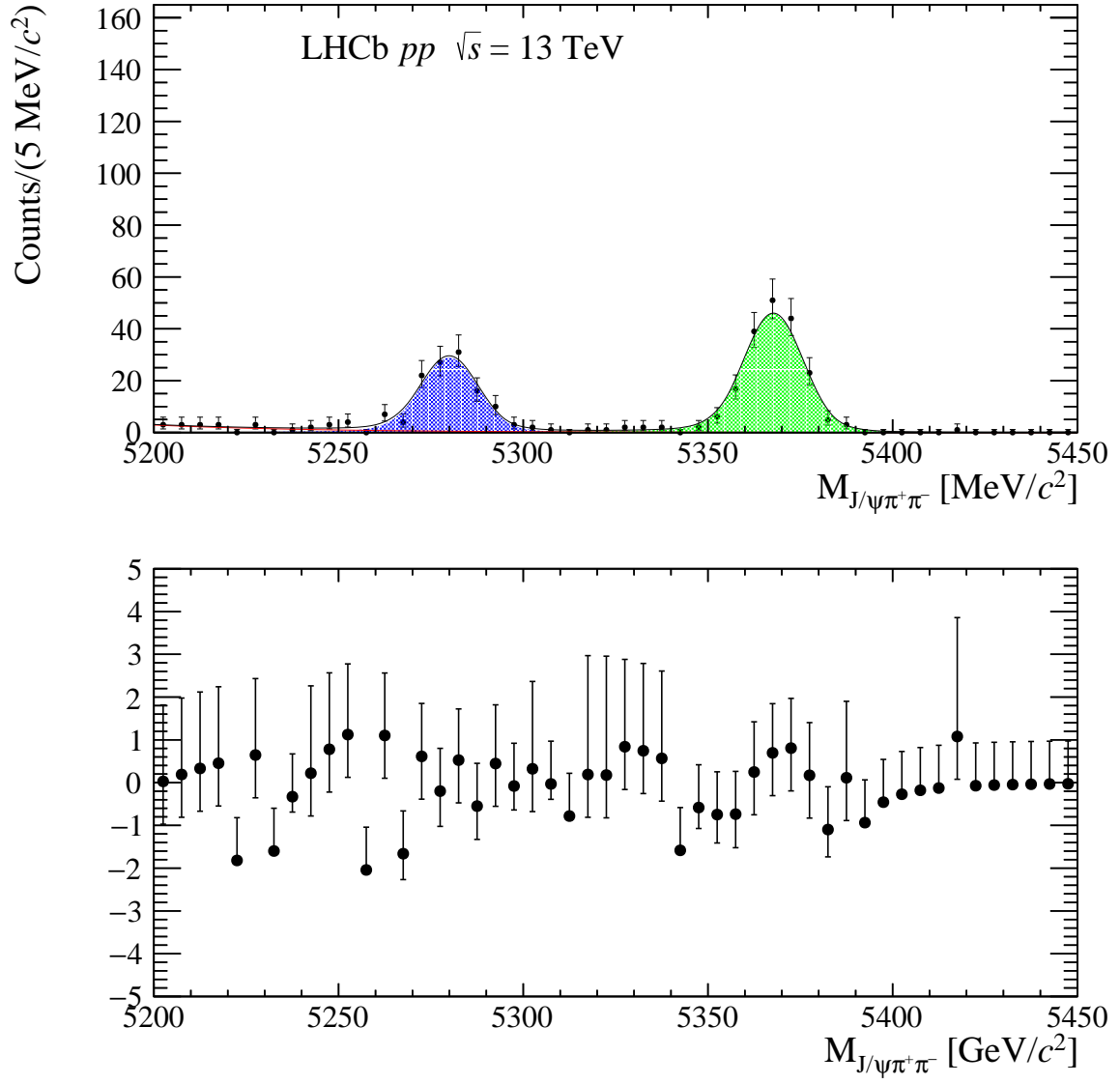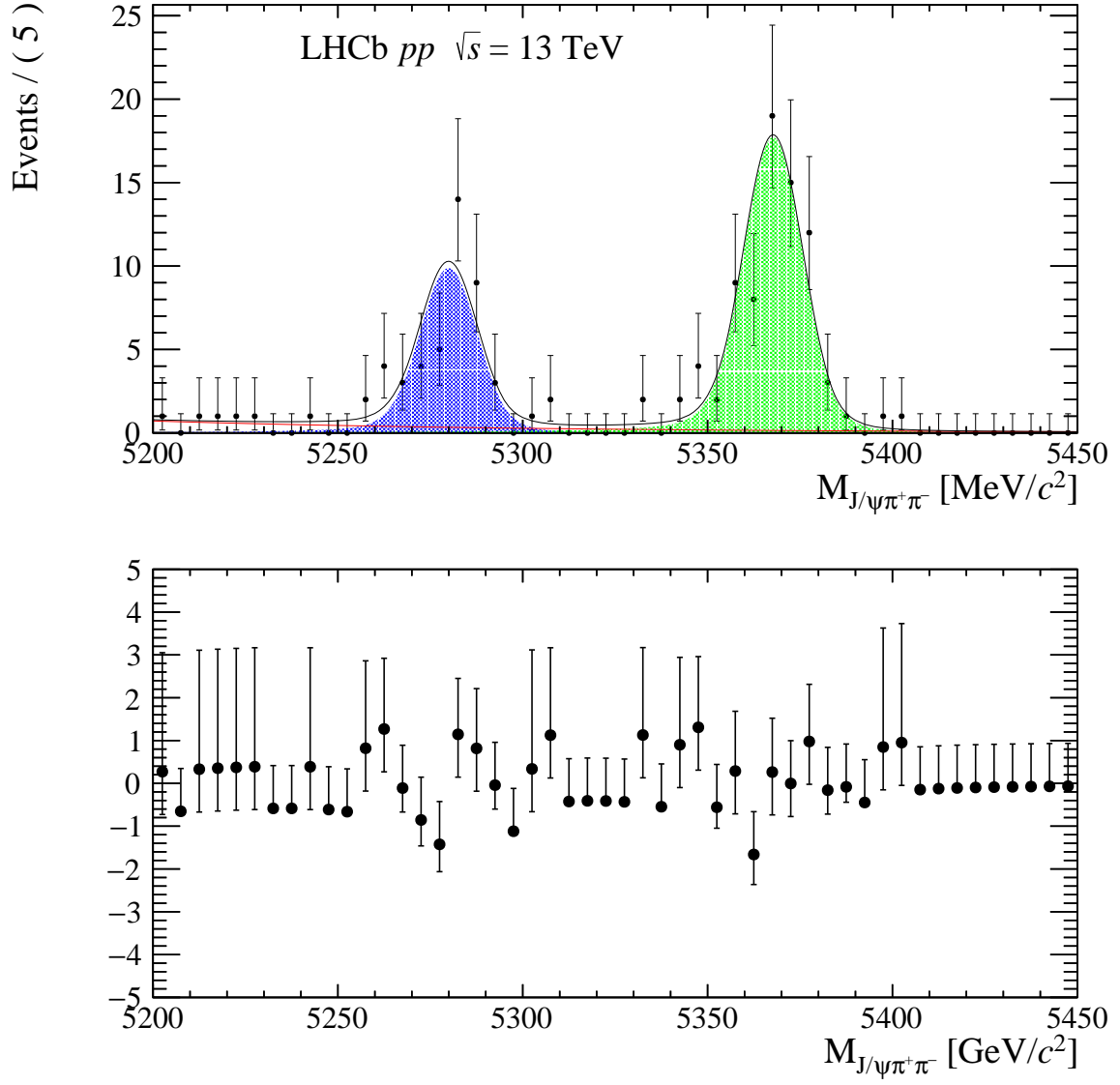Figure 60: Fit to the $J/\psi\pi^+\pi^-$ mass spectrum in the multiplicity range $41 \leq N_{tracks}^{VELO} \leq 50$.

Figure 61: Fit to the $J/\psi\pi^{+}\pi^{-}$ mass spectrum in the multiplicity range $51 \leq N^{VELO}_{tracks} \leq 60$.
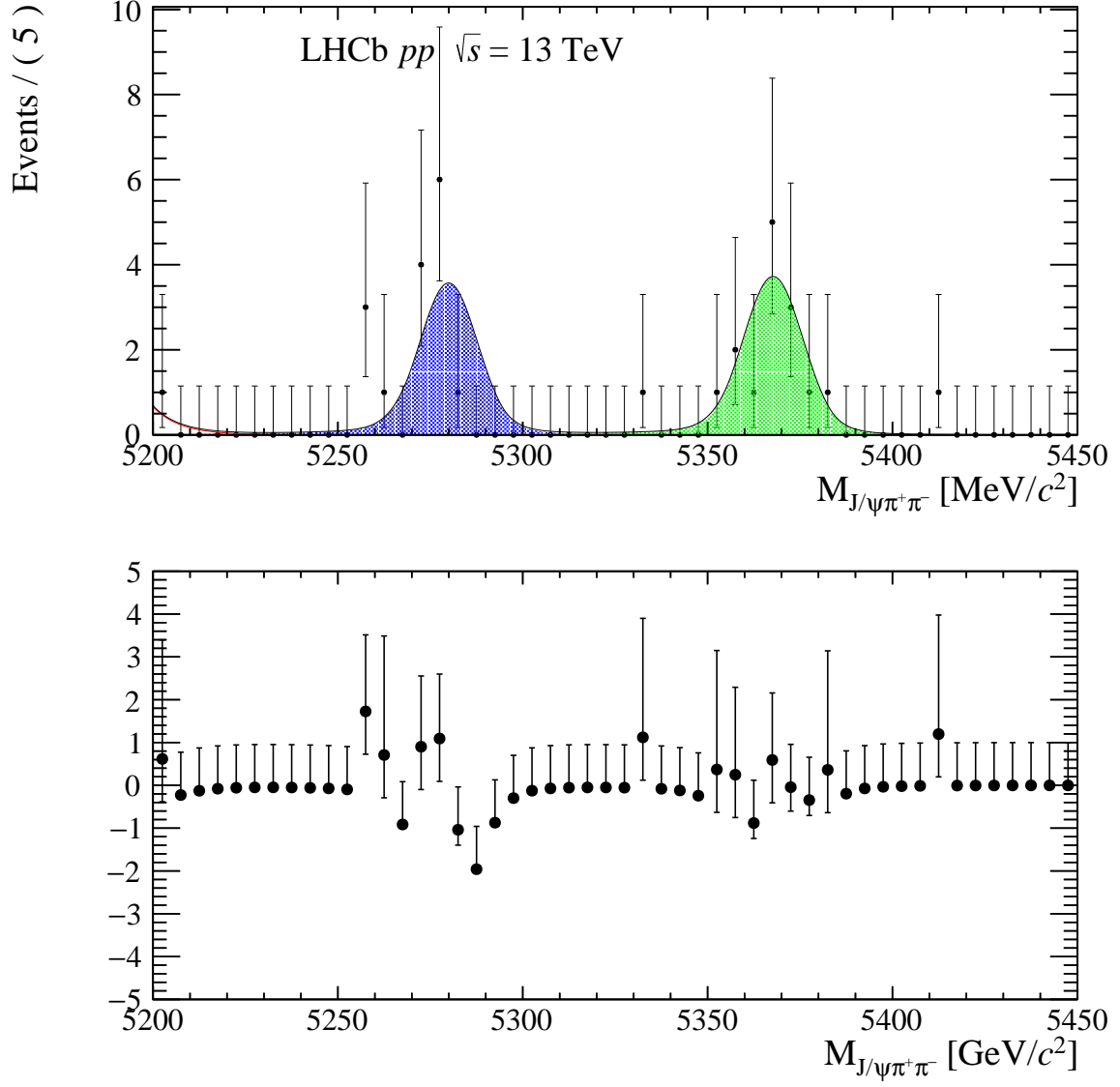
Figure 62: Fit to the $J/\psi\pi^+\pi^-$ mass spectrum in the multiplicity range $61 \leq N_{tracks}^{VELO} \leq 70$.

Figure 63: Fit to the $J/\psi\pi^+\pi^-$ mass spectrum in the multiplicity range $71 \leq N_{tracks}^{VELO} \leq 80$.

Figure 64: Fit to the $J/\psi\pi^+\pi^-$ mass spectrum in the multiplicity range $81 \leq N^{VELO}_{tracks} \leq 100$.

Figure 65: Fit to the $J/\psi\pi^+\pi^-$ mass spectrum in the multiplicity range $101 \leq N_{tracks}^{VELO} \leq 125$.
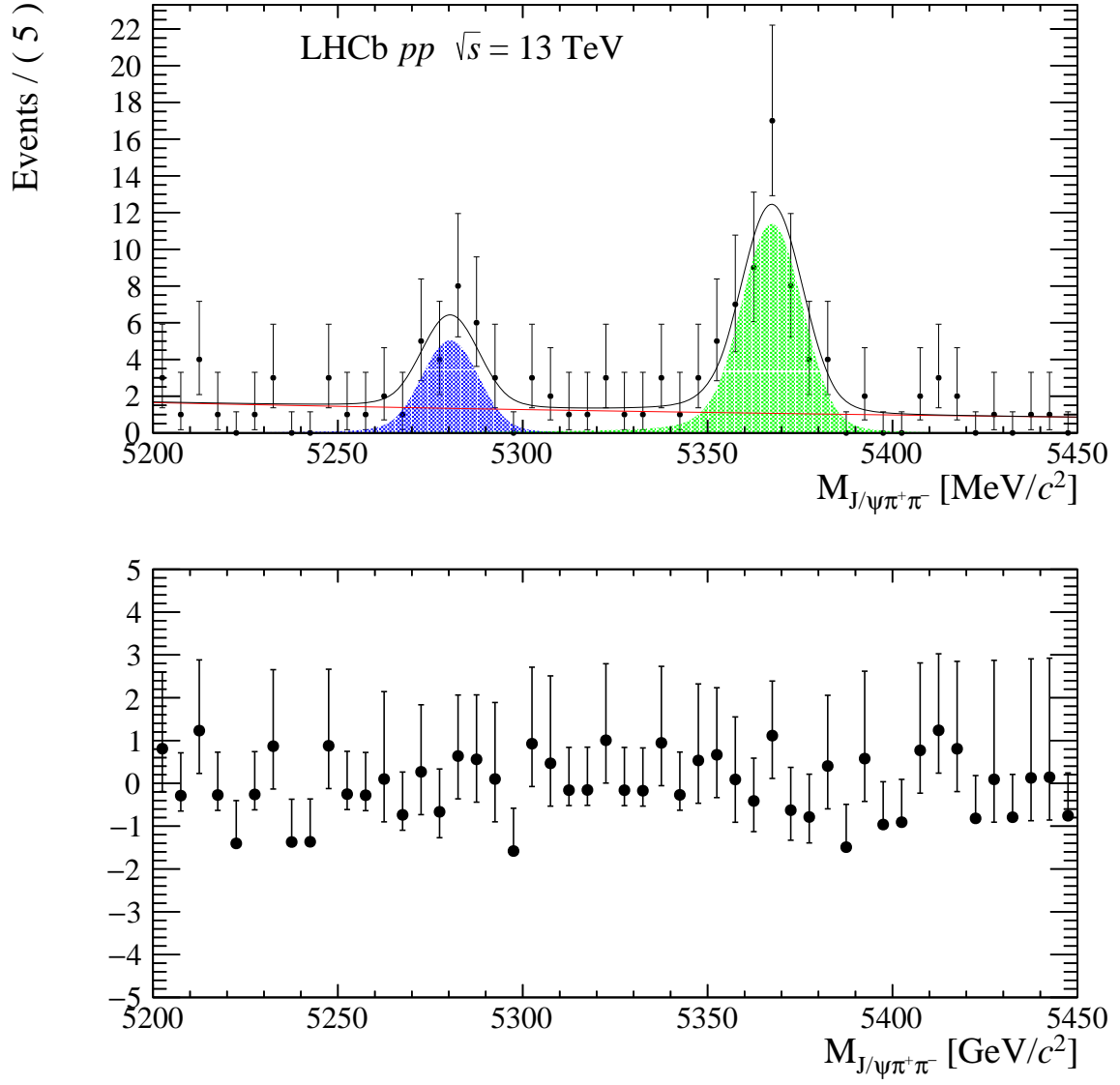
Figure 66: Fit to the $J/\psi\pi^+\pi^-$ mass spectrum in the multiplicity range $126 \leq N_{tracks}^{VELO} \leq 1500$.

Figure 67: Fit to the $J/\psi\pi^+\pi^-$ mass spectrum in the multiplicity range $151 \leq N_{tracks}^{VELO} \leq 250$.
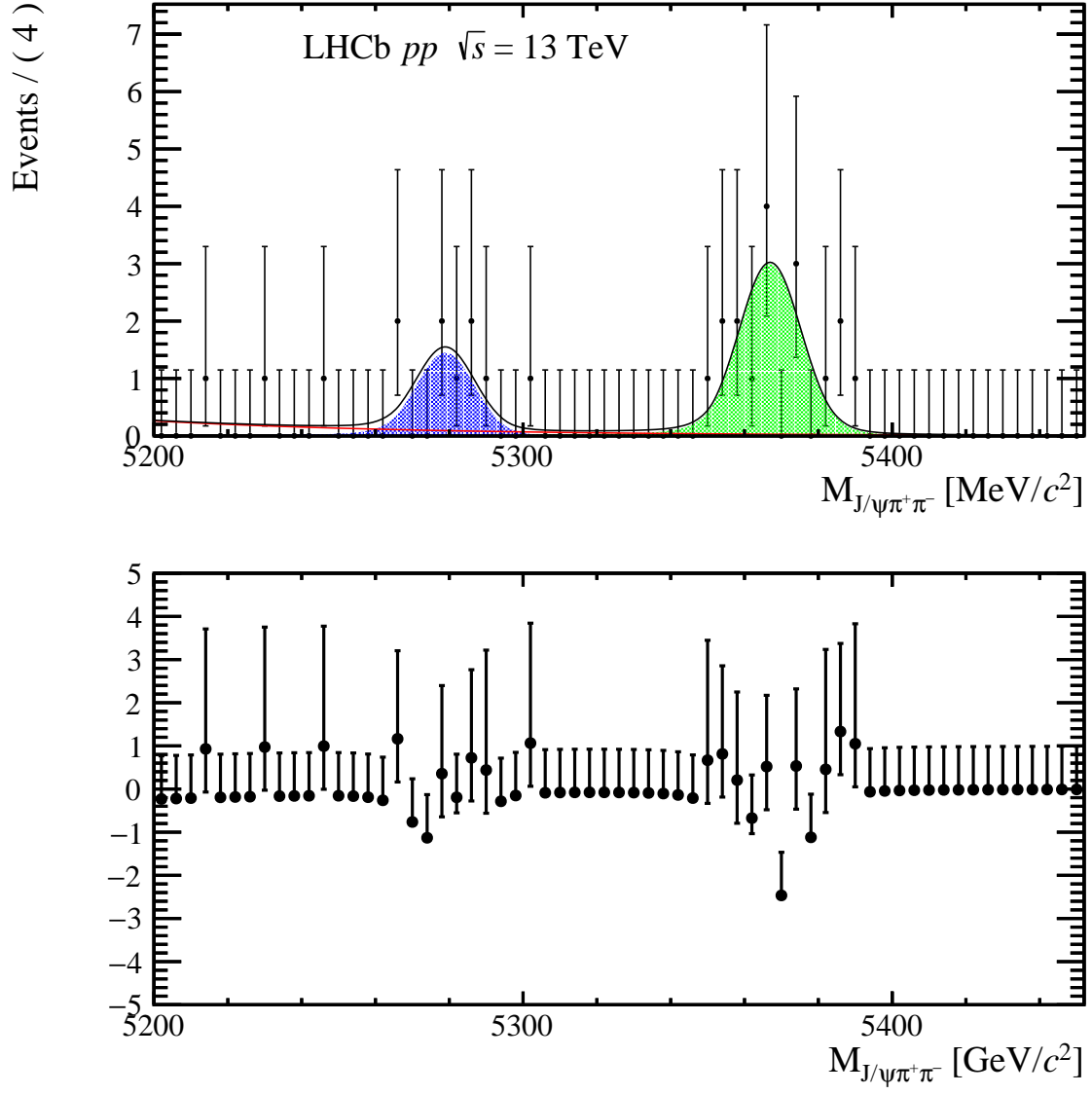
Figure 68: Fit to the $J/\psi\pi^+\pi^-$ mass spectrum in the multiplicity range $5 \leq N_{tracks}^{VELO} \leq 20$.
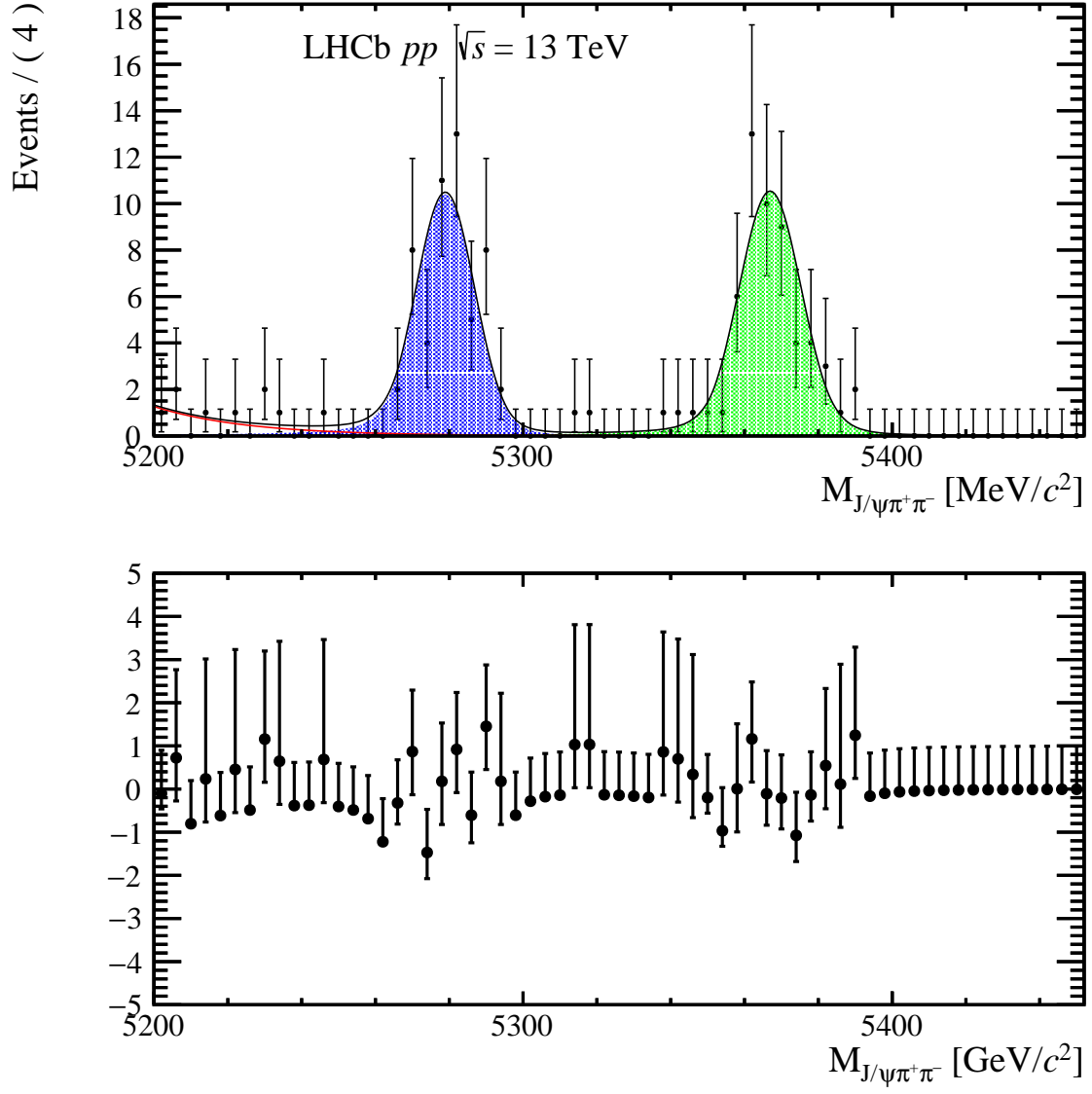
Figure 69: Fit to the $J/\psi\pi^+\pi^-$ mass spectrum in the multiplicity range $21 \leq N_{tracks}^{VELO} \leq 30$.

Figure 70: Fit to the $J/\psi\pi^+\pi^-$ mass spectrum in the multiplicity range $31 \leq N_{tracks}^{VELO} \leq 40$.
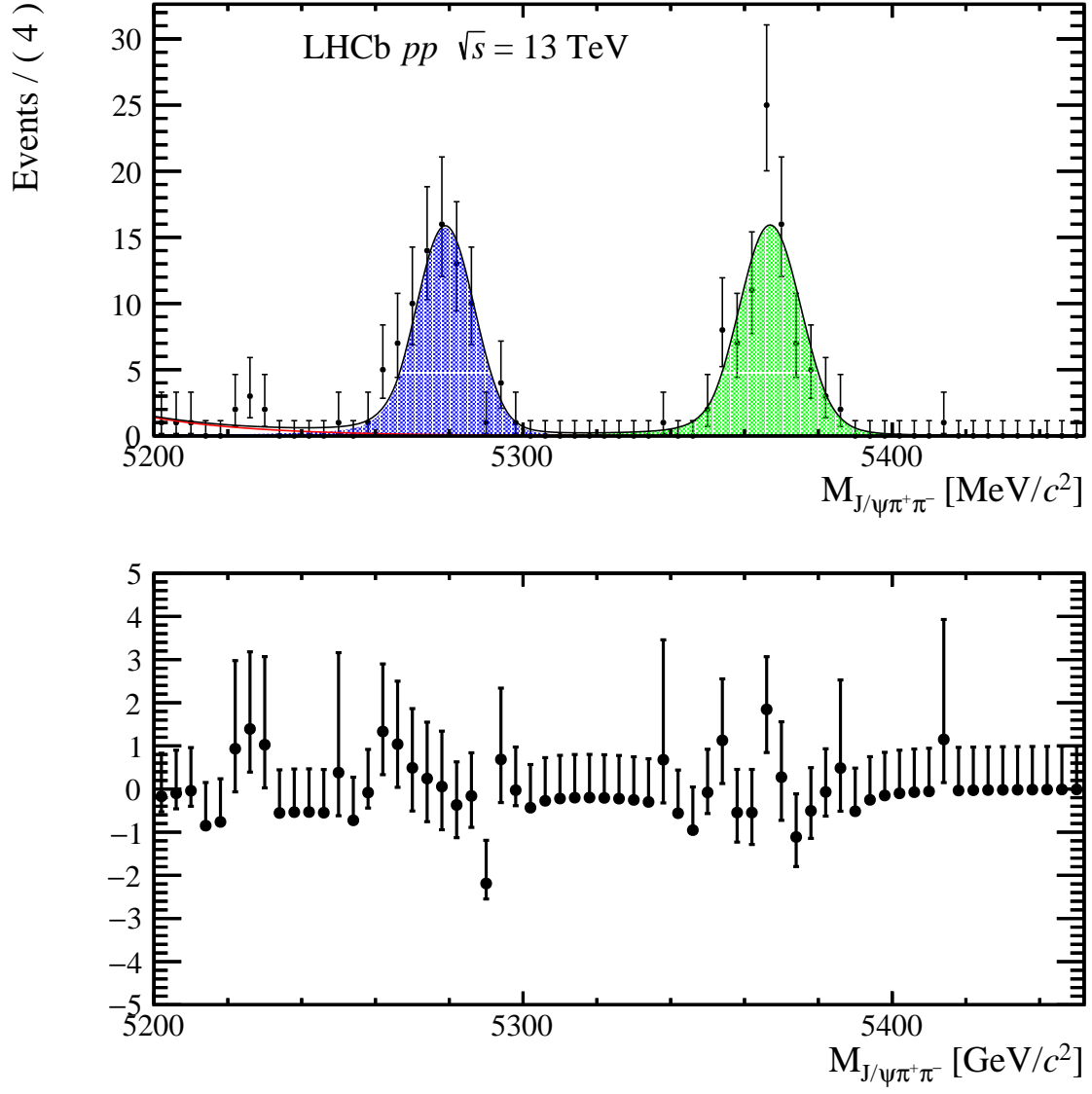
Figure 71: Fit to the $J/\psi\pi^+\pi^-$ mass spectrum in the multiplicity range $41 \leq N_{tracks}^{VELO} \leq 50$.

Figure 72: Fit to the $J/\psi\pi^+\pi^-$ mass spectrum in the multiplicity range $51 \leq N_{tracks}^{VELO} \leq 60$.
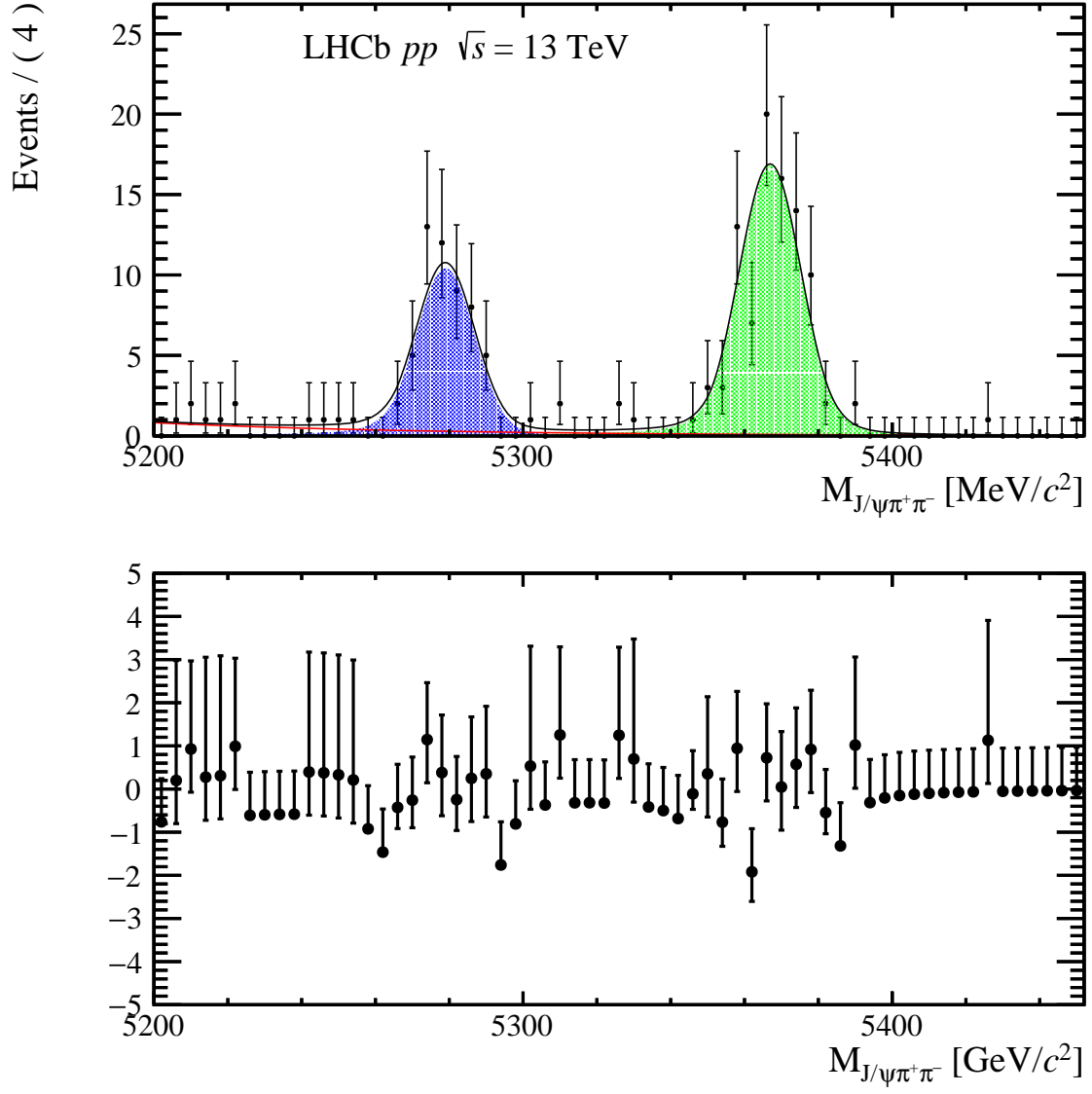
Figure 73: Fit to the $J/\psi\pi^+\pi^-$ mass spectrum in the multiplicity range $61 \leq N_{tracks}^{VELO} \leq 70$.

Figure 74: Fit to the $J/\psi\pi^+\pi^-$ mass spectrum in the multiplicity range $71 \leq N_{tracks}^{VELO} \leq 80$.
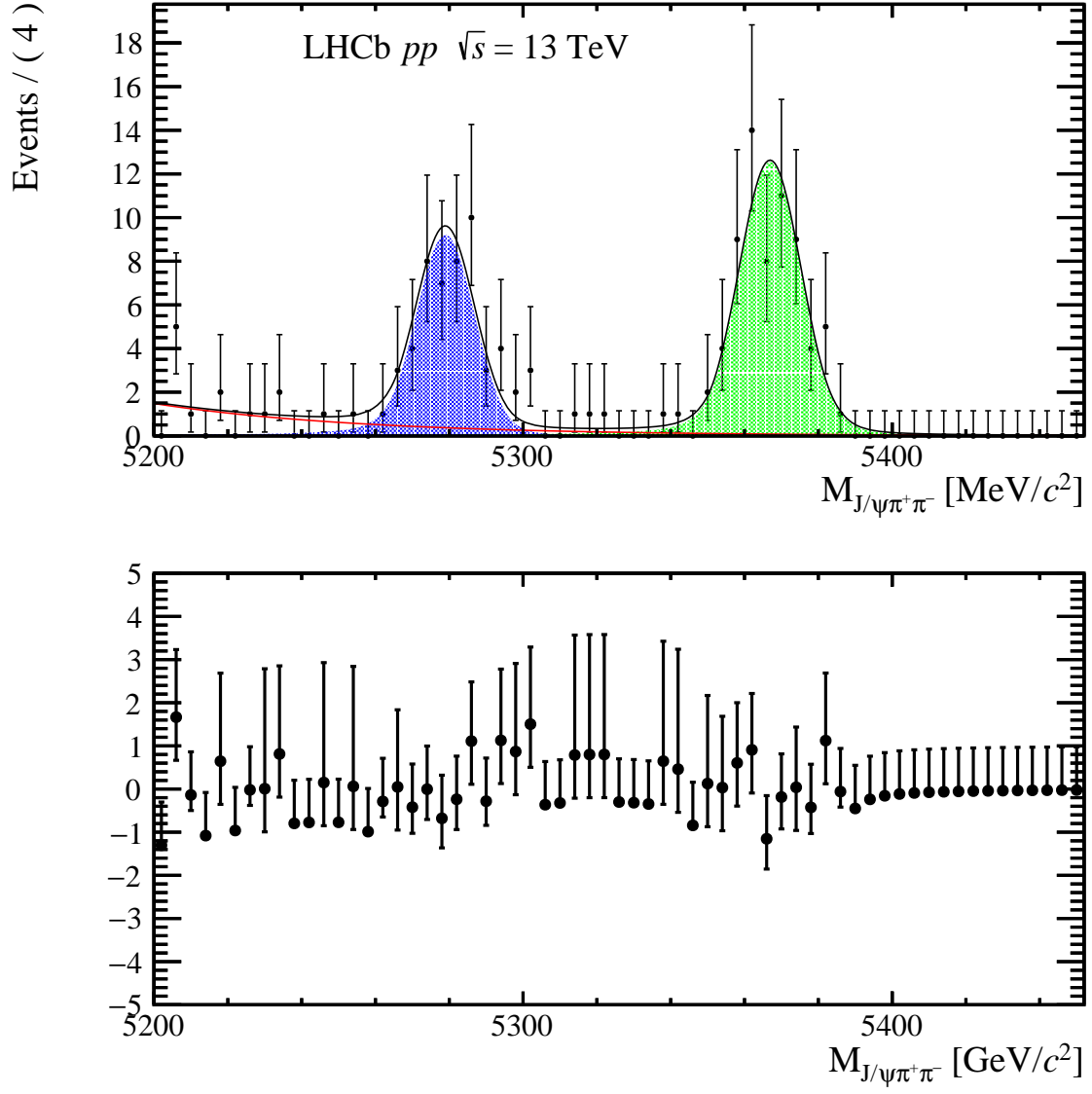
Figure 75: Fit to the $J/\psi\pi^+\pi^-$ mass spectrum in the multiplicity range $81 \leq N_{tracks}^{VELO} \leq 100$.
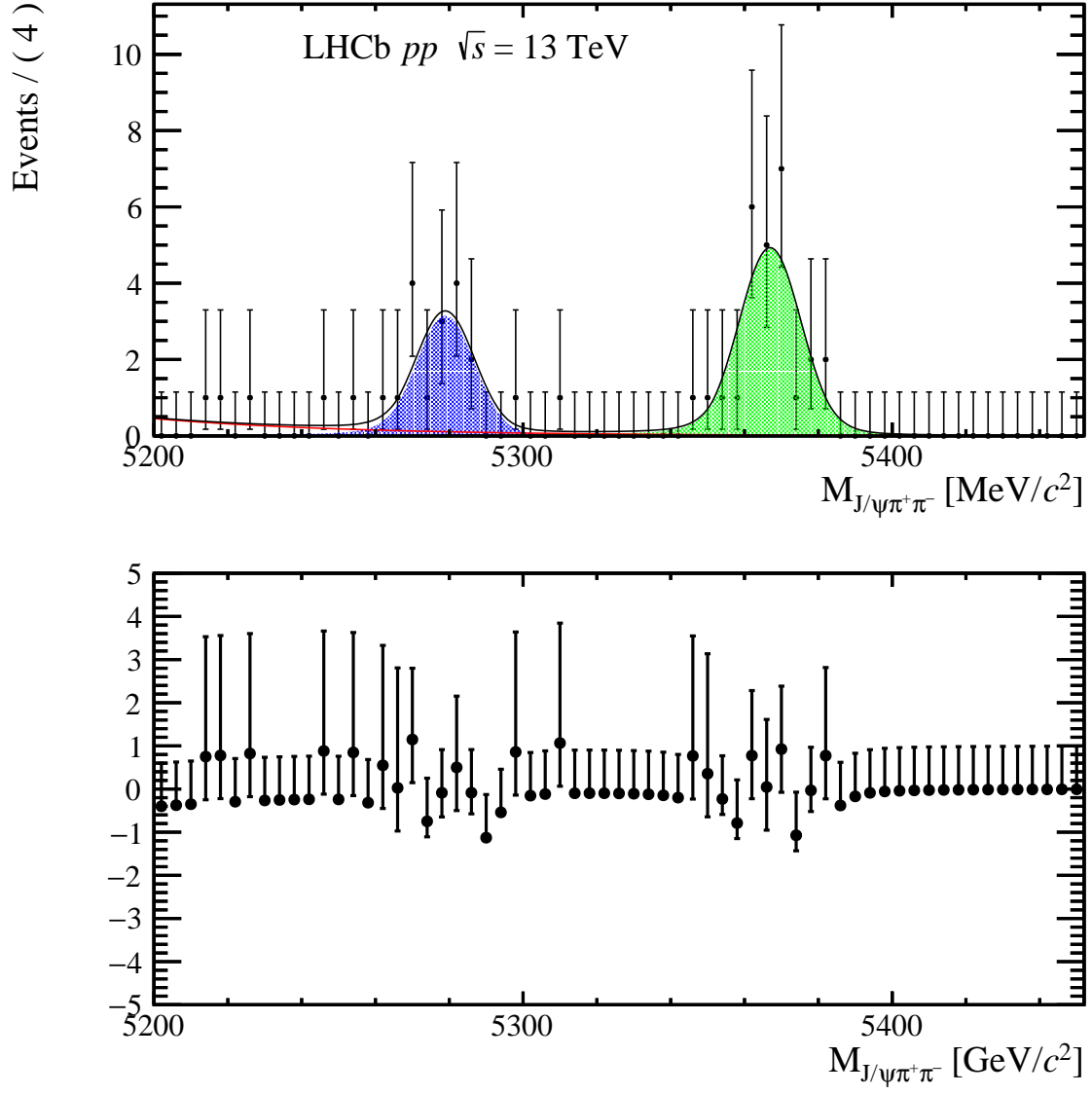
Figure 76: Fit to the $J/\psi\pi^+\pi^-$ mass spectrum in the multiplicity range $101 \leq N_{tracks}^{VELO} \leq 125$.

Figure 77: Fit to the $J/\psi\pi^{+}\pi^{-}$ mass spectrum in the multiplicity range $126 \leq N_{tracks}^{VELO} \leq 1500$.

Figure 78: Fit to the $J/\psi\pi^+\pi^-$ mass spectrum in the multiplicity range $151 \leq N_{tracks}^{VELO} \leq 250$.
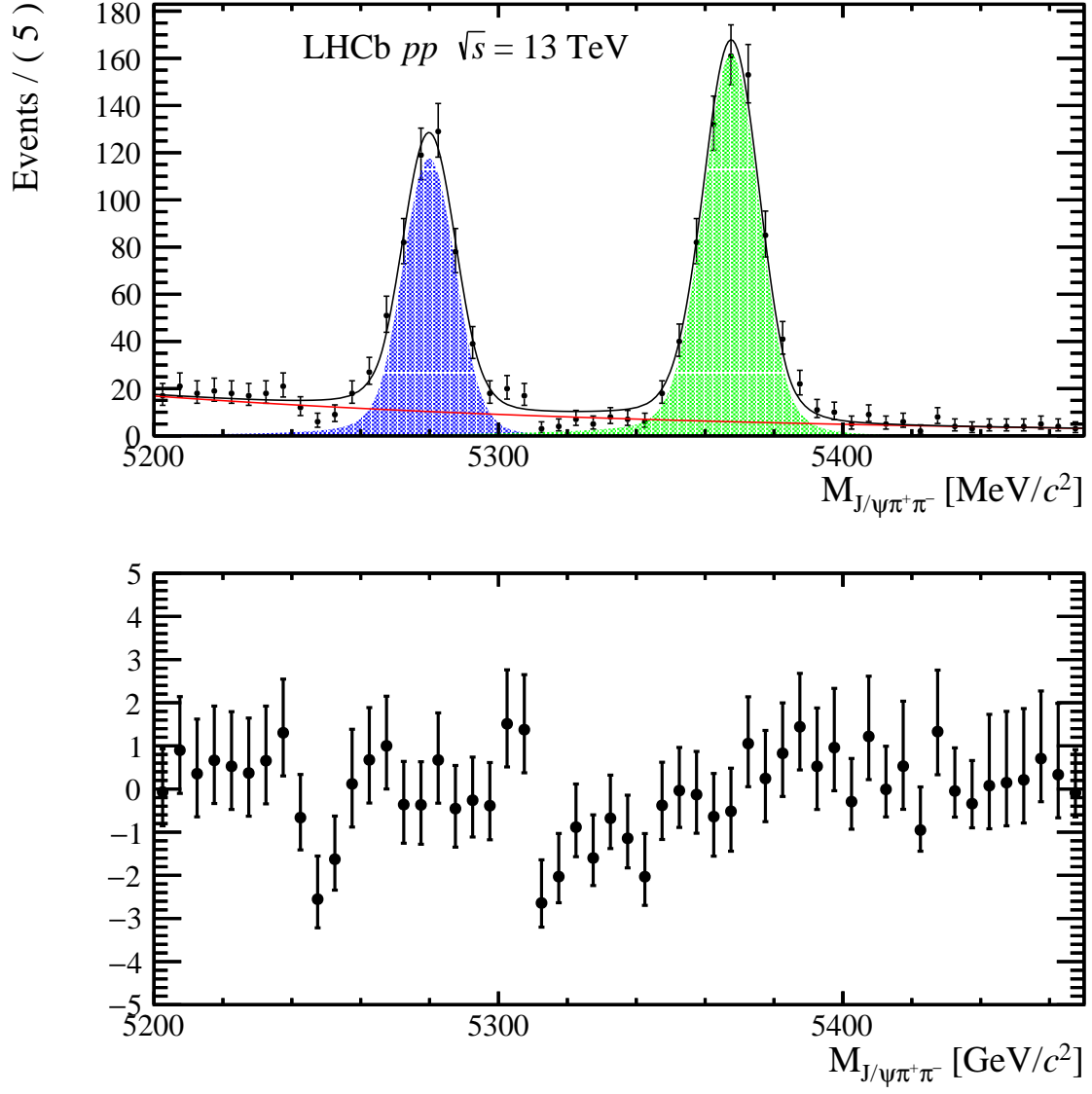
Figure 79: Fit to the $J/\psi\pi^+\pi^-$ mass spectrum in the multiplicity range $5 \leq N_{tracks}^{VELO} \leq 30$.
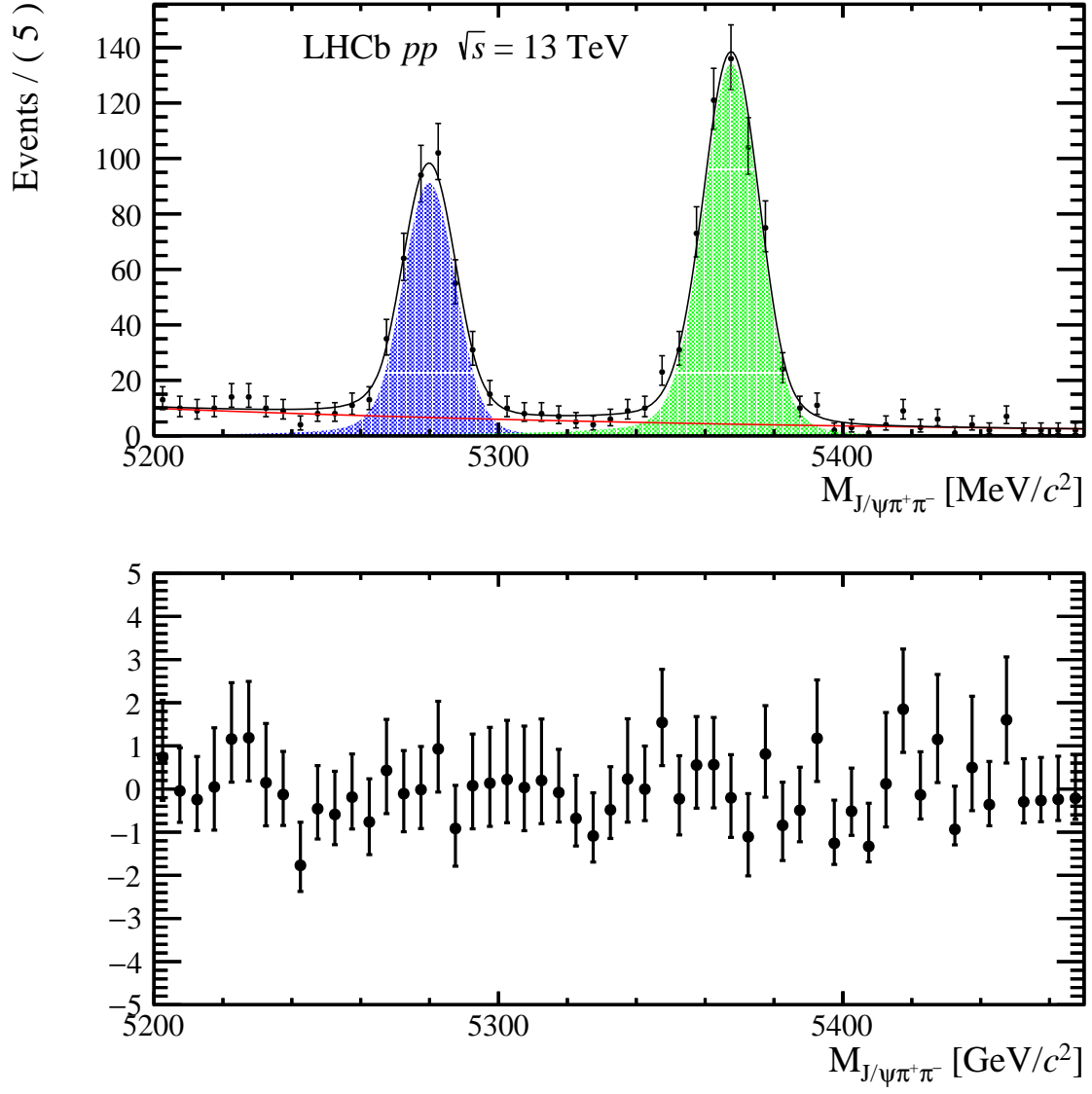
Figure 80: Fit to the $J/\psi\pi^+\pi^-$ mass spectrum in the multiplicity range $31 \leq N_{tracks}^{VELO} \leq 50$.

Figure 81: Fit to the $J/\psi\pi^+\pi^-$ mass spectrum in the multiplicity range $51 \leq N_{tracks}^{VELO} \leq 70$.
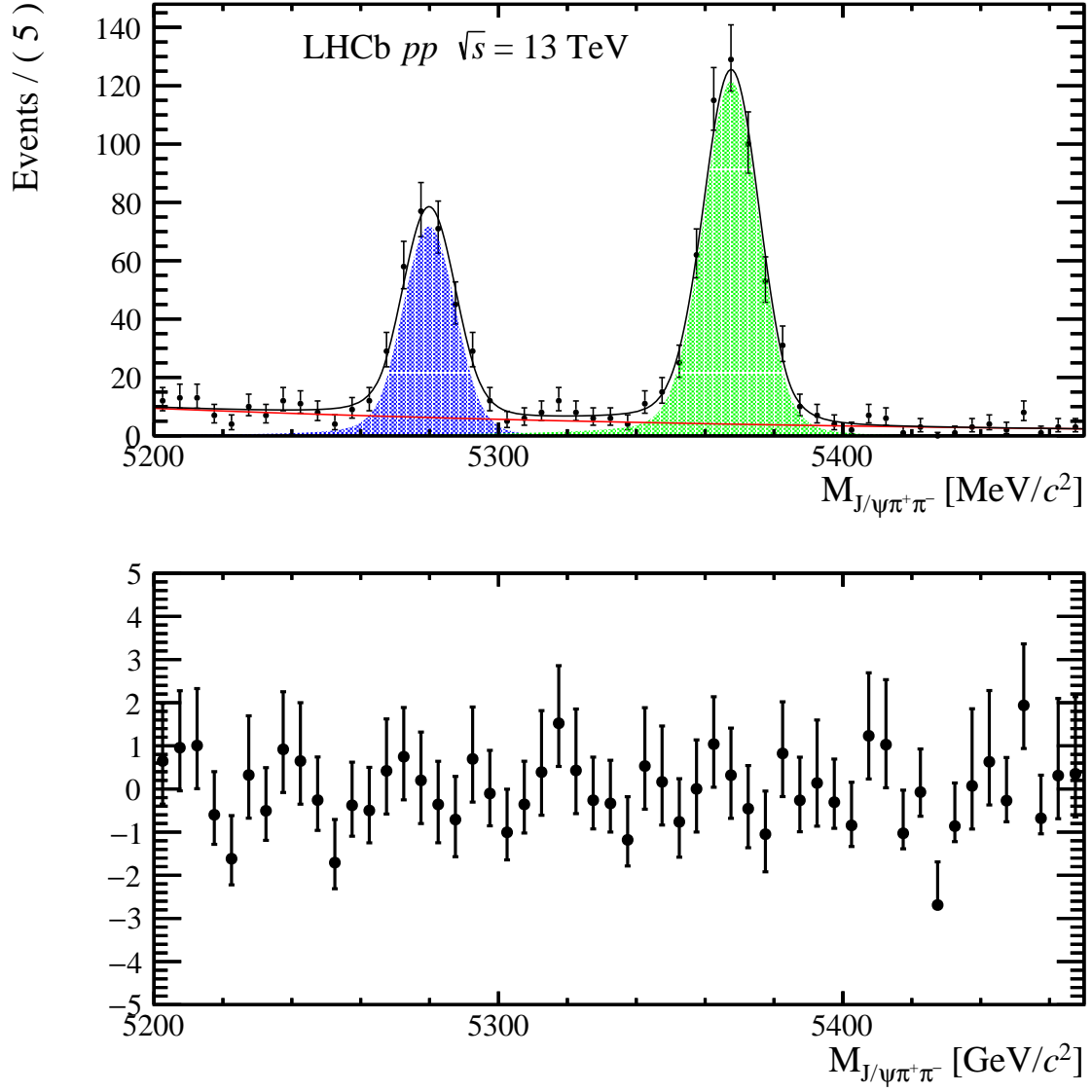
76

Figure 82: Fit to the $J/\psi\pi^+\pi^-$ mass spectrum in the multiplicity range $71 \leq N_{tracks}^{VELO} \leq 90$.

Figure 83: Fit to the $J/\psi\pi^+\pi^-$ mass spectrum in the multiplicity range $91 \leq N_{tracks}^{VELO} \leq 125$.

Figure 84: Fit to the $J/\psi\pi^+\pi^-$ mass spectrum in the multiplicity range $126 \leq N_{tracks}^{VELO} \leq 250$.

Figure 85: Fit to the $J/\psi\pi^+\pi^-$ mass spectrum in the multiplicity range $0 \leq N_{tracks}^{back} \leq 10$.

Figure 86: Fit to the $J/\psi\pi^+\pi^-$ mass spectrum in the multiplicity range $11 \leq N_{tracks}^{back} \leq 15$.
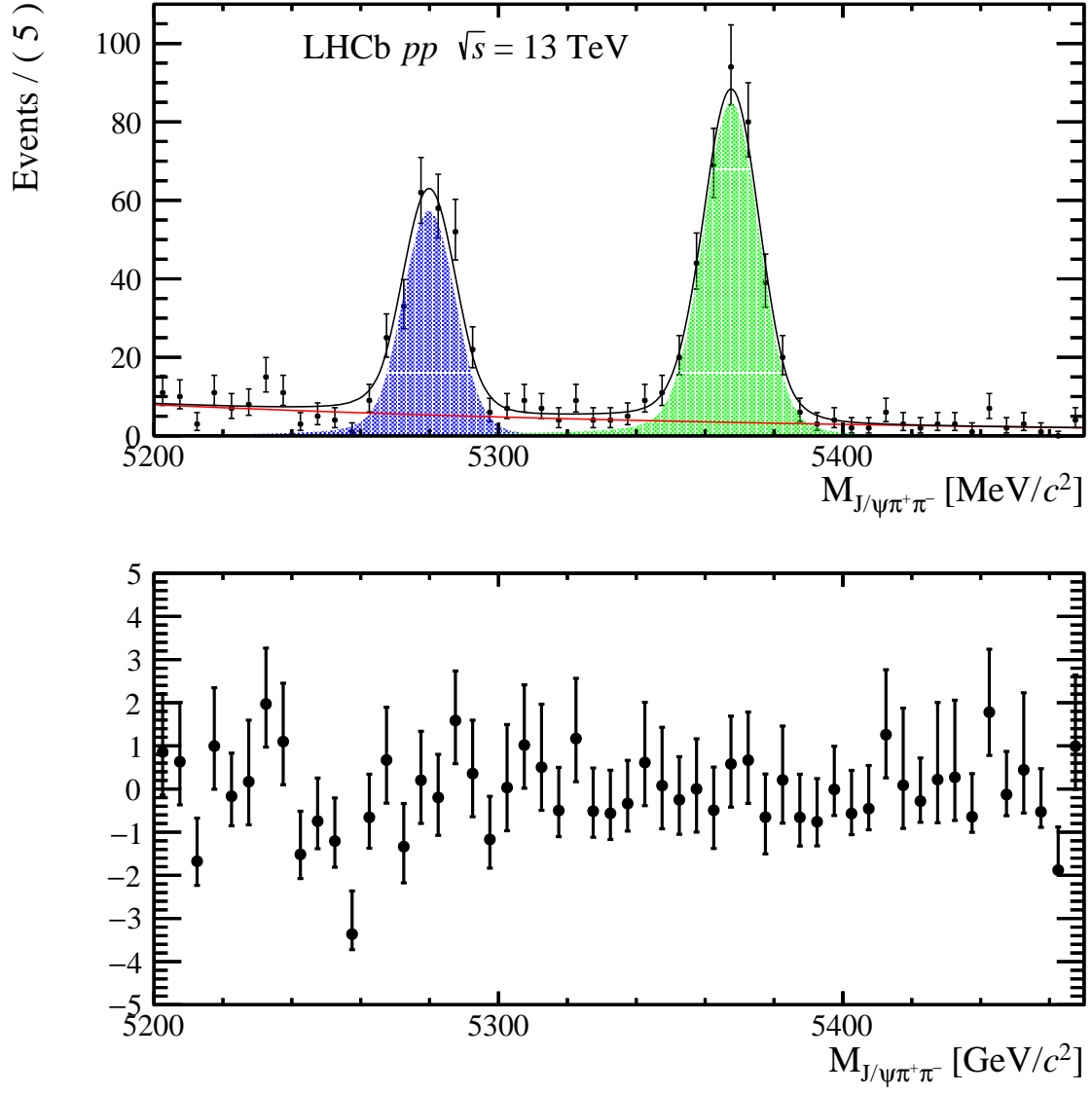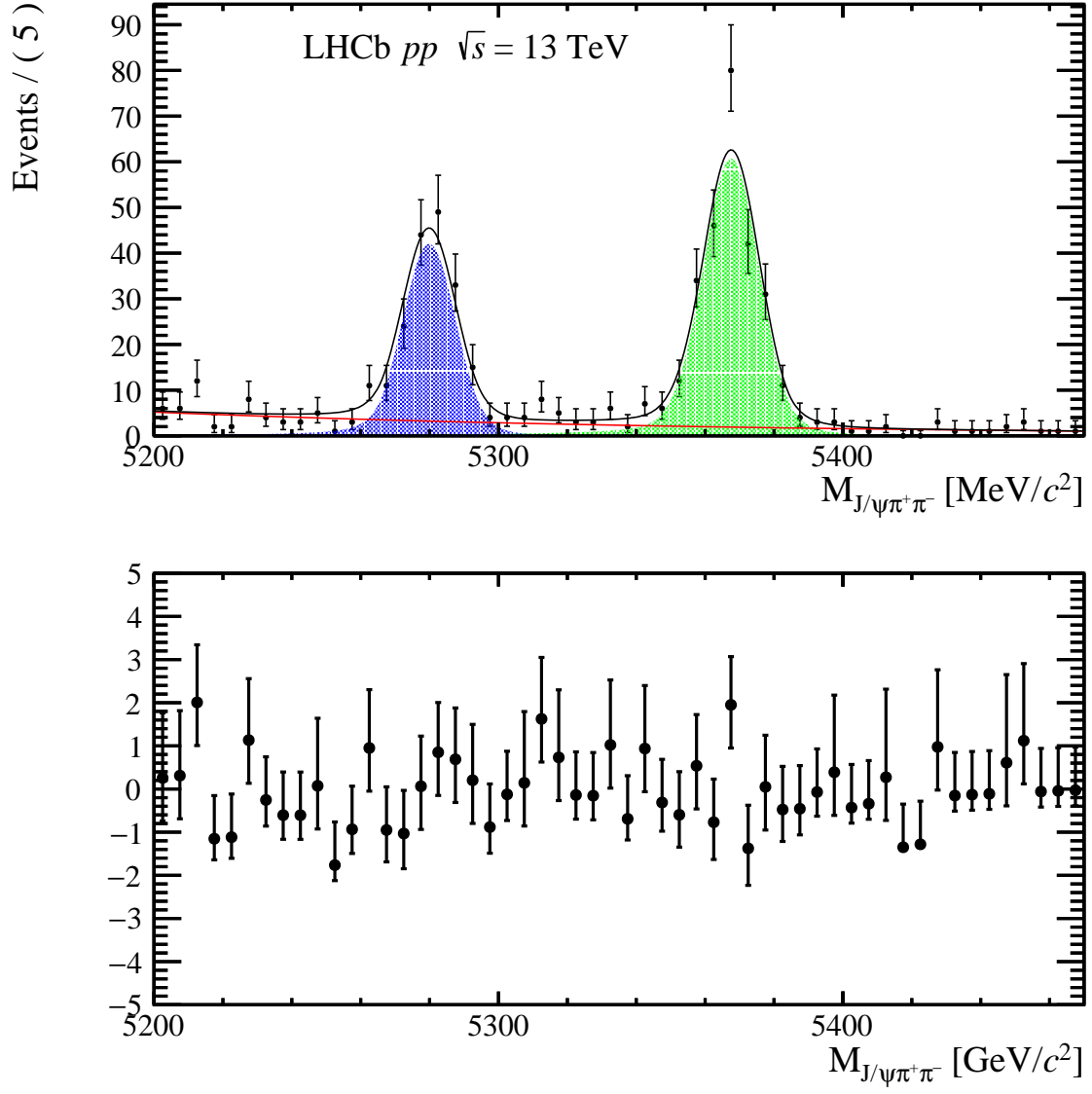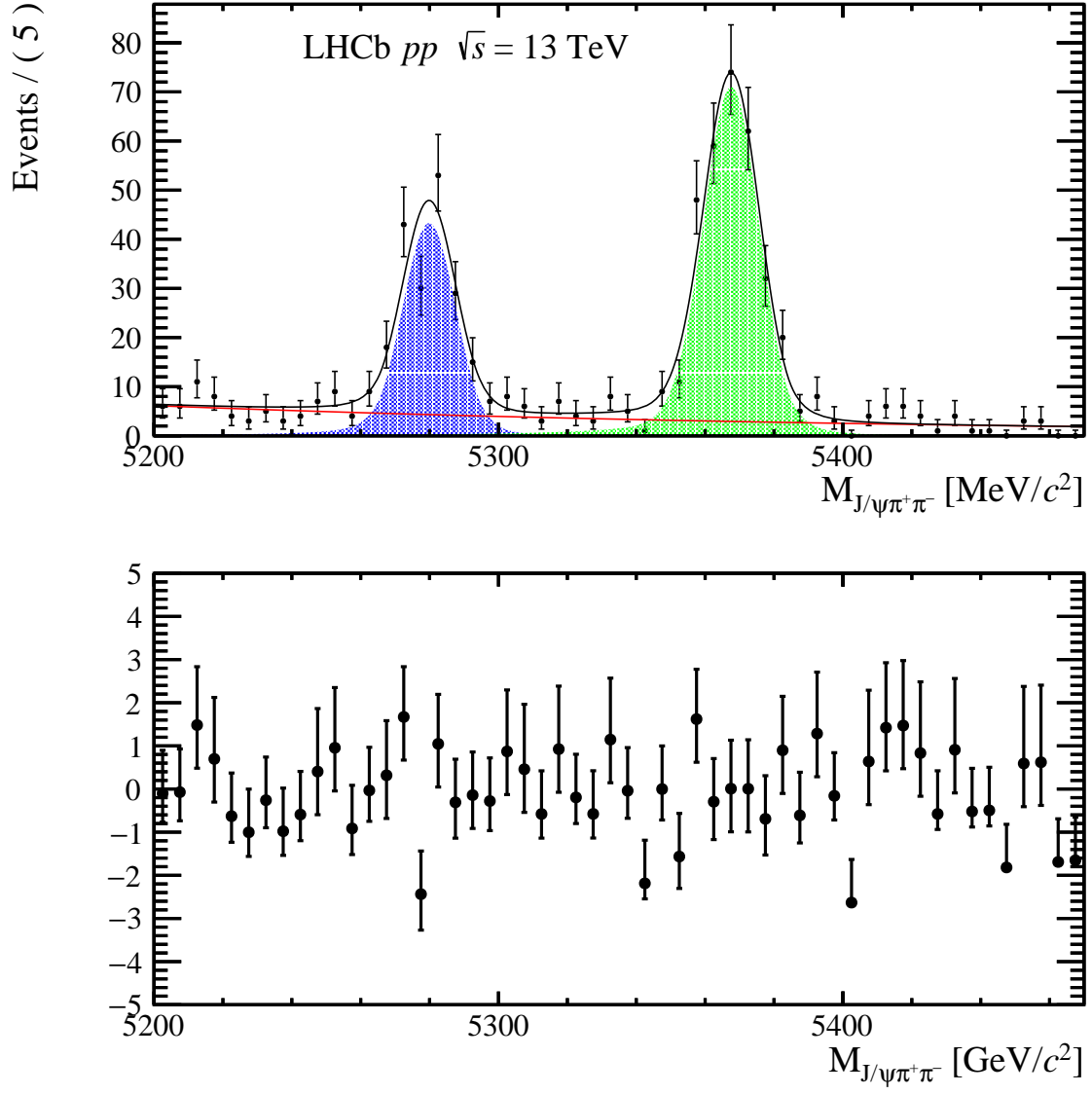
Figure 87: Fit to the $J/\psi\pi^+\pi^-$ mass spectrum in the multiplicity range $16 \leq N_{tracks}^{back} \leq 20$.

Figure 88: Fit to the $J/\psi\pi^+\pi^-$ mass spectrum in the multiplicity range $21 \leq N^{back}_{tracks} \leq 25$.

Figure 89: Fit to the $J/\psi\pi^+\pi^-$ mass spectrum in the multiplicity range $26 \leq N_{tracks}^{back} \leq 30$.

Figure 90: Fit to the $J/\psi\pi^+\pi^-$ mass spectrum in the multiplicity range $31 \leq N_{tracks}^{back} \leq 40$.
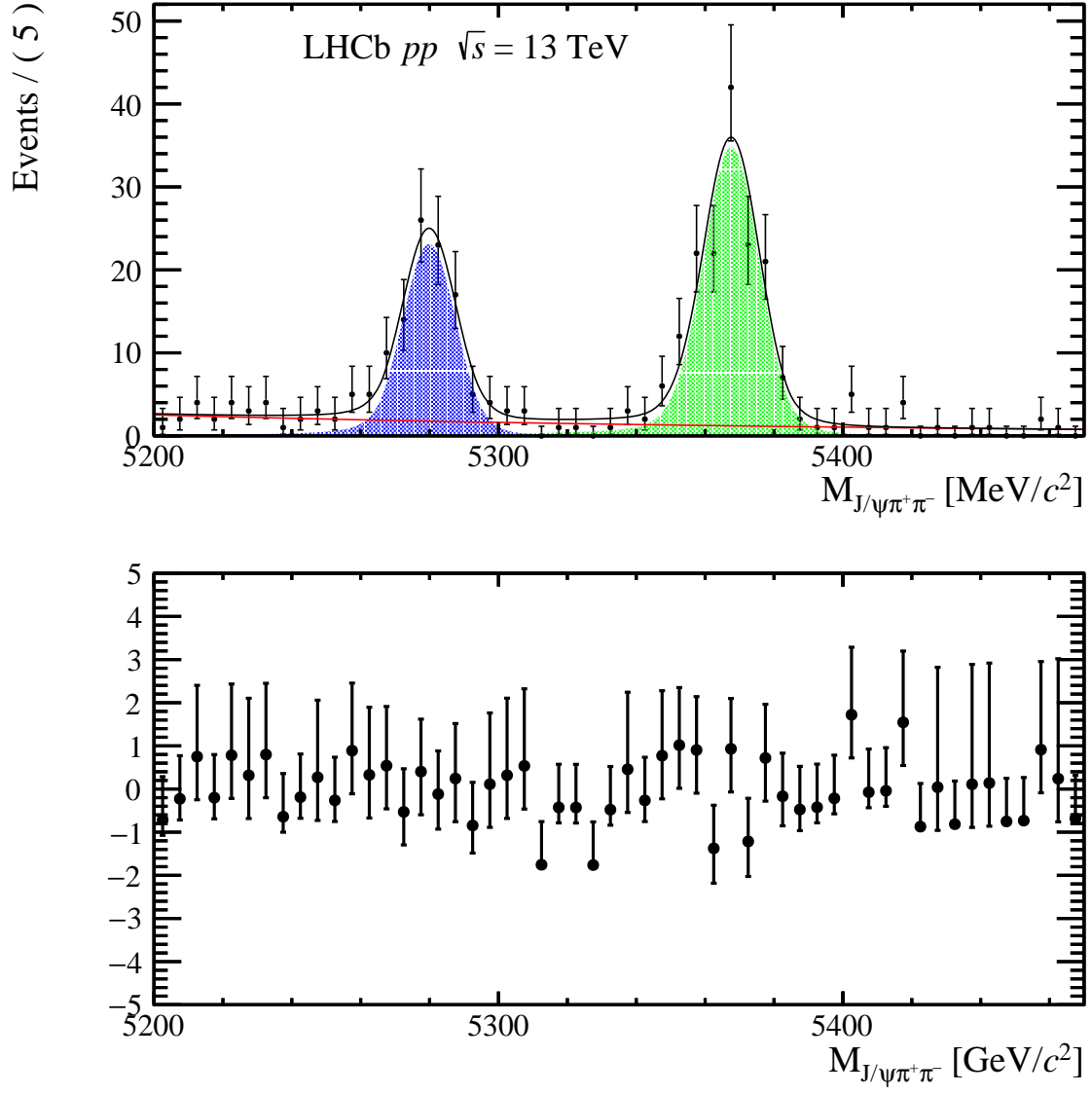
Figure 91: Fit to the $J/\psi\pi^+\pi^-$ mass spectrum in the multiplicity range $41 \leq N^{back}_{tracks} \leq 60$.